SIMULATION OF ELECTROMAGNETIC WAVES PROPAGATING IN COMPLEX MEDIA WITH THE TLM METHOD

CÉDRIC BLANCHARD

July 7, 2009

Universidad de Granada.

Departamento de Física Aplicada.

Tesis doctoral:

SIMULATION OF ELECTROMAGNETIC WAVES PROPAGATING IN COMPLEX MEDIA WITH THE TLM METHOD.

Autor:
Cédric Blanchard.

Directores:
Jorge Andrés Portí Durán, Juan Antonio Morente Chiquero y Alfonso Salinas Extremera.

Granada, 7 de Julio de 2009.

Editor: Editorial de la Universidad de Granada
Autor: Cédric Blanchard
D.L.: GR. 2648-2009
ISBN: 978-84-692-4176-9

Contents

Chapter 1

Overview

Since James Clerk Maxwell's fundamental achievement, *A Treatise on Electricity and Magnetism* in 1873, electromagnetic wave theory has allowed plenty of developments. However, complex internal constitution or boundary conditions of media can render several electromagnetic problems arduous, or even impossible, to be analytically derivable. This difficulty is usually overcome by employing computational numerical methods. The concern of this thesis is the modeling of complex media with the Transmission Line Modeling (TLM) method [1].

An important part of numerical methods starts with the derivation of an integral equation which is later numerically solved by means of different well-known methods, such as the Finite Element Method [2] or the Method of Moments [3]. In a certain way, the above mentioned approaches may be considered as semi-analytical or of integral nature in the sense that an important theoretical task is developed first to obtain the integral equation, prior to the specific numerical treatment is applied. These semi-analytical methods provide good results, but the theoretical part requires an important reformulation if different problems or new effects are to be considered. Let us think, for example, of a problem devised for a static or quasi-static situation, the integral equation describing the phenomenon has nothing to do with the same problem for a high-frequency case.

A different approach is provided by differential equation solvers working in the time domain, such as the Finite Differences in the Time Domain (FDTD) method [4, 5] or TLM. In their basic version, these techniques directly consider Maxwell's equations together with boundary conditions to numerically model a certain phenomenon. Of course, considering the problem through basic equations in their most fundamental form, i.e., Maxwell and constitutive equations, may

be considered of limited elegance because most of the work is performed by the computer, requiring an almost negligible amount of theoretical work. The main drawback of differential methods is that the computing burden is relatively high when compared to the requirements of semi-analytical methods. Nevertheless the strength of time domain methods are multiple:

- They are easily adaptable to new situations by only adding minor changes to the code.
- Solutions can cover a wide frequency range with a single simulation run by using a simple Fourier transform.
- Since the electromagnetic field is calculated everywhere in the computational domain, animated displays of its movements through the time process is available. This dynamical picture may be useful in understanding what is going on in the model, or simply to help confirm that the simulation is correctly working.

This feature makes these intuitive methods attractive tools for the modeling of diverse electromagnetic problems.

In this dissertation, TLM will be discussed, developed, and used for problem involving complex media. TLM is, as FDTD, a low-frequency numerical method well-suited for the modeling of wave propagation problems. Even if it has been mainly applied to solve questions of electromagnetic concern, it has been used in the realm of acoustic [6], particle diffusion [7], or propagation of electromagnetic waves in celestial body's atmosphere [8]. Due to many similarities between TLM and FDTD, both methods were often compared to each other [9–12]; these analysis showed that the performance of TLM and FDTD are actually comparable. Nevertheless, some advantages of the former over the latter method should be emphasized:

- TLM defines all the field quantities at the same point, precisely at the center of the basic building blocks (transmission line segments forming a node), and at the same time. In FDTD, such a versatility is not allowed given that the electromagnetic field components are spatially separated. Furthermore, the electric and magnetic fields are not solved at the same time, meaning that the FDTD routine is a two-step technique.

- The most significant disparity is the way both methods address the physical system to be simulate. FDTD discretizes Maxwell's equations, and is, therefore, basically an approximate technique to solve differential equations that represent the system under consideration. On the contrary, TLM is directly a numerical model of the physical system through equivalent transmission line circuits. In this manner, the approximations made when using TLM lie in the model rather than in the discretization of equations.

The main weakness of TLM compared to FDTD lies in the fact that it has not been extensively used like the latter method. Accordingly, there are relatively few tools and prior development to assist a physicist that wishes to perform numerical modeling with TLM. Thus, using TLM requires a good understanding of the method because such a physicist will certainly have to develop his own implementations in the aim of solving challenging issues.

The results presented in this thesis are mainly based on published articles contributed by the author in journals and conferences [13–26]. The first simulated media, in chapter 3, will be dielectric composite materials, the objective being the determination of the effective permittivity of the mixture. Second, the interaction between invisibility cloaks and electromagnetic waves will be investigated in chapter 4. Prior to these contributions, chapter 2 will be devoted to a large review on TLM, useful developments to the study of dispersive metamaterials will be reported, as well.

Chapter 2

The Transmission Line Modeling method (TLM)

2.1 Introduction

Employing electrical networks to solve problems that involve the propagation of electromagnetic fields is a well-established technique since the 1940s when Kron [27] and Whinnery [28] presented their precursor works. Inspired by these contributions, Johns and Beurle created the transmission line modeling (TLM) method in 1971 [1]. TLM is a numerical time-domain method that can be viewed as the circuit equivalent of Huygens' principle for light propagation. This principle states that each point on a primary wavefront can be considered to be a new source of a secondary spherical wave and that a secondary wavefront can be constructed as the envelope of these secondary spherical waves. In the same manner, the discretization of space leads to the TLM mesh in which each propagating voltage pulse is a new source of radiation. One of the most significant properties of TLM is that the mesh is a network of intersecting transmission lines, meaning that it should be regarded as a modeling procedure rather than a direct numerical solution of the electromagnetic field equations. Indeed, no differential or integral equations are solved, TLM is directly a numerical model of a physical system.

- In section 2.2 of this chapter, we will introduce TLM from an historical point of view. The two-dimensional (2D) parallel node, which was proposed in Johns and Beurle's pioneering article [1], and the three-dimensional (3D) Symmetrical Condensed Node [29] are briefly presented. The aim of this section is not to give too many details; instead, some basic and useful con-

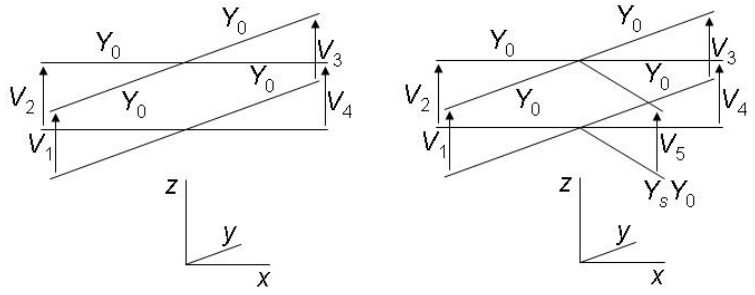

Figure 2.1: 2D parallel node: (a) without stub, (b) with stub.

cepts will be introduced. Furthermore, the limitations of the historical approach will be emphasized.

- In section 2.3, a more modern description will be presented with extensive details.
- In section 2.4, it will be shown that the usual Cartesian nodes can be substituted by curved nodes that allow the modeling of curved geometries very conveniently.
- In section 2.5, TLM will be extended to simulated metamaterials whose permittivity and/or permeability are less than the usual unitary values of free space.
- In section 2.6, we will focus on the frequency response of the modified TLM mesh for the modeling of metamaterials.

2.2 Historic representation of the TLM nodes

In their pioneering work, Johns and Beurle presented the TLM elementary cell, called node, as a junction between a pair of transmission lines [1] with characteristic impedance Z_0 or, equivalently, with admittance $Y_0 = 1/Z_0$. As a result, the first calculations were carried out in the structure depicted in Fig. 2.1(a), the complete network being made up of a large number of such building blocks. The node shown in Fig. 2.1(a) is a shunt circuit, that is why it was referred to it as parallel node. At low frequencies, Johns showed that the node can be represented

by a network made of lumped inductors, with inductance L, and capacitors, with capacitance C. It turns out that the equations applying in such a network are analogous to those of Maxwell for an electromagnetic wave propagating with the electric field normal to the plane of propagation, i.e., the transverse-electric (TE) mode. Note that it is wise to be aware that in other realms of physics or other authors use different conventions for the meaning of TE or transverse-magnetic (TM) modes. Our convention is common, but it should be kept in mind that the TE mode may represent a mode in which the electric field is confined to the plane of propagation. The analogy between Maxwell's equations and the equations of transmission lines theory constitutes the base of TLM, the calculation of the electric and magnetic field being substituted by the calculation of tension and intensity pulses that propagate in the mesh. The incident pulses penetrate into the node in Fig. 2.1(a) from the four ports; the information is grouped in the voltage vector,

$$\overline{V}^i = \begin{pmatrix} V_1 \\ V_2 \\ V_3 \\ V_4 \end{pmatrix}^i . \tag{2.1}$$

When reaching the center of the node, the incoming pulses are scattered along the four available directions, which gives rise to a set of reflected pulses we will refer to as

$$\overline{V}^r = \begin{pmatrix} V_1 \\ V_2 \\ V_3 \\ V_4 \end{pmatrix}^r . \tag{2.2}$$

This redistribution of the incident pulses is determined by a scattering matrix, S, such that,

$$\overline{V}^r = S\overline{V}^i . \tag{2.3}$$

The determination of S is an important step of the method. Given a unitary pulse incident from one port, it reaches the parallel connection of three lines, or equivalently, sees an effective admittance $3Y_0$. Therefore, the reflection, Γ, and trans-

mission, τ, coefficients are,

$$\Gamma = \frac{Y_0 - 3Y_0}{Y_0 + 3Y_0} = -\frac{1}{2}, \tag{2.4a}$$

$$\tau = \frac{2Y_0}{Y_0 + 3Y_0} = \frac{1}{2}, \tag{2.4b}$$

The voltage reflected at the incident port equals Γ, while the pulses transmitted to the rest of lines equals τ. Doing so for unitary pulses incident for all the lines in the node, it results that

$$S = \frac{1}{2}\begin{pmatrix} -1 & 1 & 1 & 1 \\ 1 & -1 & 1 & 1 \\ 1 & 1 & -1 & 1 \\ 1 & 1 & 1 & -1 \end{pmatrix}. \tag{2.5}$$

Due to the simple topology of the parallel node, the determination of S is straightforward. Nonetheless, the derivation of the scattering matrix for a more complicated node can be very difficult. In section 2.3.1, a technique that considerably simplifies the obtention of S will be presented [30].

The circuit parameters (L and C) are adjusted to account for the local value of permittivity and permeability; in this manner, the simple node in Fig. 2.1(a) is only capable of simulating homogeneous media because the capacitance and inductance of the constitutive transmission lines remain constant throughout the mesh. However, extra capacitance can be introduced to the node by equipping the node with a supplementary transmission line, i.e., a stub such that the permittivity can be variable. Note that the stub is only connected to the center of the node, no line of adjacent nodes is connected to it. This relates with the fact that this stub does not model propagation, but it serves as a means of controlling the speed of propagation. The stubbed parallel node is depicted in Fig. 2.1(b), where it can be seen that a fifth line has been added. However, this treatment does not allow variation on the permeability, which constitutes a significant limitation. An important point that should be emphasized is that the node is usually represented by a single equivalent electrical circuit in order to calculate the electromagnetic field in terms of the voltage and intensity pulses [31].

A fundamental contribution to TLM was the development of the Symmetrical Condensed Node (SCN), also proposed by Johns [29], to solve 3D problems.

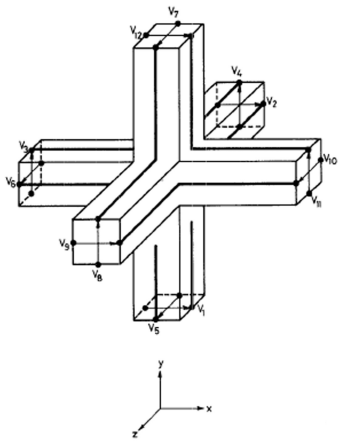

Figure 2.2: The symmetrical condensed node.

The node without stubs, as it appeared in Johns' original paper, is depicted in Fig. 2.2. Johns claimed that SCN can no longer be represented by an equivalent electrical circuit [29] because the transmission lines may couple with each other, in agreement with the fact that the components of the electromagnetic field couple in Maxwell's equations. Johns' statement was certainly true: no single equivalent circuit can be drawn up to represent SCN. However, it was shown by Naylor [30, 32] that SCN can be represented by a set of equivalent shunt-only and series-only circuits, where the particular pair of transmission lines under consideration are common to both circuits. This vision has long been unique to the description of 3D nodes. Nonetheless, we have recently pointed out [14] that even 2D nodes must be represented by a set of coupled shunt- and series-circuits. Actually, as pointed out in the preceding paragraph, the representation of the parallel node by a single circuit limits its validity to media for which only capacitive terms (as the permittivity) are variable. In contrast, describing the parallel node as a set of coupled parallel and series nodes provides more versatility to the node; allowing inductive magnitudes, such as the permeability, to be simulated. Section 2.3.1 will be devoted to what should be named a global node for TE modes, instead of parallel node, since it no longer makes sense to refer to it as parallel. Furthermore, the global node for TM modes will be presented in section 2.3.2; such a node is the generalization of the historical series node [33] that may be considered as the counterpart of the parallel node.

For further reading, more details can be found in [1, 31]. However, it is useful to derive important relations for the next sections. Let us consider the structure displayed in Fig. 2.2, where the node represents a cube of space of dimension Δx, Δy, Δz, and the total capacitance and inductance associated with a certain constitutive transmission line are C_i, L_i, respectively. To model a medium with permittivity $\varepsilon_i\varepsilon_0$ and permeability $\mu_i\mu_0$, the capacitance and inductance are required to be:

$$C_i = \varepsilon_i\varepsilon_0\frac{\Delta j\Delta k}{\Delta i}, \tag{2.6a}$$

$$L_i = \mu_i\mu_0\frac{\Delta j\Delta k}{\Delta i}, \tag{2.6b}$$

respectively, where $(i, j, k) = \{x, y, z\}$. Details on Eqs. 2.6a and 2.6b are given in section 2.3.3; concretely, the result is proven in Eqs. 2.72 and 2.75.

Let Y_i be the characteristic admittance of a particular constitutive transmission line. If we assume that $\Delta x = \Delta y = \Delta z = \Delta l$, the length of the individual line is $\Delta l/2$. Moreover, Δt is the complete time step of the calculation, i.e., the time required for a pulse to traverse the transmission lines that link the adjacent nodes of a certain node. Thus, the propagation time on each line is $\Delta t/2$. Hence, the distributed capacitance and inductance are given by

$$C_i^d = \frac{C_i}{\frac{\Delta l}{2}}, \tag{2.7a}$$

$$L_i^d = \frac{L_i}{\frac{\Delta l}{2}}; \tag{2.7b}$$

while the velocity of propagation on each transmission line is

$$\begin{aligned} v_{TL} &= \frac{\Delta l/2}{\Delta t/2} = \frac{\Delta l}{\Delta t} = \frac{1}{\sqrt{C_i^d L_i^d}} = \frac{\Delta l}{2\sqrt{C_i L_i}} \\ &\Rightarrow \Delta t = 2\sqrt{C_i L_i}. \end{aligned} \tag{2.8}$$

Thus, the total admittance and impedance of line i in terms of C_i and L_i is naturally

derived from Eq. 2.8:

$$Y_i Y_0 = \sqrt{\frac{C_i}{L_i}} = \frac{2C_i}{\Delta t}, \tag{2.9a}$$

$$Z_i Z_0 = \sqrt{\frac{L_i}{C_i}} = \frac{2L_i}{\Delta t}. \tag{2.9b}$$

Hence,

$$C_i = Y_i Y_0 \frac{\Delta t}{2}, \tag{2.10a}$$

$$L_i = Z_i Z_0 \frac{\Delta t}{2}. \tag{2.10b}$$

In practice, a purely capacitive line, as the stub of the node in Fig. 2.1(b), adds a capacitance given by Eq. 2.10a to the node. Similarly, Eq. 2.10b may describe the inductance generated by the inductive stub of a series node.

Finally, it has been mentioned at the beginning of this section that a transmission line can be represented by an equivalent distributed network at low frequency. TLM is thus a low frequency method that have an upper limit for the frequency response, this limit depends on the coarseness of the mesh. Usually, we ensure that the smallest wavelength involved in the problem under consideration is greater than ten times $\max(\Delta x, \Delta y, \Delta x)$:

$$\lambda \geq 10 \max(\Delta x, \Delta y, \Delta x). \tag{2.11}$$

The practical rule given by Eq. 2.11 is actually based on rigorous analysis of the relation of dispersion associated with TLM [34].

2.3 TLM Cartesian nodes

2.3.1 Nodes for transverse electric modes

When P. B. Johns introduced the SCN in 1987, he emphasized that a break must be made with the traditional representation of nodes by an equivalent electrical circuit obtained by replacing the transmission lines and incident pulses by Thevenin equivalent circuits [29]. Indeed, SCN can no longer be represented by a single lumped circuit.

On the contrary, the usual 2D shunt and series nodes presented in section 2.2

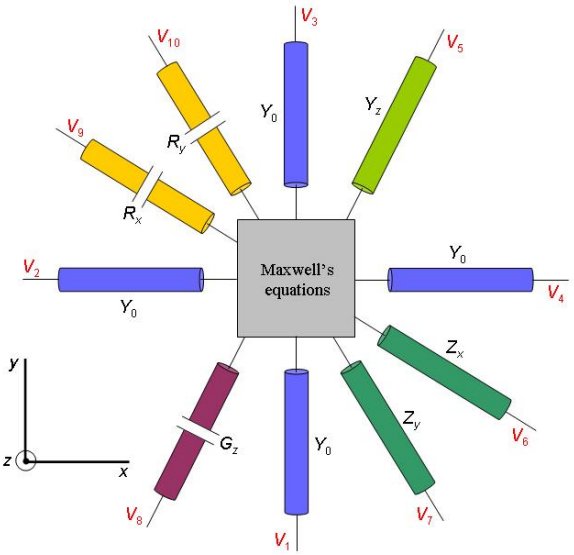

Figure 2.3: 2D global node for TE modes. Note that the propagation of the pulses is effectuated through the link lines (blue color), the other lines allow a control on the constitutive parameters of the medium under consideration.

are represented by an equivalent circuit. However, it has been shown that this circuit representation leads to limitations, particularly if one wants to consider more general cases, such as magnetic or electric losses. We published a paper in which it is pointed out that a 2D node cannot be directly represented as a single circuit neither [14]. It is more appropriate to consider the node as the multi-port system or formal circuit shown (for the case of a TE mode) in Fig. 2.3, in which the black box at the node center represents the formal connection of the lines that describe Maxwell's equations. The global node describes all the non-trivial component of Maxwell's equations, i.e., it can be split into three sub-circuits, each one of them describing a component of the electromagnetic field and being equivalent to a component of Maxwell's equations. Let us consider an electromagnetic wave that propagates with TE polarization; when the shunt node was required in the historical description, we have instead three coupled circuits: a shunt sub-circuit for E_z, and two series sub-circuits for H_x and H_y, as depicted in Fig. 2.4.

The E_z sub-circuit shown in Fig. 2.4(a) is made up of four connecting or link lines (lines 1-4) of admittance Y_0. It is worth noting that Y_0 is not necessarily the admittance of free space which we will refer to as $\frac{1}{\eta_0} = \sqrt{\varepsilon_0/\mu_0}$, where η_0 is

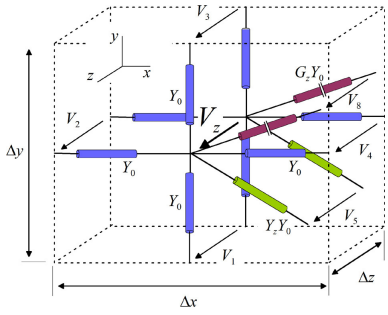

(a) Parallel sub-circuit for the z-component of Ampère's law to define E_z.

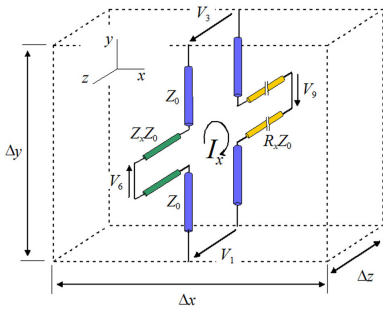

(b) Series sub-circuit for the x-component of Faraday's law to define H_x.

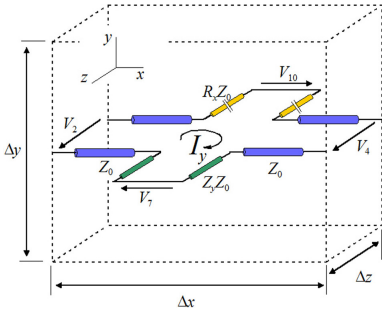

(c) Series sub-circuit for the y-component of Faraday's law to define H_y.

Figure 2.4: Splitting of the 2D global node into into three sub-circuits.

the impedance of free space. Instead, the value of Y_0 can be judiciously chosen depending on the problem under consideration, however we will show later that some restrictions may apply. The sub-circuit is also equipped by a capacitive stub (line 5), with admittance $Y_z Y_0$, which allows independent control of ε_z. A lossy stub (line 8), which may be regarded as infinitely long or, equivalently, as terminated by its own characteristic impedance, is also connected to the node in order to incorporate electric conductivity σ_z^e. Any pulse scattered into the lossy stub is then absorbed, with no possibility of being readmitted into the circuit. The admittance of line 8 is given by $G_z Y_0$, and the expression of G_z in terms of σ_z^e will be given and proven in section 2.3.3 at Eq. 2.73c.

The H_x and H_y sub-circuits, shown in Figs. 2.4(b) and 2.4(c), are each made up of two connecting lines (lines 1 and 3, and lines 2 and 4; respectively) whose impedance is $Z_0 = 1/Y_0$. Furthermore, they are each equipped with an inductive stub (line 6 and line 7, respectively), with impedances $Z_x Z_0$ and $Z_y Z_0$, which allows independent control of μ_x and μ_y. Since E is not involved here, there is no lossy stub for electric conductivity. Nonetheless, we can introduce an even more versatile node by adding magnetic losses along the x- and y-directions; that results in another infinite stub in both sub-circuits (line 9 and line 10, respectively) to take into account the magnetic resistivities σ_x^m and σ_x^m. Impedances of lines 9 and 10 are given by $R_x Z_0$ and $R_y Z_0$, respectively. Even if such a general situation is unlikely, we do consider magnetic resistivity for the sake of generality, and also because new materials do have magnetic losses. However, note that such a general node leads to high computational requirements and should be sparingly used. Furthermore, the expression of R_x and R_y in terms of σ_x^m and σ_y^m will be given and proven in section 2.3.3 at Eqs. 2.76a and 2.76b, respectively.

The total capacitance associated with lines 1-5 in Fig. 2.4(a) is given by $C_z = 4Y_0 \frac{\Delta t}{2} + Y_z Y_0 \frac{\Delta t}{2}$; the total inductance associated with lines 1, 3, and 6 in Fig. 2.4(b) turns out to be $L_x = 2Z_0 \frac{\Delta t}{2} + Z_x Z_0 \frac{\Delta t}{2}$; while we calculate that the total inductance associated with lines 2, 4, and 7 in Fig. 2.4(c) is $L_y = 2Z_0 \frac{\Delta t}{2} + Z_y Z_0 \frac{\Delta t}{2}$. Given that the circuits in Fig. 2.4 must model a medium with $C_z = \varepsilon_z \frac{\Delta x \Delta y}{\Delta z}$, $L_x = \mu_x \frac{\Delta y \Delta z}{\Delta x}$, and $L_y = \mu_y \frac{\Delta x \Delta z}{\Delta y}$, simple operations provide the following expressions for Z_x, Z_y, and

Y_z:

$$Z_x = \frac{2\mu_x\mu_0}{Z_0\Delta t}\frac{\Delta y\Delta z}{\Delta x} - 2, \tag{2.12a}$$

$$Z_y = \frac{2\mu_y\mu_0}{Z_0\Delta t}\frac{\Delta x\Delta z}{\Delta y} - 2, \tag{2.12b}$$

$$Y_z = \frac{2\varepsilon_z\varepsilon_0}{Y_0\Delta t}\frac{\Delta x\Delta y}{\Delta z} - 4. \tag{2.12c}$$

Since the above parameters represent the admittances and impedances of a transmission line, they must be positive. That has direct consequences on the TLM time-step, Δt, and on Z_0; both must be chosen so that Z_x, Z_y, and Y_z are nonnegative. Let ε_z^-, μ_x^-, and μ_y^-, be the lowest constitutive parameters of the modeled space. Note that as long as only usual materials are involved, these three parameters are greater than unity. We get:

$$\Delta t \leq \Delta t_x = \frac{\mu_x^-\mu_0}{Z_0}\frac{\Delta y\Delta z}{\Delta x}, \tag{2.13a}$$

$$\Delta t \leq \Delta t_y = \frac{\mu_y^-\mu_0}{Z_0}\frac{\Delta x\Delta z}{\Delta y}, \tag{2.13b}$$

$$\Delta t \leq \Delta t_z = \frac{\varepsilon_z^-\varepsilon_0}{2Y_0}\frac{\Delta x\Delta y}{\Delta z}. \tag{2.13c}$$

In order to eliminate one of the two inductive stubs,

$$\Delta t = \min(\Delta t_x, \Delta t_y). \tag{2.14}$$

Furthermore, the capacitive stub is canceled, i.e., $Y_z = 0$ if the value

$$Y_0 = \frac{1}{2}\frac{\varepsilon_z^-\varepsilon_0}{\Delta t}\frac{\Delta x\Delta y}{\Delta z} \tag{2.15}$$

is selected. If we take into account the choice of Δt, it turns out that

$$Z_0 = \sqrt{2}\eta^-\eta_0\frac{\Delta z}{\Delta \iota}, \tag{2.16}$$

where ι is either x or y depending on the Δt that has been elected, and where $\eta^- = \sqrt{\frac{\mu_\iota^-}{\varepsilon_z^-}}$. It is possible that η^- be the impedance of no constitutive material of the simulated space; indeed the space with the smallest permittivity and the space

with the smallest permeability may no coincide. However, if such a space exists, it should be noted that this space in particular is entirely described by using only a single inductive stub if the above Δt and Z_0 are chosen. A situation very often met is $\Delta x = \Delta y = \Delta z = \Delta l$, $\varepsilon_z^- = 1$, $\mu_x^- = 1$, and $\mu_y^- = 1$; in this case,

$$Z_0 = \sqrt{2}\eta_0. \tag{2.17}$$

With this approach, it is possible to simulate a certain class of metamaterials whose optics constants ranges from zero to one. All we have to do is to decrease the TLM time step, Δt. However, this prescription no longer holds if ε and/or μ are negative; moreover, decreasing Δt increases the computational requirements. We will present in section 2.5 a better way to model metamaterials: negative values will be allowed and Δt will not have to be decreased.

Obtaining the scattering matrix S that connects the incident and reflected pulses at the node center according to $V^r = SV^i$, is not a straightforward task. We use the method of common and uncommon lines presented by Portí *et al.* [30] that simplifies the derivation of S. First, it is worth noting that the node is made up of a total of 10 lines that should lead to a 10×10 matrix. But, since no incident voltages are coming from the lossy stubs, S can be reduced to a 7 columns, 10 rows matrix. Moreover, the pulses that are reflected from the node center to the lossy stubs are usually not of valuable interest, except for energy conservation reasons, S is consequently a 7×7 matrix.

Let us suppose that a voltage pulse V_1^i of unit amplitude is incident upon port 1 of the structure in Fig. 2.4. This pulse only excites H_x and E_z and propagates along the y-direction. In terms of Maxwell's equations, only the x-component of Faraday's law (associated with Fig. 2.4(b)) and the z-component of Ampère's law (associated with Fig. 2.4(a)) are involved. Thus, logically, port 1 is only present in the two above-mentioned sub-circuits.

1. **Uncommon lines: Shunt sub-circuit in Fig. 2.4(a).**
   The pulse is scattered into ports 1, 2, 3, 4, 5, and 8. Obviously, ports 1 and 3 are common with the other sub-node, determining V_1^r and V_3^r is then not trivial given that circuit is not the only information to be considered. On the other hand, ports 2, 4, 5, and 8 are uncommon: they are completely defined by the circuit and, therefore, V_2^r, V_4^r, V_5^r, and V_8^r are equal to the transmission

coefficient given here by

$$\tau = \frac{2Y_1}{Y_1 + Y_L}, \tag{2.18}$$

where

$$\begin{aligned} Y_L &= Y_2 + Y_3 + Y_4 + Y_5 + Y_8 \\ &= 3Y_0 + Y_z Y_0 + G_z Y_0 \end{aligned} \tag{2.19}$$

is the load admittance. Let the amplitude scattered into ports 2, 4, 5, and 8 be $c = V_2^r = V_4^r = V_5^r = V_8^r = \tau$, we get:

$$c = \frac{2}{4 + Y_z + G_z}. \tag{2.20}$$

Although there is no need to evaluate V_8^r as an element of S, its value will be of interest for defining the common voltages as we will see hereinafter.

2. **Uncommon lines: Series sub-circuit in Fig. 2.4(b).**
Here, the pulse is scattered into ports 1, 3, 6, and 9. Only ports 6 and 9 are uncommon to the shunt subcircuit; we obtain V_6^r and V_9^r by using the transmission coefficient that applies to this series node:

$$\tau = \frac{2Z_L}{Z_1 + Z_L}, \tag{2.21}$$

where

$$\begin{aligned} Z_L &= Z_3 + Z_6 + Z_9 \\ &= Z_0 + Z_x Z_0 + R_x Z_0. \end{aligned} \tag{2.22}$$

At this stage, a voltage divider has to been employed in this series circuit to define the part of the transmitted voltage in each line. This results in:

$$V_6^r = -\tau \frac{Z_x Z_0}{Z_L}, \tag{2.23a}$$

$$V_9^r = -\tau \frac{R_x Z_0}{Z_L}. \tag{2.23b}$$

If the amplitude scattered into the inductive stub (port 6) is $-e_x$, we finally calculate that:

$$e_x = \frac{2Z_x}{2 + Z_x + R_x}. \tag{2.24}$$

Again, it is not necessary to name the amplitude scattered into the lossy stub

(port 9), i.e.,

$$V_9^r = -\frac{2R_x}{2+Z_x+R_x}. \tag{2.25}$$

because it will not appear in S, but it will be useful for defining voltages at the common lines.

3. **Common lines to both sub-circuits.**
The situation is quite different for pulses reflected at ports 1 and 3, common to the series and parallel sub-circuits. Both must be simultaneously considered in order to represent the coupling between Maxwell's equations. The difficulty is that the circuits do not describe this coupling; consequently, a more traditional derivation, involving the flux of Ampère's law and the circulation of Faraday's law, has to be carried out. However, it is shown in [14] that these two conditions are equivalent to circuit conditions that ensure continuity of potential at the series sub-circuit and charge conservation at the shunt sub-circuit. Let the amplitudes of the pulses scattered into ports 1 and 3 be a_x and b_x, respectively. On the one hand, the continuity of the electric potential for the series node yields

$$\begin{aligned} &V_1 - V_3 + V_6 + V_9 = 0 \\ &\Rightarrow (1+a_x) - b_x - e_x + V_9 = 0. \end{aligned} \tag{2.26}$$

On the other hand, the conservation of charge for the parallel node yields

$$\begin{aligned} &I_1^i = I_1^r + I_2^r + I_3^r + I_4^r + I_5^r + I_8^r \\ &\Rightarrow Y_0 = a_x Y_0 + cY_0 + b_x Y_0 + cY_0 + cY_z Y_0 + cG_z Y_0. \end{aligned} \tag{2.27}$$

Calculations that involve Eqs. 2.20, 2.24, 2.25, 2.26, and 2.27, give

$$a_x = \frac{2}{4+Y_z+G_z} - \frac{2}{2+Z_x+R_x}, \tag{2.28}$$

$$b_x = \frac{2}{4+Y_z+G_z} - \frac{Z_x+R_x}{2+Z_x+R_x}. \tag{2.29}$$

It is worth putting the emphasis on that, in a general situation, coefficients a and b, which correspond to common lines, cannot be calculated by simply using the reflection or transmission coefficients of sub-circuits in Fig. 2.4(a) or 2.4(b). This enforces the idea that a single circuit is not valid for representing not only three but also 2D TLM nodes [14].

We have examined the scattering that occurs into the node if a pulse enters port 1. The analysis for a pulse that excites any other connecting line (2, 3, or 4) would be the same.

However, there are still remaining concerns: what happens if a unitary pulse is coming from the stubs?

1. Suppose that a voltage pulse V_5^i of unit amplitude is incident upon port 5 of the structure in Fig. 2.4. In this case, only one circuit is to be considered and, therefore, $V_1^r, V_2^r, V_3^r, V_4^r$ are obtained from the transmission coefficient,

$$\tau = \frac{2Y_5}{Y_5 + Y_L}, \tag{2.30}$$

while $V_5^r = \Gamma$, the reflection coefficient, given by

$$\Gamma = \frac{Y_5 - Y_L}{Y_5 + Y_L}, \tag{2.31}$$

where, in both expressions,

$$\begin{aligned} Y_L &= Y_1 + Y_2 + Y_3 + Y_4 + Y_8 \\ &= 4Y_0 + G_z Y_0. \end{aligned} \tag{2.32}$$

Let the amplitude of the pulses scattered into port 5 be f, and the amplitude of the pulses scattered into ports 1, 2, 3, and 4 be g. Then it may be shown:

$$f = \frac{Y_z - G_z - 4}{Y_z + G_z + 4}, \tag{2.33a}$$

$$g = \frac{2Y_z}{4 + Y_z + G_z}. \tag{2.33b}$$

$$\tag{2.33c}$$

2. Let us consider that a voltage pulse V_6^i of unit amplitude is incident upon port 6 of the structure in Fig. 2.4(b). Again, only the circuit of Fig. 2.4(b) must be taken into account. Thus, on the one hand, V_1^r, V_3^r, V_9^r, are obtained from the transmission coefficient,

$$\tau = \frac{2Z_L}{Z_6 + Z_L}, \tag{2.34}$$

which, from a voltage divider, leads to:

$$V_1^r = -\tau\frac{Z_1}{Z_L} = -\frac{2}{2+Z_x+R_x}, \tag{2.35a}$$

$$V_3^r = +\tau\frac{Z_3}{Z_L} = +\frac{2}{2+Z_x+R_x}, \tag{2.35b}$$

$$V_9^r = -\tau\frac{Z_9}{Z_L} = -\frac{2R_x}{2+Z_x+R_x}, \tag{2.35c}$$

$$\tag{2.35d}$$

where $Z_L = Z_1 + Z_3 + Z_9$. In the following, i_x will be the quantity $\frac{2}{2+Z_x+R_x}$. On the other hand, V_6^r is given by the reflection coefficient,

$$\Gamma = \frac{Z_L - Z_6}{Z_L + Z_6}. \tag{2.36}$$

We will refer to this quantity as h_x, which simplifies as:

$$h_x = \frac{2 - Z_x + R_x}{2 + Z_x + R_x}. \tag{2.37}$$

This completes the description of all possibilities.

The complete scattering matrix, which connects the reflected and the incident pulses at the center of a node, according to $V^r = SV^i$, is finally shown to be:

$$S = \begin{bmatrix} a_x & c & b_x & c & g & -i_x & 0 \\ c & a_y & c & b_y & g & 0 & i_y \\ b_x & c & a_x & c & g & i_x & 0 \\ c & b_y & c & a_y & g & 0 & -i_y \\ c & c & c & c & f & 0 & 0 \\ -e_x & 0 & e_x & 0 & 0 & h_x & 0 \\ 0 & e_y & 0 & -e_y & 0 & 0 & h_y \end{bmatrix}. \tag{2.38}$$

The elements of S, given by the preceding development, are summarized in the

following expressions:

$$
\begin{aligned}
a_k &= \tfrac{2}{4+Y_z+G_z} - \tfrac{2}{2+Z_k+R_k}, & f &= \tfrac{Y_z-G_z-4}{Y_z+G_z+4}, \\
b_k &= \tfrac{2}{4+Y_z+G_z} - \tfrac{Z_k+R_k}{2+Z_k+R_k}, & g &= \tfrac{2Y_z}{4+Y_z+G_z}, \\
c &= \tfrac{2}{4+Y_z+G_z}, & h_k &= \tfrac{2-Z_k+R_k}{2+Z_k+R_k}, \\
e_k &= \tfrac{2Z_k}{2+Z_k+R_k}, & i_k &= \tfrac{2}{2+Z_k+R_k},
\end{aligned}
\tag{2.39}
$$

with $k = \{x, y\}$.

A general approach, based on replacing each of the eight transmission lines by a Thevenin equivalent circuit [31], the propagating incident pulse V^i and line being substituted by a voltage source $2V^i$ and a series admittance or impedance, is used to derive the expression of the electromagnetic and magnetic fields. The Thevenin equivalent circuit for the three sub-nodes describing E_z, H_x, and H_y are shown in Fig. 2.5.

Let us first consider Fig. 2.5(a); it consists of a parallel circuit for which each segment represents one of the six ports of the equivalent parallel sub-node depicted in Fig. 2.4(a). From Fig. 2.5(a), we derive the set of equations:

$$
\begin{cases}
V_z = 2V_1^i - I_1 Z_0, \\
V_z = 2V_2^i - I_2 Z_0, \\
V_z = 2V_3^i - I_3 Z_0, \\
V_z = 2V_4^i - I_4 Z_0, \\
V_z = 2V_5^i - I_5 Z_z Z_0, \\
V_z = I_8 Z_8,
\end{cases}
\Rightarrow
\begin{cases}
I_1 = (2V_1^i - V_z) Y_0, \\
I_2 = (2V_2^i - V_z) Y_0, \\
I_3 = (2V_3^i - V_z) Y_0, \\
I_4 = (2V_4^i - V_z) Y_0, \\
I_5 = (2V_5^i - V_z) Y_z Y_0, \\
I_8 = V_z G_z Y_0.
\end{cases}
\tag{2.40}
$$

From Eq. 2.40:

$$
\sum_{i=1}^{5} I_i = 2(V_1^i + V_2^i + V_3^i + V_4^i + Y_z V_5^i) Y_0 - V_z(4Y_0 + Y_z Y_0), \tag{2.41}
$$

and

$$
\sum_{i=1}^{5} I_i = -I_8 = -V_z G_z Y_0. \tag{2.42}
$$

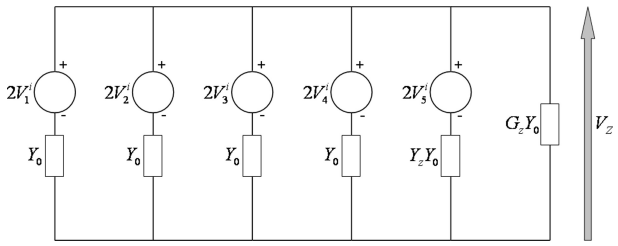

(a) Parallel sub-circuit for the z-component of Ampere's law, i.e, E_z.

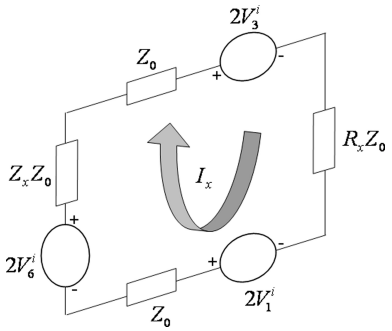

(b) Parallel sub-circuit for the x-component of Faraday's law, i.e, H_x.

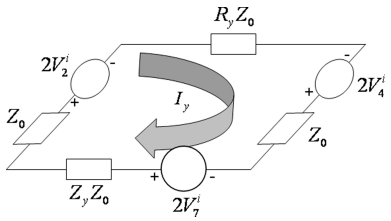

(c) Parallel sub-circuit for the y-component of Faraday's law, i.e, H_y.

Figure 2.5: Splitting of the 2D global node into three sub-circuits.

Equating Eq. 2.41 and Eq. 2.42 gives:

$$V_z = \frac{2(V_1^i + V_2^i + V_3^i + V_4^i + Y_z V_5^i)}{4 + Y_z + G_z}. \tag{2.43}$$

Hence, the electric field is easily obtained by identifying the voltage of Eq. 2.43 per unit length along the z-direction:

$$E_z \equiv \frac{V_z}{\Delta z} = \frac{2(V_1^i + V_2^i + V_3^i + V_4^i + Y_z V_5^i)}{\Delta z(4 + Y_z + G_z)}. \tag{2.44}$$

Let us now consider Fig. 2.5(b); it consists of a series circuit that is equivalent to the series sub-node depicted in Fig. 2.4(b). In Fig. 2.5(b), note that the orientation of the current I_x is chosen along the $-x$ direction. This choice is due to historic reasons and corrects the relation $E_z \equiv \frac{V_z}{\Delta z}$ that should actually be $E_z \equiv -\frac{V_z}{\Delta z}$. But, historically, the electric field has been defined in the literature relative to TLM without the negative sign, we will maintain this criterion. Assuming that, it is plain from Fig. 2.5(b) that

$$I_x = \frac{2(V_1^i - V_3^i + V_6^i)}{2Z_0 + Z_x Z_0 + R_x Z_0}. \tag{2.45}$$

Hence

$$H_x \equiv \frac{I_x}{\Delta x} = \frac{2(V_1^i - V_3^i + V_6^i)}{\Delta x Z_0(2 + Z_x + R_x)}. \tag{2.46}$$

In the same manner, we obtain

$$H_y \equiv \frac{I_y}{\Delta y} = \frac{2(-V_2^i + V_4^i + V_7^i)}{\Delta y Z_0(2 + Z_y + R_y)}. \tag{2.47}$$

In order to excite a particular component of the electromagnetic field, it is necessary to inject a certain voltage into the appropriate ports. For instance, imagine that component E_z has to be excited. In this case, Eq. 2.44 suggests that pulses have to be injected into ports 1, 2, 3, 4, and 5. These pulses must have the same amplitude in order to not excite any magnetic field component. Supposing that

$$V_1^i = V_2^i = V_3^i = V_4^i = V_5^i = \xi_z, \tag{2.48}$$

Eq. 2.44 becomes

$$E_z = \frac{2}{\Delta z}\xi_z, \tag{2.49}$$

which implies that

$$\xi_z = \frac{1}{2}E_z\Delta z\frac{4+Y_z+G_z}{4+Y_z}. \tag{2.50}$$

In the same manner, suppose that only H_x has to be excited and let us assume that

$$V_1^i = -V_3^i = \frac{V_6^i}{Z_x} = \xi_x \Rightarrow H_x = \frac{2}{\Delta x Z_0}\xi_x. \tag{2.51}$$

Obviously, $V_1^i = -V_3^i$ ensures that no electric field is excited.

$$\xi_x = \frac{1}{2}H_x Z_0\Delta x\frac{2+Z_x+R_x}{2+Z_x}. \tag{2.52}$$

is obtained. Finally, let us suppose that only H_y has to be excited and let us assume that

$$-V_2^i = V_4^i = \frac{V_7^i}{Z_y} = \xi_y \Rightarrow H_y = \frac{2}{\Delta y Z_0}\xi_y, \tag{2.53}$$

which leads to

$$\xi_y = \frac{1}{2}H_y Z_0\Delta y\frac{2+Z_y+R_y}{2+Z_y}. \tag{2.54}$$

Therefore, it can be deduced from Eqs. 2.50, 2.52, and 2.54 that a possible set of incident pulses is given by:

$$V_1^i = \frac{1}{2}(\Delta z E_z\frac{4+Y_z+G_z}{4+Y_z} + Z_0\Delta x H_x\frac{2+Z_x+R_x}{2+Z_x}), \tag{2.55a}$$

$$V_2^i = \frac{1}{2}(\Delta z E_z\frac{4+Y_z+G_z}{4+Y_z} - Z_0\Delta y H_y\frac{2+Z_y+R_y}{2+Z_y}), \tag{2.55b}$$

$$V_3^i = \frac{1}{2}(\Delta z E_z\frac{4+Y_z+G_z}{4+Y_z} - Z_0\Delta x H_x\frac{2+Z_x+R_x}{2+Z_x}), \tag{2.55c}$$

$$V_4^i = \frac{1}{2}(\Delta z E_z\frac{4+Y_z+G_z}{4+Y_z} + Z_0\Delta y H_y\frac{2+Z_y+R_y}{2+Z_y}), \tag{2.55d}$$

$$V_5^i = \frac{1}{2}\Delta z E_z\frac{4+Y_z+G_z}{4+Y_z}, \tag{2.55e}$$

$$V_6^i = \frac{1}{2}Z_x Z_0\Delta x H_x\frac{2+Z_x+R_x}{2+Z_x}, \tag{2.55f}$$

$$V_7^i = \frac{1}{2} Z_y Z_0 \Delta y H_y \frac{2 + Z_y + R_y}{2 + Z_y}. \tag{2.55g}$$

This set of equations is very general and takes into account the possibility of locating the source within a dissipative region. If the electromagnetic wave is incident from a lossless region, free space for instance, Eq. 2.55 significantly simplifies since G_z, R_x, and R_y are then equal to zero. The new set of equations becomes:

$$V_1^i = \frac{1}{2}(\Delta z E_z + Z_0 \Delta x H_x), \tag{2.56a}$$

$$V_2^i = \frac{1}{2}(\Delta z E_z - Z_0 \Delta y H_y), \tag{2.56b}$$

$$V_3^i = \frac{1}{2}(\Delta z E_z - Z_0 \Delta x H_x), \tag{2.56c}$$

$$V_4^i = \frac{1}{2}(\Delta z E_z + Z_0 \Delta y H_y), \tag{2.56d}$$

$$V_5^i = \frac{1}{2} \Delta z E_z, \tag{2.56e}$$

$$V_6^i = \frac{1}{2} Z_x Z_0 \Delta x H_x, \tag{2.56f}$$

$$V_7^i = \frac{1}{2} Z_y Z_0 \Delta y H_y. \tag{2.56g}$$

2.3.2 Nodes for transverse magnetic modes

If the components of the incoming electromagnetic wave are $\{E_x, E_y, H_z\}$, the historical description required a series node. As pointed out in section 2.3.1, such an historical description is not capable of dealing with a general situation; we present in this section a more versatile node that we shall call node for TM polarization, or simply TM-node. The TM-node must be regarded as three coupled sub-circuits, as shown in Fig. 2.6.

The series sub-circuit of Fig. 2.6(a) describes the component H_z of the field. It is made up of four main lines (lines 1-4) whose impedance is Z_0 (it is not necessarily that of free space). The sub-circuit is also equipped by an inductive stub (line 5), with impedance $Z_z Z_0$, which allows an independent control of μ_z. Furthermore, magnetic losses (σ_{mz}) are taken into account by an infinitely long lossy stub (line 8), which impedance is $R_z Z_0$.

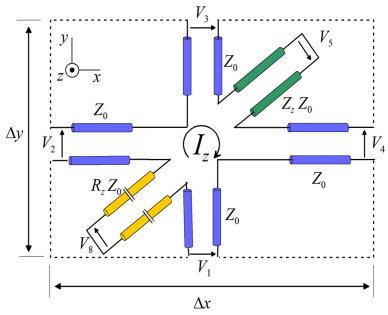

(a) Series sub-circuit for the z-component of Faraday's law to define H_z.

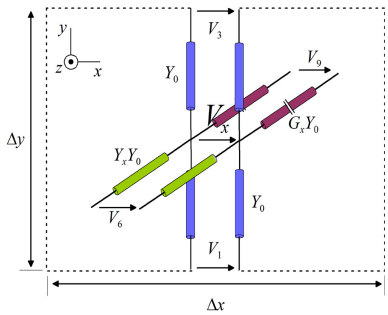

(b) Parallel sub-circuit for the x-component of Ampère's law to define E_x.

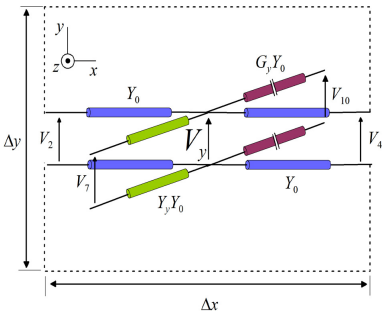

(c) Parallel sub-circuit for the y-component of Ampère's law to define E_y.

Figure 2.6: Splitting of the TM-node into three sub-circuits.

The two parallel sub-circuits depicted in Figs. 2.6(b) and 2.6(c) describe the components H_x and H_y, respectively. Besides the two connecting lines (lines 2 and 4, and 1 and 3), they are each equipped by a capacitive stub (line 6 and 7), with admittance Y_xY_0 and Y_yY_0, respectively. These two capacitive stubs allow an independent control of ε_x and ε_y. Furthermore, electric conductivity (σ_{ex} and σ_{ey}) can be taken into account by adding a lossy stub (line 9 and 10) to each sub-circuit. Their admittances are given by G_xY_0 and G_yY_0, respectively.

Following the same process we used in section 2.3.1 to define the stub parameters for the TE node, we obtain:

$$Y_x = \frac{2\varepsilon_x\varepsilon_0}{Y_0\Delta t}\frac{\Delta y\Delta z}{\Delta x} - 2, \tag{2.57a}$$

$$Y_y = \frac{2\varepsilon_y\varepsilon_0}{Y_0\Delta t}\frac{\Delta x\Delta z}{\Delta y} - 2, \tag{2.57b}$$

$$Z_z = \frac{2\mu_z\mu_0}{Z_0\Delta t}\frac{\Delta x\Delta y}{\Delta z} - 4. \tag{2.57c}$$

The parameters of Eq. 2.57 must be positive, which restricts the choice of Δt and Z_0. Let μ_z^-, ε_x^-, and ε_y^-, be the lowest constitutive parameters of the modeled space. According to Eq. 2.57, we can write that

$$\Delta t \leq \Delta t_x = \frac{\varepsilon_x^-\varepsilon_0}{Y_0}\frac{\Delta y\Delta z}{\Delta x}, \tag{2.58a}$$

$$\Delta t \leq \Delta t_y = \frac{\varepsilon_y^-\varepsilon_0}{Y_0}\frac{\Delta x\Delta z}{\Delta y}, \tag{2.58b}$$

$$\Delta t \leq \Delta t_z = \frac{\mu_z^-\mu_0}{2Z_0}\frac{\Delta x\Delta y}{\Delta z}. \tag{2.58c}$$

In order to eliminate one of the two capacitive stubs,

$$\Delta t = \min(\Delta t_x, \Delta t_y). \tag{2.59}$$

Furthermore, the inductive stub is canceled, i.e. $Z_z = 0$, if the value

$$Z_0 = \frac{1}{2}\frac{\mu_z^-\mu_0}{\Delta t}\frac{\Delta x\Delta y}{\Delta z} \tag{2.60}$$

is selected. If we take into account the choice of Δt, it turns out that

$$Z_0 = \frac{1}{\sqrt{2}}\eta^- \eta_0 \frac{\Delta \iota}{\Delta z}, \tag{2.61}$$

where ι is either x or y depending on the Δt that has been elected, and where $\eta^- = \sqrt{\frac{\mu_z^-}{\varepsilon_i^-}}$. It is possible that η^- be the impedance of no constitutive material of the simulated space; indeed the space with the smallest permittivity and the space with the smallest permeability may no coincide. However, if such a space exists, it should be note that this space in particular is entirely described by using only a single inductive stub if the above Δt and Z_0 are chosen. A situation very often met is $\Delta x = \Delta y = \Delta z = \Delta l$, $\mu_z^- = 1$, $\varepsilon_x^- = 1$, and $\varepsilon_y^- = 1$; in this case,

$$Z_0 = \frac{\eta_0}{\sqrt{2}}, \tag{2.62a}$$

$$\Delta t = \frac{\varepsilon_0 \Delta l}{Y_0}, \tag{2.62b}$$

The process allowing the determination of the scattering matrix, the value of its elements, as well as the expression of the electromagnetic field in terms of the incident pulses, is very similar to the development presented in section 2.3.1. In the following, we simply give the results without demonstration.

For the TM-node, the scattering matrix turns out to be

$$S = \begin{bmatrix} a_x & c & b_x & -c & g & i_x & 0 \\ c & a_y & -c & b_y & -g & 0 & i_y \\ b_x & -c & a_x & c & -g & i_x & 0 \\ -c & b_y & c & a_y & g & 0 & i_y \\ d & -d & -d & d & f & 0 & 0 \\ e_x & 0 & e_x & 0 & 0 & h_x & 0 \\ 0 & e_y & 0 & e_y & 0 & 0 & h_y \end{bmatrix}, \tag{2.63}$$

where

$$
\begin{aligned}
a_k &= \tfrac{2}{2+Y_k+G_k} - \tfrac{2}{4+R_z+Z_z}, & f &= \tfrac{4+R_z-Z_z}{4+R_z+Z_z},\\
b_k &= -\tfrac{Y_k+G_k}{2+Y_k+G_k} + \tfrac{2}{4+R_z+Z_z}, & g &= \tfrac{2}{4+Z_z+R_z},\\
c &= \tfrac{2}{4+Z_z+R_z}, & h_k &= \tfrac{Y_k-2-G_k}{Y_k+2+G_k},\\
d &= \tfrac{2Z_z}{4+Z_z+R_z}, & i_k &= \tfrac{2Y_k}{Y_k+2+G_k},\\
e_k &= \tfrac{2}{2+Y_k+G_k}, &&
\end{aligned}
\tag{2.64}
$$

with $k = \{x, y\}$.

The expression of the electric and magnetic fields in terms of the incident voltage is given by

$$H_z \equiv \frac{I_z}{\Delta z} = \frac{2(-V_1^i + V_2^i + V_3^i - V_4^i + V_5^i)}{\Delta z Z_0 (4 + Z_z + R_z)}, \tag{2.65a}$$

$$E_x \equiv \frac{V_x}{\Delta x} = \frac{2(V_1^i + V_3^i + Y_x V_6^i)}{\Delta x (2 + Y_x + G_x)}, \tag{2.65b}$$

$$E_y \equiv \frac{V_y}{\Delta y} = \frac{2(V_2^i + V_4^i + Y_y V_7^i)}{\Delta y (2 + Y_y + G_y)}. \tag{2.65c}$$

Furthermore, the different ports must be excited according to the following equations

$$V_1^i = \frac{1}{2}(\Delta x E_x \frac{2 + Y_x + G_x}{2 + Y_x} - Z_0 \Delta z H_z \frac{4 + Z_z + R_z}{4 + Z_z}), \tag{2.66a}$$

$$V_2^i = \frac{1}{2}(\Delta y E_y \frac{2 + Y_z + G_z}{2 + Y_z} + Z_0 \Delta z H_z \frac{4 + Z_z + R_z}{4 + Z_z}), \tag{2.66b}$$

$$V_3^i = \frac{1}{2}(\Delta x E_x \frac{2 + Y_z + G_z}{2 + Y_z} + Z_0 \Delta z H_z \frac{4 + Z_z + R_z}{4 + Z_z}), \tag{2.66c}$$

$$V_4^i = \frac{1}{2}(\Delta y E_y \frac{2 + Y_z + G_z}{2 + Y_z} - Z_0 \Delta z H_z \frac{4 + Z_z + R_z}{4 + Z_z}), \tag{2.66d}$$

$$V_5^i = \frac{1}{2} Z_z Z_0 \Delta z H_z \frac{4 + Z_z + R_z}{4 + Z_z}, \tag{2.66e}$$

$$V_6^i = \frac{1}{2}\Delta x E_x \frac{2+Y_x+G_x}{2+Y_x}, \tag{2.66f}$$

$$V_7^i = \frac{1}{2}\Delta y E_y \frac{2+Y_y+G_y}{2+Y_y}; \tag{2.66g}$$

which reduces to

$$V_1^i = \frac{1}{2}(\Delta x E_x - Z_0 \Delta z H_z), \tag{2.67a}$$

$$V_2^i = \frac{1}{2}(\Delta y E_y + Z_0 \Delta z H_z), \tag{2.67b}$$

$$V_3^i = \frac{1}{2}(\Delta x E_x + Z_0 \Delta z H_z), \tag{2.67c}$$

$$V_4^i = \frac{1}{2}(\Delta y E_y - Z_0 \Delta z H_z), \tag{2.67d}$$

$$V_5^i = \frac{1}{2} Z_z Z_0 \Delta z H_z, \tag{2.67e}$$

$$V_6^i = \frac{1}{2}\Delta x E_x, \tag{2.67f}$$

$$V_7^i = \frac{1}{2}\Delta y E_y, \tag{2.67g}$$

if the source is located in a lossless medium.

2.3.3 The symmetrical condensed node

Having a 3D TLM node capable of taking into account all spatial directions is essential. As pointed out in section 2.2, 3D materials have long been simulated by interconnecting 2D series and parallel nodes, leading to a complicated topology of the network [35]. Furthermore, as it is the case for FDTD, the components of the electromagnetic field have the disadvantage to be calculated at points that are spatially separated. Johns introduced the Symmetrical Condensed Node (SCN), a more satisfactory node that has the significant advantage of being totally symmetrical, and allowing the calculation of the components of the electromagnetic field at the same point, i.e., at the center of the node. SCN has roughly been evoked in section 2.2. Because of its neatness and efficiency, other 3D outdated versions are no longer employed.

SCN is depicted in Fig. 2.7. It is represented without stubs, implying that this simple structure, made up of 12 connecting lines, can only represent a cubic

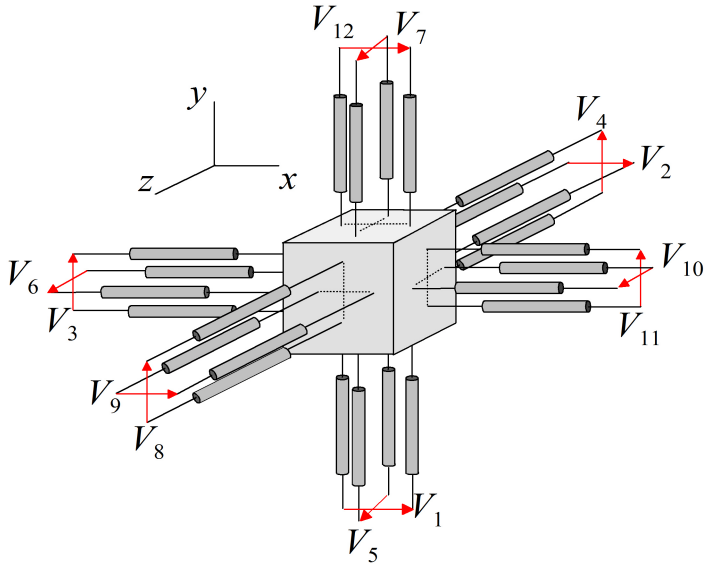

Figure 2.7: The Symmetrical Condensed Node without stubs.

block of homogeneous space. Inhomogeneous and/or lossy problems are solved by equipping SCN with capacitive, inductive, electric-wise lossy, and magnetic-wise lossy stubs. Given the 3Dity of the node, we may add three capacitive and three inductive stubs, capable of providing extra capacitance or inductance, respectively, to the node, to account for ε_x, ε_y, ε_z, μ_x, μ_y, and μ_z; as well as six lossy stubs (infinitely long) to allow independent control on the electric and magnetic conductivity σ_x^e, σ_y^e, σ_z^e, σ_x^m, σ_y^m, and σ_z^m. Therefore, the node, in its most versatile form, has a total of 24 lines. The characteristics of each line, such as its capacitance or inductance (see Eqs. 2.10a and 2.10b), are summarized in Table 2.1. Furthermore, it should be noted that there are two ports, which do not couple with each other, along any direction of propagation that represent the two polarizations (TE or TM). Given the large number of constitutive lines of SCN, it is noteworthy to relate them to Maxwell's equations.

In differential form, the Faraday- and Ampère-Maxwell's equations can be written as:

$$\nabla \times \overline{E}(\bar{r},t) = -\frac{\partial}{\partial t}\overline{B}(\bar{r},t) - \overline{M}(\bar{r},t), \tag{2.68a}$$

Table 2.1: Magnitudes related to the link and stub transmission lines

Line	$\overline{E}$	$\overline{H}$	$\overline{k}$	Capacitance	Inductance
1	$E_x \equiv V_1/\Delta x$	$H_z \equiv -I_1/\Delta z$	y	$Y_0\Delta t/2$	$Z_0\Delta t/2$
2	$E_x \equiv V_2/\Delta x$	$H_y \equiv I_2/\Delta y$	z	$Y_0\Delta t/2$	$Z_0\Delta t/2$
3	$E_y \equiv V_3/\Delta y$	$H_z \equiv I_3/\Delta z$	x	$Y_0\Delta t/2$	$Z_0\Delta t/2$
4	$E_y \equiv V_4/\Delta y$	$H_x \equiv -I_4/\Delta x$	z	$Y_0\Delta t/2$	$Z_0\Delta t/2$
5	$E_z \equiv V_5/\Delta z$	$H_x \equiv I_5/\Delta x$	y	$Y_0\Delta t/2$	$Z_0\Delta t/2$
6	$E_z \equiv V_6/\Delta z$	$H_y \equiv -I_6/\Delta y$	x	$Y_0\Delta t/2$	$Z_0\Delta t/2$
7	$E_z \equiv V_7/\Delta z$	$H_x \equiv -I_7/\Delta x$	y	$Y_0\Delta t/2$	$Z_0\Delta t/2$
8	$E_y \equiv V_8/\Delta y$	$H_x \equiv I_8/\Delta x$	z	$Y_0\Delta t/2$	$Z_0\Delta t/2$
9	$E_x \equiv V_9/\Delta x$	$H_y \equiv -I_9/\Delta y$	z	$Y_0\Delta t/2$	$Z_0\Delta t/2$
10	$E_z \equiv V_{10}/\Delta z$	$H_y \equiv I_{10}/\Delta y$	x	$Y_0\Delta t/2$	$Z_0\Delta t/2$
11	$E_y \equiv V_{11}/\Delta y$	$H_z \equiv -I_{11}/\Delta z$	x	$Y_0\Delta t/2$	$Z_0\Delta t/2$
12	$E_x \equiv V_{12}/\Delta x$	$H_z \equiv I_{12}/\Delta z$	y	$Y_0\Delta t/2$	$Z_0\Delta t/2$
13	$E_x \equiv V_{13}/\Delta y$			$Y_xY_0\Delta t/2$	
14	$E_y \equiv V_{14}/\Delta y$			$Y_yY_0\Delta t/2$	
15	$E_z \equiv V_{15}/\Delta y$			$Y_zY_0\Delta t/2$	
16		$H_x \equiv I_{16}/\Delta x$			$Z_xZ_0\Delta t/2$
17		$H_y \equiv I_{17}/\Delta y$			$Z_yZ_0\Delta t/2$
18		$H_z \equiv I_{18}/\Delta z$			$Z_zZ_0\Delta t/2$
19	$E_x \equiv V_{19}/\Delta y$			$G_xY_0\Delta t/2$	
20	$E_y \equiv V_{20}/\Delta y$			$G_yY_0\Delta t/2$	
21	$E_z \equiv V_{21}/\Delta y$			$G_zY_0\Delta t/2$	
22		$H_x \equiv I_{22}/\Delta x$			$R_xZ_0\Delta t/2$
23		$H_y \equiv I_{23}/\Delta y$			$R_yZ_0\Delta t/2$
24		$H_z \equiv I_{24}/\Delta z$			$R_zZ_0\Delta t/2$

$$\nabla \times \overline{H}(\bar{r},t) = \frac{\partial}{\partial t}\overline{D}(\bar{r},t) + \overline{J}(\bar{r},t), \tag{2.68b}$$

where

$$\begin{aligned} \overline{J}(\bar{r},t) &= \text{electric current density,} \\ \overline{M}(\bar{r},t) &= \text{magnetic current density,} \\ \overline{D}(\bar{r},t) &= \text{electric flux density,} \\ \overline{B}(\bar{r},t) &= \text{magnetic flux density,} \end{aligned}$$

Taking into account the constitutive relations,

$$\overline{D}(\bar{r},t) = \overline{\overline{\varepsilon}}(\bar{r})\varepsilon_0\overline{E}(\bar{r},t), \tag{2.69a}$$
$$\overline{B}(\bar{r},t) = \overline{\overline{\mu}}(\bar{r})\mu_0\overline{H}(\bar{r},t), \tag{2.69b}$$
$$\overline{J}(\bar{r},t) = \overline{\overline{\sigma^e}}(\bar{r})\overline{E}(\bar{r},t), \tag{2.69c}$$
$$\overline{M}(\bar{r},t) = \overline{\overline{\sigma^m}}(\bar{r})\overline{H}(\bar{r},t), \tag{2.69d}$$

Eqs. 2.68a and 2.68b may be expanded in Cartesian coordinates as

$$\frac{\partial E_z}{\partial y} - \frac{\partial E_y}{\partial z} = -\mu_x\mu_0\frac{\partial H_x}{\partial t} - \sigma_x^m H_x, \tag{2.70a}$$
$$\frac{\partial E_x}{\partial z} - \frac{\partial E_z}{\partial x} = -\mu_y\mu_0\frac{\partial H_y}{\partial t} - \sigma_y^m H_y, \tag{2.70b}$$
$$\frac{\partial E_y}{\partial x} - \frac{\partial E_x}{\partial y} = -\mu_z\mu_0\frac{\partial H_z}{\partial t} - -\sigma_z^m H_z, \tag{2.70c}$$
$$\frac{\partial H_z}{\partial y} - \frac{\partial H_y}{\partial z} = \varepsilon_x\varepsilon_0\frac{\partial E_x}{\partial t} + \sigma_x^e E_x, \tag{2.70d}$$
$$\frac{\partial H_x}{\partial z} - \frac{\partial H_z}{\partial x} = \varepsilon_y\varepsilon_0\frac{\partial E_y}{\partial t} + \sigma_y^e E_y, \tag{2.70e}$$
$$\frac{\partial H_y}{\partial x} - \frac{\partial H_x}{\partial y} = \varepsilon_z\varepsilon_0\frac{\partial E_z}{\partial t} + \sigma_z^e E_z. \tag{2.70f}$$

Following the same process as in section 2.3.1, let us now suppose that a voltage pulse $V_1^i = 1$ enters port 1 of the structure in Fig. 2.7. In agreement with Table 2.1, this pulse is associated with $\{E_x, H_z, k_y\}$, and consequently scatters into ports 1, 12, 13, 18, 19, and 24. From the description resulting from Maxwell's equations, E_x and H_z appear together in Eqs. 2.70c and 2.70d, in which they couple with other components:

1. According to the former equation, $\{E_x, H_y\}$ is also involved, meaning that

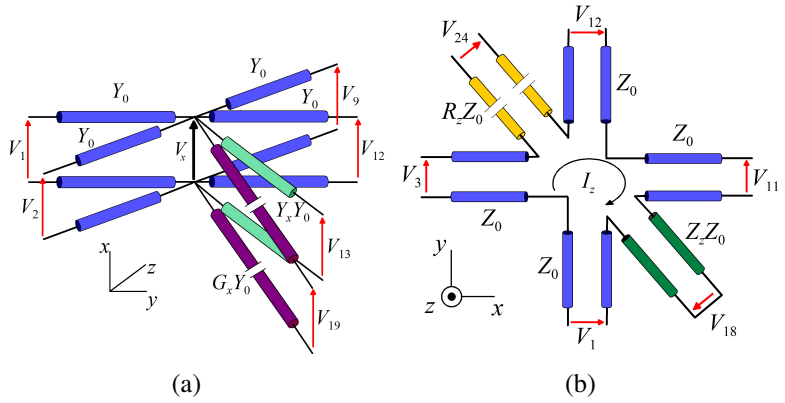

Figure 2.8: (a) Parallel sub-circuit for E_x. (b) Series sub-circuit for H_z.

the pulse is scattered into the ports associated with these magnitudes, i.e., 2 and 9.

2. According to the latter equation, $\{E_y, H_z\}$ is also involved, and the pulse is consequently scattered into the ports associated with these magnitudes, i.e., 3 and 11.

It is precisely this multiple coupling between the components of the electromagnetic field that pushed P. B. Johns to claim that a break should be made with the traditional representation of the node by an equivalent circuit [29], as mentioned in section 2.2. Actually, the coupling between Maxwell's equations may be treated by coupling electrical circuits as described in sections 2.3.1 and 2.3.2. As a result, SCN can be represented by six coupled sub-circuits, each one corresponding to a component of the electromagnetic field. Actually, an individual sub-circuit represents an individual Maxwell's equation in the set of Eqs. 2.70. In our current example, exciting V_1 involves the two sub-circuits depicted in Figs. 2.8(a) and 2.8(b). The former figure represents Eq. 2.70d, while the latter represents Eq. 2.70c.

By identifying the fields with their electrical analogs according to Table 2.1, we can transform Eq. 2.70d to its finite difference form:

$$\begin{aligned} &\frac{\left(\frac{I_{12}}{\Delta z}\right)-\left(-\frac{I_1}{\Delta z}\right)}{\Delta y}-\frac{\left(-\frac{I_9}{\Delta y}\right)-\left(\frac{I_2}{\Delta y}\right)}{\Delta z}=\varepsilon_x\varepsilon_0\frac{\partial\frac{V_x}{\Delta x}}{\partial t}+\sigma_x^e\frac{V_x}{\Delta x} \\ \Rightarrow &I_1+I_2+I_9+I_{12}=\varepsilon_x\varepsilon_0\frac{\Delta y\Delta z}{\Delta x}\frac{\partial V_x}{\partial t}+\sigma_x^e\frac{\Delta y\Delta z}{\Delta x}V_x. \end{aligned} \tag{2.71}$$

This equation establishes the current loss in lines 1, 2, 9, and 12, which is due to charge accumulation in the capacitive stubs. By using the analogy with the usual relation $I = C\frac{\partial V}{\partial t}$, we can naturally define the capacitive term

$$C_x = \varepsilon_x \varepsilon_0 \frac{\Delta y \Delta z}{\Delta x}, \tag{2.72}$$

which demonstrates for the x-component Eq. 2.6a that was previously introduced. C_y (from Eq. 2.70e) and C_z (from Eq. 2.70f) are similarly obtained. Moreover, the value of the characteristic admittance of the electric lossy stub, G_x, which derives from Eq. 2.71, is given by Eq. 2.73a

$$G_x = \frac{\sigma_x^e}{Y_0} \frac{\Delta y \Delta z}{\Delta x}, \tag{2.73a}$$

$$G_y = \frac{\sigma_y^e}{Y_0} \frac{\Delta x \Delta z}{\Delta y}, \tag{2.73b}$$

$$G_z = \frac{\sigma_z^e}{Y_0} \frac{\Delta x \Delta y}{\Delta z}. \tag{2.73c}$$

while Eqs. 2.73b and 2.73c are obtained by considering the other components, Eqs. 2.70e and 2.70f, of Ampère's equations.

In the same manner, we transform Eq. 2.70c as:

$$\begin{aligned} &\frac{(\frac{V_{11}}{\Delta y}) - (\frac{V_3}{\Delta y})}{\Delta x} - \frac{(\frac{V_{12}}{\Delta x}) - (\frac{V_1}{\Delta x})}{\Delta y} = -\mu_z \mu_0 \frac{\partial \frac{I_z}{\Delta z}}{\partial t} - \sigma_z^m \frac{I_z}{\Delta z} \\ \Rightarrow &V_1 - V_3 + V_{11} - V_{12} = -\mu_z \mu_0 \frac{\Delta x \Delta y}{\Delta z} \frac{\partial I_z}{\partial t} + \sigma_z^m \frac{\Delta x \Delta y}{\Delta z} I_z, \end{aligned} \tag{2.74}$$

which provides the relations

$$L_z = \mu_z \mu_0 \frac{\Delta x \Delta y}{\Delta z} \tag{2.75}$$

by using $V = L\frac{\partial I}{\partial t}$. The process would be similar to get L_x and L_y. This expression was already given, without demonstration, in Eq. 2.6b. As well, the expression of

R_z can be obtained and is given in Eq. 2.76c:

$$R_x = \frac{\sigma_x^m}{Z_0}\frac{\Delta y \Delta z}{\Delta x}, \tag{2.76a}$$

$$R_y = \frac{\sigma_y^m}{Z_0}\frac{\Delta x \Delta z}{\Delta y}, \tag{2.76b}$$

$$R_z = \frac{\sigma_z^m}{Z_0}\frac{\Delta x \Delta y}{\Delta z}; \tag{2.76c}$$

R_x and R_y are also given and their derivation follows the same process using Eqs. 2.70a and 2.70b. Note that Eq. 2.74 describes the discontinuity of the potential due to the inductive stubs.

The scattering matrix, S, is derived using the method of common and uncommon lines [30], as in section 2.3.1. Since, no pulse can return from the lossy stub, S is a 18×18 matrix.

1. **Uncommon lines: pulse incident from a link line of the parallel sub-circuit of Fig. 2.8(a).** When entering port 1, V_1^i connects to an effective admittance

$$Y_L = Y_2 + Y_9 + Y_{12} + Y_{13} + Y_{19} = 3Y_0 + Y_x Y_0 + G_x Y_0, \tag{2.77}$$

which is the load admittance. Let τ be the transmission coefficient,

$$\tau = \frac{2Y_1}{Y_1 + Y_L}; \tag{2.78}$$

V_1^i is simply scattered into the uncommon lines (the ones which are not involved in the series circuit of Fig. 2.8(b)), i.e., 2, 9, 13, and 19, with an amplitude we will refer to as c_x,

$$c_x = V_2^r = V_9^r = V_{13}^r = V_{19}^r = \tau = \frac{2}{4 + Y_x + G_x}. \tag{2.79}$$

2. **Uncommon lines: pulse incident from a link line of the series sub-circuit of Fig. 2.8(b).** V_1^i connects to a load impedance given by

$$Z_L = Z_3 + Z_{11} + Z_{12} + Z_{18} + Z_{24} = 3Z_0 + Z_z Z_0 + R_z Z_0. \tag{2.80}$$

The transmission coefficient is given by

$$\tau = \frac{2Z_L}{Z_1 + Z_L}. \tag{2.81}$$

V_1^i spreads out into the uncommon lines 3 (with amplitude d_z), 11 (with amplitude $-d_z$), 18 (with amplitude e_z), and 24 (no need to assign it a name) according to a simple voltage division

$$d_z = V_3^r = -V_{11}^r = \tau\frac{Z_0}{Z_L} = \frac{2}{4 + Z_z + R_z}, \tag{2.82a}$$

$$e_z = V_{18}^r = \tau\frac{Z_z Z_0}{Z_L} = \frac{2Z_z}{4 + Z_z + R_z}, \tag{2.82b}$$

$$V_{24}^r = \tau\frac{R_z Z_0}{Z_L} = \frac{2R_z}{4 + Z_z + R_z}. \tag{2.82c}$$

3. **Common lines to both sub-circuits.** Since lines 1 and 12 are common to both circuits, their coupling requires another method to determine how V_1^i scatters into them. Let a_{xz} and b_{xz} be the amplitude of the pulses scattered into port 1 and 12, respectively. Note the two subscripts denoting that these two magnitudes are involved in both E_x- and H_z-sub-circuits. More practically, the two subscripts are useful to make the distinction between pulses which could be incident from other ports. For example, in the case of a pulse incident from port 2 of the structure of Fig. 2.8(a), the series circuit of Fig. 2.8(b) would no be longer involved. Instead, the pertinent series sub-circuit would be that associated with H_y, meaning that the amplitudes would be a_{xy} and b_{xy}. This parenthesis being finished, the charge conservation at the parallel sub-circuit ensures that

$$\begin{aligned} I_1^i &= I_1^r + I_2^r + I_9^r + I_{12}^r + I_{13}^r + I_{19}^r \\ \Rightarrow Y_0 &= a_{xz}Y_0 + 2c_xY_0 + b_{xz}Y_0 + c_xY_xY_0 + V_{19}^r G_x Y_0, \end{aligned} \tag{2.83}$$

while continuity of potential at the series sub-circuit yields

$$\begin{aligned} -V_1 + V_3 - V_{11} + V_{12} + V_{18} + V_{24} &= 0 \\ \Rightarrow -(1 + a_{xz}) + 2d_z + b_{xz} + e_z + V_{24}^r &= 0. \end{aligned} \tag{2.84}$$

Simultaneously solving these two equations leads to

$$a_{xz} = -\frac{Y_x + G_x}{2(4 + Y_x + G_x)} + \frac{Z_z + R_z}{2(4 + Z_z + R_z)}, \tag{2.85a}$$

$$b_{xz} = -\frac{Y_x + G_x}{2(4 + Y_x + G_x)} - \frac{Z_z + R_z}{2(4 + Z_z + R_z)}. \tag{2.85b}$$

4. **Pulse incident from a stub line of the parallel sub-circuit of Fig. 2.8(a).** Let us suppose now that a voltage pulse $V_{13}^i = 1$ is incident upon the capacitive stub, i.e., port 13 of the structure in Fig. 2.8(a). This pulse connects to a load admittance determined by

$$Y_L = Y_1 + Y_2 + Y_9 + Y_{12} + Y_{19} = 4Y_0 + G_x Y_0, \tag{2.86}$$

while the reflection and transmission coefficient are

$$\Gamma = \frac{Y_{13} - Y_L}{Y_{13} + Y_L}, \tag{2.87a}$$

$$\tau = \frac{2Y_{13}}{Y_{13} + Y_L}, \tag{2.87b}$$

respectively. Since no other coupled circuit must be accounted for, V_{13}^i is simply reflected into port 13, with a magnitude we will refer to as f_x, so that

$$f_x = V_{13}^r = \Gamma = \frac{Y_x - 4 - G_x}{Y_x + 4 + G_x}, \tag{2.88}$$

while it is scattered, with magnitude g_x, into the other involved ports, i.e., 1, 2, 9, 12, and 19 according to

$$g_x = V_1^r = V_2^r = V_9^r = V_{12}^r = V_{19}^r = \tau = \frac{2Y_x}{Y_x + 4 + G_x}, \tag{2.89}$$

although it was not necessary to mention V_{19}^r given that it does not enter into account for S.

5. **Pulse incident from a stub line of the series sub-circuit of Fig. 2.8(b).** A pulse $V_{18}^i = 1$, which sees a load impedance

$$Z_L = Z_1 + Z_3 + Z_{11} + Z_{12} + Z_{24} = 4Z_0 + R_z Z_0, \tag{2.90}$$

is incident from the inductive stub, i.e., port 18. The reflection and transmission coefficients are

$$\Gamma = \frac{Z_L - Z_{18}}{Z_L + Z_{18}}, \tag{2.91a}$$

$$\tau = \frac{2Z_L}{Z_L + Z_{18}}, \tag{2.91b}$$

respectively. Again, no other coupled circuits must be regarded, which means that this pair of coefficients completely define the scattered pulses. Let h_z be the amplitude scattered back into port 18, we find

$$h_z = V_{18}^r = \Gamma = \frac{4 - Z_z + R_z}{4 + Z_z + R_z}. \tag{2.92}$$

V_{18}^i is scattered into ports 1 (with amplitude i_z), 3 (with amplitude $-i_z$), 11 (with amplitude i_z), and 12 (with amplitude $-i_z$) according to a simple voltage division

$$i_z = V_1^r = -V_3^r = V_{11}^r = -V_{12}^r = \frac{Z_0}{Z_L}\tau = \frac{2}{4 + Z_z + R_z}, \tag{2.93}$$

This completes the description of all possibilities. If the incoming pulse is incident from other ports, the process to get the scattering at the center of the node is rigourously the same. We can thus write the scattering matrix as

$$\begin{bmatrix}
a_{xz} & c_x & d_z & 0 & 0 & 0 & 0 & 0 & c_x & 0 & -d_z & b_{xz} & g_x & 0 & 0 & 0 & 0 & i_z \\
c_x & a_{xy} & 0 & 0 & 0 & d_y & 0 & 0 & b_{xy} & -d_y & 0 & c_x & g_x & 0 & 0 & 0 & -i_y & 0 \\
d_z & 0 & a_{yz} & c_y & 0 & 0 & 0 & c_y & 0 & 0 & b_{yz} & -d_z & 0 & g_y & 0 & 0 & 0 & -i_z \\
0 & 0 & c_y & a_{yx} & d_x & 0 & -d_x & b_{yx} & 0 & 0 & c_y & 0 & 0 & g_y & 0 & i_x & 0 & 0 \\
0 & 0 & 0 & d_x & a_{zx} & c_z & b_{zx} & -d_x & 0 & c_z & 0 & 0 & 0 & 0 & g_z & -i_x & 0 & 0 \\
0 & d_y & 0 & 0 & c_z & a_{zy} & c_z & 0 & -d_y & b_{zy} & 0 & 0 & 0 & 0 & g_z & 0 & i_y & 0 \\
0 & 0 & 0 & -d_x & b_{zx} & c_z & a_{zx} & d_x & 0 & c_z & 0 & 0 & 0 & 0 & g_z & i_x & 0 & 0 \\
0 & 0 & c_y & b_{yx} & -d_x & 0 & d_x & a_{yx} & 0 & 0 & c_y & 0 & 0 & g_y & 0 & -i_x & 0 & 0 \\
c_x & b_{xy} & 0 & 0 & 0 & -d_y & 0 & 0 & a_{xy} & d_y & 0 & c_x & g_x & 0 & 0 & 0 & i_y & 0 \\
0 & -d_y & 0 & 0 & c_z & b_{zy} & c_z & 0 & d_y & a_{zy} & 0 & 0 & 0 & 0 & g_z & 0 & -i_y & 0 \\
-d_z & 0 & b_{yz} & c_y & 0 & 0 & 0 & c_y & 0 & 0 & a_{yz} & d_z & 0 & g_y & 0 & 0 & 0 & i_z \\
b_{xz} & c_x & -d_z & 0 & 0 & 0 & 0 & 0 & c_x & 0 & d_z & a_{xz} & g_x & 0 & 0 & 0 & 0 & -i_z \\
c_x & c_x & 0 & 0 & 0 & 0 & 0 & 0 & c_x & 0 & 0 & c_x & f_x & 0 & 0 & 0 & 0 & 0 \\
0 & 0 & c_y & c_y & 0 & 0 & 0 & c_y & 0 & 0 & c_y & 0 & 0 & f_y & 0 & 0 & 0 & 0 \\
0 & 0 & 0 & 0 & c_z & c_z & c_z & 0 & 0 & c_z & 0 & 0 & 0 & 0 & f_z & 0 & 0 & 0 \\
0 & 0 & 0 & e_x & -e_x & 0 & e_x & -e_x & 0 & 0 & 0 & 0 & 0 & 0 & 0 & h_x & 0 & 0 \\
0 & -e_y & 0 & 0 & 0 & e_y & 0 & 0 & e_y & -e_y & 0 & 0 & 0 & 0 & 0 & 0 & h_y & 0 \\
e_z & 0 & -e_z & 0 & 0 & 0 & 0 & 0 & 0 & 0 & e_z & -e_z & 0 & 0 & 0 & 0 & 0 & h_z
\end{bmatrix}, \tag{2.94}$$

where the elements of the matrix S are hereinafter summarized:

$$
\begin{aligned}
a_{pq} &= -\tfrac{Y_p+G_p}{2(4+Y_p+G_p)} + \tfrac{Z_q+R_q}{2(4+Z_q+R_q)}, & f_p &= \tfrac{-4+Y_p-G_p}{4+Y_p+G_p}, \\
b_{pq} &= -\tfrac{Y_p+G_p}{2(4+Y_p+G_p)} - \tfrac{Z_q+R_q}{2(4+Z_q+R_q)}, & g_p &= \tfrac{2Y_p}{4+Y_p+G_p}, \\
c_p &= \tfrac{2}{4+Y_p+G_p}, & h_q &= \tfrac{4-Z_q+R_q}{4+Z_q+R_q}, \\
d_q &= \tfrac{2}{4+Z_q+R_q}, & i_q &= \tfrac{2}{4+Z_q+R_q}, \\
e_q &= \tfrac{2Z_q}{4+Z_q+R_q}, &&
\end{aligned}
\tag{2.95}
$$

with $(p,q) = \{x,y\}$.

In agreement with Table 2.1, and Eq. 2.72 and Eq. 2.75, the total capacitance associated with lines 1, 2, 9, 12, and 13 for the parallel circuit depicted in Fig. 2.8(a), and the total inductance associated with lines 1, 3, 11, 12, and 18 for the series circuit depicted in Fig. 2.8(b), are given by

$$C_x = \varepsilon_x \varepsilon_0 \frac{\Delta y \Delta z}{\Delta x} = 4Y_0 \frac{\Delta t}{2} + Y_x Y_0 \frac{\Delta t}{2}, \tag{2.96a}$$

$$L_z = \mu_z \mu_0 \frac{\Delta x \Delta y}{\Delta z} = 4Z_0 \frac{\Delta t}{2} + Z_z Z_0 \frac{\Delta t}{2}, \tag{2.96b}$$

respectively. Generalizing to the other coordinates, we can get the form of the admittances and impedances of the capacitive and inductive stubs, respectively:

$$Y_x = \frac{2\varepsilon_x \varepsilon_0}{Y_0 \Delta t} \frac{\Delta y \Delta z}{\Delta x} - 4, \tag{2.97a}$$

$$Y_y = \frac{2\varepsilon_y \varepsilon_0}{Y_0 \Delta t} \frac{\Delta x \Delta z}{\Delta y} - 4, \tag{2.97b}$$

$$Y_z = \frac{2\varepsilon_z \varepsilon_0}{Y_0 \Delta t} \frac{\Delta x \Delta y}{\Delta z} - 4, \tag{2.97c}$$

$$Z_x = \frac{2\mu_x \mu_0}{Z_0 \Delta t} \frac{\Delta y \Delta z}{\Delta x} - 4, \tag{2.97d}$$

$$Z_y = \frac{2\mu_y \mu_0}{Z_0 \Delta t} \frac{\Delta x \Delta z}{\Delta y} - 4, \tag{2.97e}$$

$$Z_z = \frac{2\mu_z \mu_0}{Z_0 \Delta t} \frac{\Delta x \Delta y}{\Delta z} - 4. \tag{2.97f}$$

All these magnitudes must be positive, which is of direct consequence on $Z_0 = 1/Y_0$ and Δt. In particular, the latter must be selected such that:

$$\Delta t \leq \Delta t_x^C = \frac{\varepsilon_x^- \varepsilon_0}{2Y_0} \frac{\Delta y \Delta z}{\Delta x}, \tag{2.98a}$$

$$\Delta t \leq \Delta t_y^C = \frac{\varepsilon_y^- \varepsilon_0}{2Y_0} \frac{\Delta x \Delta z}{\Delta y}, \tag{2.98b}$$

$$\Delta t \leq \Delta t_z^C = \frac{\varepsilon_z^- \varepsilon_0}{2Y_0} \frac{\Delta x \Delta y}{\Delta z}, \tag{2.98c}$$

$$\Delta t \leq \Delta t_x^L = \frac{\mu_x^- \mu_0}{2Z_0} \frac{\Delta y \Delta z}{\Delta x}, \tag{2.98d}$$

$$\Delta t \leq \Delta t_y^L = \frac{\mu_y^- \mu_0}{2Z_0} \frac{\Delta x \Delta z}{\Delta y}, \tag{2.98e}$$

$$\Delta t \leq \Delta t_z^L = \frac{\mu_z^- \mu_0}{2Z_0} \frac{\Delta x \Delta y}{\Delta z}, \tag{2.98f}$$

in order to ensure the impedances and admittances of the stubs to be positive; the superscript "$-$" denotes the lowest permittivity or permeability along a certain direction. A good choice for Δt and Z_0 would be to cancel one capacitive and one inductive stubs, so that only four parameters of Eq. 2.97 would be nonzero. To do so, we may proceed as follow:

1. The choice,
$$\Delta t = \min(\Delta t_x^C, \Delta t_y^C, \Delta t_z^C) \tag{2.99}$$
eliminates either Y_x, Y_y, or Y_z, ensuring that one of the three capacitive stubs is eliminated, while the others are positive.

2. Z_0 is chosen such that either Z_x, Z_y, or Z_z become zero. This choice ensures that one of the three inductive stubs is eliminated, while the others are positive.

In a space involving free space, which is a likely situation, $\varepsilon_x^- = \varepsilon_y^- = \varepsilon_z^- = \mu_x^- = \mu_y^- = \mu_z^- = 1$. Moreover, if $\Delta x = \Delta y = \Delta z = \Delta l$, we get

$$Z_0 = \eta_0, \tag{2.100a}$$

$$\Delta t = \frac{1}{2} \frac{\varepsilon_0}{Y_0} \Delta l, \tag{2.100b}$$

Note that the impedance Z_0 is that of free space in this case.

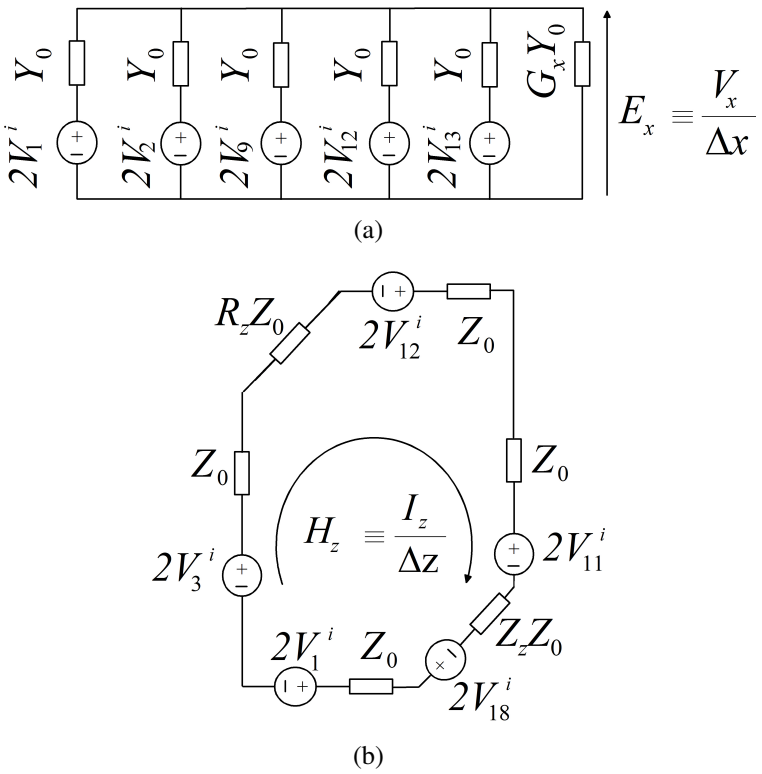

Figure 2.9: (a) Thevenin representation of the shunt E_x-sub-circuit depicted in Fig. 2.8(a).(b) Thevenin representation of the series H_z-sub-circuit depicted in Fig. 2.8(b). It should be noted that there is no incident tension for the lossy stubs, i.e., lines 19 and 24

In order to express the electric and magnetic fields in terms of the incident pulses, the Thevenin representation of the structures in Fig. 2.11 should be considered, as pointed out in section 2.3.1. Therefore, the expressions of E_x and H_z are easily derived using the process explained in section 2.3.1; generalizing to the other components of the electromagnetic field, we obtain:

$$E_x \equiv \frac{V_x}{\Delta x} = \frac{2(V_1^i + V_2^i + V_9^i + V_{12}^i + Y_x V_{13}^i)}{\Delta x(4 + Y_x + G_x)}, \tag{2.101a}$$

$$E_y \equiv \frac{V_y}{\Delta y} = \frac{2(V_3^i + V_4^i + V_8^i + V_{11}^i + Y_y V_{14}^i)}{\Delta y(4 + Y_y + G_y)}, \tag{2.101b}$$

$$E_z \equiv \frac{V_z}{\Delta z} = \frac{2(V_5^i + V_6^i + V_7^i + V_{10}^i + Y_z V_{15}^i)}{\Delta z(4 + Y_z + G_z)}, \tag{2.101c}$$

$$H_x \equiv \frac{I_x}{\Delta x} = \frac{2(-V_4^i + V_5^i - V_7^i + V_8^i + V_{16}^i)}{Z_0 \Delta x (4 + Z_x + R_x)}, \tag{2.101d}$$

$$H_y \equiv \frac{I_y}{\Delta y} = \frac{2(V_2^i - V_6^i - V_9^i + V_{10}^i + V_{17}^i)}{Z_0 \Delta y (4 + Z_y + R_y)}, \tag{2.101e}$$

$$H_z \equiv \frac{I_z}{\Delta z} = \frac{2(-V_1^i + V_3^i - V_{11}^i + V_{12}^i + V_{18}^i)}{Z_0 \Delta z (4 + Z_z + R_z)}, \tag{2.101f}$$

Note that the individual components of the electromagnetic field can be determined without consideration of the Thevenin equivalents. Indeed, the total charge that is injected to the node in Fig. 2.8(a) can be written as,

$$Q_i = C_1 V_1^i + C_2 V_2^i + C_9 V_9^i + C_{12} V_{12}^i + C_{13} V_{13}^i + C_{19} V_{19}^i. \tag{2.102}$$

According to Table 2.1 and since $V_{19}^i = 0$, we get

$$Q_i = \frac{Y_0 \Delta t}{2} (V_1^i + V_2^i + V_9^i + V_{12}^i + V_{13}^i). \tag{2.103}$$

Conservation of current (or charge) means that the total charge leaving the ports is also given by Eq. 2.103; therefore, the total charge that is located into the node during the whole time step is

$$Q = 2Q_i = Y_0 \Delta t (V_1^i + V_2^i + V_9^i + V_{12}^i + V_{13}^i). \tag{2.104}$$

On the other hand, the total capacitance modeled by the six constitutive transmission lines is

$$C_x = \frac{Y_0 \Delta t}{2} (4 + Y_x + G_x). \tag{2.105}$$

Thus, the electric field is

$$E_x = \frac{Q}{\Delta x C_x} = \frac{2(V_1^i + V_2^i + V_9^i + V_{12}^i + Y_x V_{13}^i)}{\Delta x (4 + Y_x + G_x)}, \tag{2.106}$$

which is the relation obtained in Eq. 2.101.

Similarly, considering Fig. 2.8(b), the incident magnetic flux that reaches the plane $z = cte$ is

$$\Phi_i = -L_1 I_1^i + L_3 I_3^i - L_{11} I_{11}^i + L_{12} I_{12}^i + L_{18} I_{18}^i + L_{24} I_{24}^i. \tag{2.107}$$

Since $I_i^i = V_i^i/Z_i$ and $I_{24}^i = 0$, we get

$$\Phi_i = \frac{\Delta t}{2}(-V_1^i + V_3^i - V_{11}^i + V_{12}^i + V_{18}^i). \tag{2.108}$$

The magnetic flux must be conserved; thus, the total magnetic flux that is involved during the whole time step is

$$\Phi = \Delta t(-V_1^i + V_3^i - V_{11}^i + V_{12}^i + V_{18}^i). \tag{2.109}$$

On the other hand, the total inductance modeled by the six constitutive transmission lines is

$$L_z = \frac{Z_0 \Delta t}{2}(4 + Z_z + R_z). \tag{2.110}$$

Hence, the magnetic field is

$$H_z = \frac{\Phi}{\Delta z L_z} = \frac{2(-V_1^i + V_3^i - V_{11}^i + V_{12}^i + V_{18}^i)}{Z_0 \Delta z(4 + Z_z + R_z)}. \tag{2.111}$$

which is the relation obtained in Eq. 2.101.

With the technique employed in section 2.3.1, we can determine the set of incident pulses to excite the desired separate field components of $\overline{E}$ and $\overline{H}$:

$$V_1^i = \frac{1}{2}(\Delta x E_x \frac{4 + Y_x + G_x}{4 + Y_x} - \Delta z Z_0 H_z \frac{4 + Z_z + R_z}{4 + Z_z}), \tag{2.112a}$$

$$V_2^i = \frac{1}{2}(\Delta x E_x \frac{4 + Y_x + G_x}{4 + Y_x} + \Delta y Z_0 H_y \frac{4 + Z_y + R_y}{4 + Z_y}), \tag{2.112b}$$

$$V_3^i = \frac{1}{2}(\Delta y E_y \frac{4 + Y_y + G_y}{4 + Y_y} + \Delta z Z_0 H_z \frac{4 + Z_z + R_z}{4 + Z_z}), \tag{2.112c}$$

$$V_4^i = \frac{1}{2}(\Delta y E_y \frac{4 + Y_y + G_y}{4 + Y_y} - \Delta x Z_0 H_x \frac{4 + Z_x + R_x}{4 + Z_x}), \tag{2.112d}$$

$$V_5^i = \frac{1}{2}(\Delta z E_z \frac{4 + Y_z + G_z}{4 + Y_z} + \Delta x Z_0 H_x \frac{4 + Z_x + R_x}{4 + Z_x}), \tag{2.112e}$$

$$V_6^i = \frac{1}{2}(\Delta z E_z \frac{4 + Y_z + G_z}{4 + Y_z} - \Delta y Z_0 H_y \frac{4 + Z_y + R_y}{4 + Z_y}), \tag{2.112f}$$

$$V_7^i = \frac{1}{2}(\Delta z E_z \frac{4 + Y_z + G_z}{4 + Y_z} - \Delta x Z_0 H_x \frac{4 + Z_x + R_x}{4 + Z_x}), \tag{2.112g}$$

$$V_8^i = \frac{1}{2}(\Delta y E_y \frac{4 + Y_y + G_y}{4 + Y_y} + \Delta x Z_0 H_x \frac{4 + Z_x + R_x}{4 + Z_x}), \tag{2.112h}$$

$$V_9^i = \frac{1}{2}(\Delta x E_x \frac{4+Y_x+G_x}{4+Y_x} - \Delta y Z_0 H_y \frac{4+Z_y+R_y}{4+Z_y}), \tag{2.112i}$$

$$V_{10}^i = \frac{1}{2}(\Delta z E_z \frac{4+Y_z+G_z}{4+Y_z} + \Delta y Z_0 H_y \frac{4+Z_y+R_y}{4+Z_y}), \tag{2.112j}$$

$$V_{11}^i = \frac{1}{2}(\Delta y E_y \frac{4+Y_y+G_y}{4+Y_y} - \Delta z Z_0 H_z \frac{4+Z_z+R_z}{4+Z_z}), \tag{2.112k}$$

$$V_{12}^i = \frac{1}{2}(\Delta x E_x \frac{4+Y_x+G_x}{4+Y_x} + \Delta z Z_0 H_z \frac{4+Z_z+R_z}{4+Z_z}), \tag{2.112l}$$

$$V_{13}^i = \frac{1}{2}\Delta x E_x \frac{4+Y_x+G_x}{4+Y_x}, \tag{2.112m}$$

$$V_{14}^i = \frac{1}{2}\Delta y E_y \frac{4+Y_y+G_y}{4+Y_y}, \tag{2.112n}$$

$$V_{15}^i = \frac{1}{2}\Delta z E_z \frac{4+Y_z+G_z}{4+Y_z}, \tag{2.112o}$$

$$V_{16}^i = \frac{1}{2}Z_x Z_0 \Delta x H_x \frac{4+Z_x+R_x}{4+Z_x}, \tag{2.112p}$$

$$V_{17}^i = \frac{1}{2}Z_y Z_0 \Delta y H_y \frac{4+Z_y+R_y}{4+Z_y}, \tag{2.112q}$$

$$V_{18}^i = \frac{1}{2}Z_z Z_0 \Delta z H_z \frac{4+Z_z+R_z}{4+Z_z}. \tag{2.112r}$$

Note that Eq. 2.112 is general and holds if the source is located in a lossy region of the space. If the mesh is excited in a lossless region, $G = R = 0$, and Eq. 2.112 dramatically simplifies.

2.4 TLM curved nodes

The Cartesian TLM nodes presented in sections 2.3.1, 2.3.2, and 2.3.3 are well-suited to model square or cubic shaped blocks of space. However, chapter 4 will be dedicated to the study of cylindrical and spherical cloaking structures. Modeling curved geometries with Cartesian nodes can be accomplished by approximating the curved boundary by a staircase shaped boundary. Ensuring that the size of the node is small compared to the wavelength should not alter the correctness of the obtained results. On the other hand, it is intuitively obvious that curved TLM nodes can better match the current geometry. In this chapter, the cylindrical nodes for TE and TM polarizations, as well as the spherical node, will be presented. The resulting meshes, made up of a large number of such nodes,

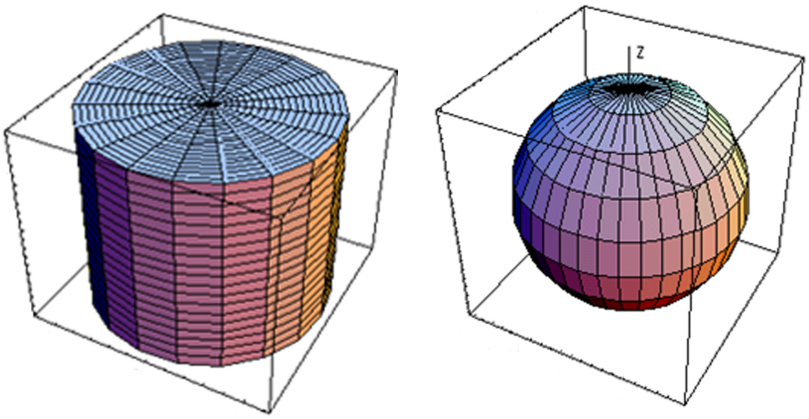

(a) (b)

Figure 2.10: (a) Mesh made up of cylindrical nodes. (b) Mesh made up of spherical nodes.

can be viewed in Fig. 2.10. This approach can be profitable in many aspects. The step-wise approximation is eliminated and, furthermore, the number of nodes that fills the mesh can be significantly reduced. However, we will show in this section that the resulting curved mesh is variable, i.e., the TLM parameters, like the impedance of the stubs, depend on the radial coordinates. As a result, this can force the time-step to be very small because the impedance of the stubs must be positive everywhere (except if metamaterial is under consideration), lengthening thus the computational requirement. Moreover, the nodes become bigger towards the outer boundary of the mesh, thus the condition in Eq. 2.11, $\lambda \geq 10\Delta l$, decreases the maximum allowed frequency, f_{max}. To conclude, curved nodes should not be systematically preferred in simulations involving cylindrical or spherical symmetry. Therefore, there use should be carefully considered; nevertheless, if all the necessary conditions are fulfilled, the benefit in employing curved nodes to model curved shape can be very important. This will be illustrated in section 4.6.1.

2.4.1 Cylindrical nodes for transverse electric modes

In order to become cylindrical, the Cartesian nodes that involve the $\{x, y, z\}$ coordinates have to be transform into the $\{r, \varphi, z\}$ coordinates. The following

equivalence between both coordinate systems

$$\begin{cases} x \leftrightarrow r, \\ y \leftrightarrow \varphi, \\ z \leftrightarrow z, \end{cases} \quad \Rightarrow \quad \begin{cases} \Delta x \leftrightarrow \Delta r, \\ \Delta y \leftrightarrow r\Delta\varphi, \\ \Delta z \leftrightarrow \Delta z, \end{cases} \tag{2.113}$$

permits the transformation. Eq. 2.113 accounts for all the details of the new geometry and formally constitutes the only modification to the Cartesian two-dimensional nodes presented in sections 2.3.1 and 2.3.2. All the new quantities of interest are simply obtained from those previously calculated in the former and latter sections, but we have to take into account the substitution imposed by Eq. 2.113. The new expressions are given in the following paragraph.

Let us first consider the cylindrical node for TE modes. Eq. 2.12 becomes

$$Z_r = \frac{2\mu_r\mu_0}{Z_0\Delta t}\frac{r\Delta\varphi\Delta z}{\Delta r} - 2, \tag{2.114a}$$

$$Z_\varphi = \frac{2\mu_\varphi\mu_0}{Z_0\Delta t}\frac{\Delta r\Delta z}{r\Delta\varphi} - 2, \tag{2.114b}$$

$$Y_z = \frac{2\varepsilon_z\varepsilon_0}{Y_0\Delta t}\frac{r\Delta\varphi\Delta r}{\Delta z} - 4, \tag{2.114c}$$

while Eqs. 2.76a, 2.76b, and 2.73c become

$$R_r = \frac{\sigma_r^m}{Z_0}\frac{r\Delta\varphi\Delta z}{\Delta r}, \tag{2.115a}$$

$$R_\varphi = \frac{\sigma_\varphi^m}{Z_0}\frac{\Delta r\Delta z}{r\Delta\varphi}, \tag{2.115b}$$

$$G_z = \frac{\sigma_z^e}{Y_0}\frac{r\Delta\varphi\Delta r}{\Delta z}, \tag{2.115c}$$

respectively.

It is plain from Eqs. 2.114 and 2.115 that these parameters are variable, the values of the stubs directly depend on the position, r, of the nodes. It is worth emphasizing this property of the cylindrical nodes; indeed, the Cartesian nodes did not behave that way, the possible non-homogeneity of the simulated medium resulted in the values of the stubs to be variable within the mesh, but for a certain homogeneous medium the values of the stubs were constant. This statement is no longer valid for cylindrical nodes, and each node is expected to be unique along

the radial direction. This is of direct consequence on the time-step, Δt, given that Eq. 2.13 becomes

$$\Delta t \leq \Delta t_r = \frac{\bar{\mu_r}\mu_0}{Z_0}\frac{r\Delta\varphi\Delta z}{\Delta r}, \tag{2.116a}$$

$$\Delta t \leq \Delta t_\varphi = \frac{\bar{\mu_\varphi}\mu_0}{Z_0}\frac{\Delta r\Delta z}{r\Delta\varphi}, \tag{2.116b}$$

$$\Delta t \leq \Delta t_z = \frac{\bar{\varepsilon_z}\varepsilon_0}{2Y_0}\frac{r\Delta\varphi\Delta r}{\Delta z}. \tag{2.116c}$$

Accordingly, Δt can be forced to be very small because of the r-dependence of these formulas.

The scattering matrix that was given by Eq. 6.5 becomes

$$S = \begin{bmatrix} a_r & c & b_r & c & g & -i_r & 0 \\ c & a_\varphi & c & b_\varphi & g & 0 & i_\varphi \\ b_r & c & a_r & c & g & i_r & 0 \\ c & b_\varphi & c & a_\varphi & g & 0 & -i_\varphi \\ c & c & c & c & f & 0 & 0 \\ -e_r & 0 & e_r & 0 & 0 & h_r & 0 \\ 0 & e_\varphi & 0 & -e_\varphi & 0 & 0 & h_\varphi \end{bmatrix}. \tag{2.117}$$

The expression of the matrix elements is almost unchanged compared to Eq. 6.6. We can write

$$\begin{aligned} a_k &= \tfrac{2}{4+Y_z+G_z} - \tfrac{2}{2+Z_k+R_k}, & f &= \tfrac{Y_z-G_z-4}{Y_z+G_z+4}, \\ b_k &= \tfrac{2}{4+Y_z+G_z} - \tfrac{Z_k+R_k}{2+Z_k+R_k}, & g &= \tfrac{2Y_z}{4+Y_z+G_z}, \\ c &= \tfrac{2}{4+Y_z+G_z}, & h_k &= \tfrac{2-Z_k+R_k}{2+Z_k+R_k}, \\ e_k &= \tfrac{2Z_k}{2+Z_k+R_k}, & i_k &= \tfrac{2}{2+Z_k+R_k}, \end{aligned} \tag{2.118}$$

with $k = \{r, \varphi\}$; the only modification being the value of k.

The expression of the electromagnetic field in terms of the incident pulses

becomes

$$H_r = \frac{2(V_1^i - V_3^i + V_6^i)}{\Delta r Z_0 (2 + Z_r + R_r)}, \tag{2.119a}$$

$$H_\varphi = \frac{2(-V_2^i + V_4^i + V_7^i)}{r\Delta\varphi Z_0 (2 + Z_\varphi + R_\varphi)}, \tag{2.119b}$$

$$E_z = \frac{2(V_1^i + V_2^i + V_3^i + V_4^i + Y_z V_5^i)}{\Delta z (4 + Y_z + G_z)}. \tag{2.119c}$$

Furthermore, if the source is located in a lossless medium, the set

$$V_1^i = \frac{1}{2}(\Delta z E_z + Z_0 \Delta r H_r), \tag{2.120a}$$

$$V_2^i = \frac{1}{2}(\Delta z E_z - Z_0 r \Delta\varphi H_\varphi), \tag{2.120b}$$

$$V_3^i = \frac{1}{2}(\Delta z E_z - Z_0 \Delta r H_r), \tag{2.120c}$$

$$V_4^i = \frac{1}{2}(\Delta z E_z + Z_0 r \Delta\varphi H_\varphi), \tag{2.120d}$$

$$V_5^i = \frac{1}{2}\Delta z E_z, \tag{2.120e}$$

$$V_6^i = \frac{1}{2} Z_r Z_0 \Delta r H_r, \tag{2.120f}$$

$$V_7^i = \frac{1}{2} Z_\varphi Z_0 r \Delta\varphi H_\varphi. \tag{2.120g}$$

should substitute Eq. 2.56.

2.4.2 Cylindrical nodes for transverse magnetic modes

The cylindrical node for TM modes directly derives from the Cartesian TM node, presented in section 2.4.2, by using the transformation given by Eq. 2.113.

Eq. 2.57 becomes

$$Y_r = \frac{2\varepsilon_r \varepsilon_0}{Y_0 \Delta t} \frac{r\Delta\varphi\Delta z}{\Delta r} - 2, \tag{2.121a}$$

$$Y_\varphi = \frac{2\varepsilon_\varphi \varepsilon_0}{Y_0 \Delta t} \frac{\Delta r \Delta z}{r\Delta\varphi} - 2, \tag{2.121b}$$

$$Z_z = \frac{2\mu_z\mu_0}{Z_0\Delta t}\frac{r\Delta\varphi\Delta r}{\Delta z} - 4, \tag{2.121c}$$

while Eqs. 2.73a, 2.73b, and 2.76c become

$$G_r = \frac{\sigma_r^e}{Y_0}\frac{r\Delta\varphi\Delta z}{\Delta r}, \tag{2.122a}$$

$$G_\varphi = \frac{\sigma_\varphi^e}{Y_0}\frac{\Delta r\Delta z}{r\Delta\varphi}, \tag{2.122b}$$

$$R_z = \frac{\sigma_z^m}{Z_0}\frac{r\Delta\varphi\Delta r}{\Delta z}, \tag{2.122c}$$

respectively.

Again, note that Eqs. 2.121 and 2.122 are r-dependent, as well as the condition on Δt,

$$\Delta t \leq \Delta t_r = \frac{\bar{\varepsilon_r}\varepsilon_0}{Y_0}\frac{r\Delta\varphi\Delta z}{\Delta r}, \tag{2.123a}$$

$$\Delta t \leq \Delta t_\varphi = \frac{\bar{\varepsilon_\varphi}\varepsilon_0}{Y_0}\frac{\Delta r\Delta z}{r\Delta\varphi}, \tag{2.123b}$$

$$\Delta t \leq \Delta t_z = \frac{\bar{\mu_z}\mu_0}{2Z_0}\frac{r\Delta\varphi\Delta r}{\Delta z}. \tag{2.123c}$$

The scattering matrix given by Eq. 2.63 thus becomes

$$S = \begin{bmatrix} a_r & c & b_r & -c & g & i_r & 0 \\ c & a_\varphi & -c & b_\varphi & -g & 0 & i_\varphi \\ b_r & -c & a_r & c & -g & i_r & 0 \\ -c & b_\varphi & c & a_\varphi & g & 0 & i_\varphi \\ d & -d & -d & d & f & 0 & 0 \\ e_r & 0 & e_r & 0 & 0 & h_r & 0 \\ 0 & e_\varphi & 0 & e_\varphi & 0 & 0 & h_\varphi \end{bmatrix}, \tag{2.124}$$

where

$$
\begin{aligned}
a_k &= \tfrac{2}{2+Y_k+G_k} - \tfrac{2}{4+R_z+Z_z}, & f &= \tfrac{4+R_z-Z_z}{4+R_z+Z_z},\\
b_k &= -\tfrac{Y_k+G_k}{2+Y_k+G_k} + \tfrac{2}{4+R_z+Z_z}, & g &= \tfrac{2}{4+Z_z+R_z},\\
c &= \tfrac{2}{4+Z_z+R_z}, & h_k &= \tfrac{Y_k-2-G_k}{Y_k+2+G_k},\\
d &= \tfrac{2Z_z}{4+Z_z+R_z}, & i_k &= \tfrac{2Y_k}{Y_k+2+G_k},\\
e_k &= \tfrac{2}{2+Y_k+G_k}, &&
\end{aligned}
\tag{2.125}
$$

with $k = \{r, \varphi\}$.

The expressions of the electromagnetic field's component in terms of the incident pulses can be written as

$$E_r = \frac{2(V_1^i + V_3^i + Y_r V_6^i)}{\Delta r(2 + Y_r + G_r)}, \tag{2.126a}$$

$$E_\varphi = \frac{2(V_2^i + V_4^i + Y_y V_7^i)}{r\Delta\varphi(2 + Y_\varphi + G_\varphi)}, \tag{2.126b}$$

$$H_z = \frac{2(-V_1^i + V_2^i + V_3^i - V_4^i + V_5^i)}{\Delta z Z_0(4 + Z_z + R_z)}, \tag{2.126c}$$

Furthermore, if the source is located in a lossless medium, the voltage components

$$V_1^i = \frac{1}{2}(\Delta r E_r - Z_0 \Delta z H_z), \tag{2.127a}$$

$$V_2^i = \frac{1}{2}(r\Delta y E_\varphi + Z_0 \Delta z H_z), \tag{2.127b}$$

$$V_3^i = \frac{1}{2}(\Delta r E_r + Z_0 \Delta z H_z), \tag{2.127c}$$

$$V_4^i = \frac{1}{2}(r\Delta y E_\varphi - Z_0 \Delta z H_z), \tag{2.127d}$$

$$V_5^i = \frac{1}{2} Z_z Z_0 \Delta z H_z, \tag{2.127e}$$

$$V_6^i = \frac{1}{2}\Delta r E_r, \tag{2.127f}$$

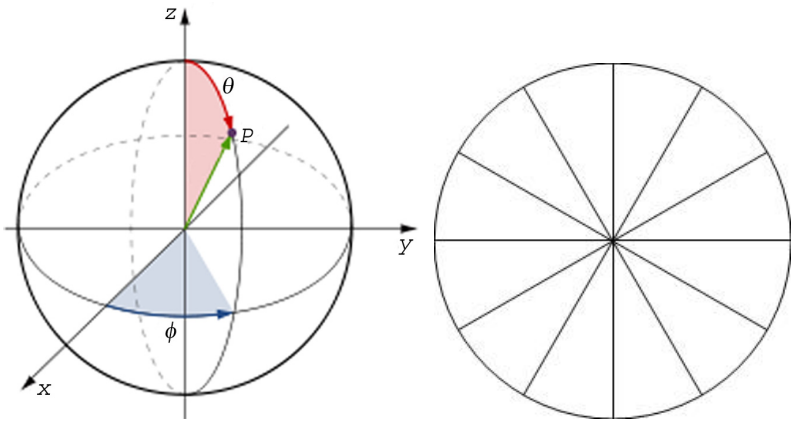

(a) (b)

Figure 2.11: (a) The spherical coordinate system. rajouter *r* (b) Upper view of the pole, $\theta = 0$.

$$V_7^i = \frac{1}{2} r \Delta\varphi E_\varphi, \tag{2.127g}$$

should substitute Eq. 2.67.

2.4.3 The spherical node

First, the spherical coordinate system is shown in Fig. 2.11(a). To describe spherical shapes, the symmetrical condensed node presented in section 2.3.3 has to be transformed from the $\{x, y, z\}$ Cartesian coordinates into the $\{r, \theta, \varphi\}$ spherical coordinate system. The following equivalence between both coordinate systems

$$\begin{cases} x \leftrightarrow \varphi, \\ y \leftrightarrow r, \\ z \leftrightarrow \theta, \end{cases} \quad \Rightarrow \quad \begin{cases} \Delta x \leftrightarrow r \sin\theta \Delta\varphi, \\ \Delta y \leftrightarrow \Delta r, \\ \Delta z \leftrightarrow r \Delta\theta, \end{cases} \tag{2.128}$$

permits the transformation. As for the cylindrical nodes, all the new quantities of interest for the spherical node are simply obtained from those previously calculated for Cartesian coordinates (section 2.3.3), but taking into account the substitution imposed by Eq. 2.128. The obtained spherical node is represented in Fig. 2.12, and in the following, the expressions related to this new node are given and discussed.

Eq. 2.97 becomes

$$Y_\varphi = \frac{2\varepsilon_\varphi \varepsilon_0}{Y_0 \Delta t} \frac{\Delta r \Delta\theta}{\sin\theta \Delta\varphi} - 4, \tag{2.129a}$$

$$Y_r = \frac{2\varepsilon_r \varepsilon_0}{Y_0 \Delta t} \frac{r^2 \sin\theta \Delta\varphi \Delta\theta}{\Delta r} - 4, \tag{2.129b}$$

$$Y_\theta = \frac{2\varepsilon_\theta \varepsilon_0}{Y_0 \Delta t} \frac{\sin\theta \Delta\varphi \Delta r}{\Delta\theta} - 4, \tag{2.129c}$$

$$Z_\varphi = \frac{2\mu_\varphi \mu_0}{Z_0 \Delta t} \frac{\Delta r \Delta\theta}{\sin\theta \Delta\varphi} - 4, \tag{2.129d}$$

$$Z_r = \frac{2\mu_y \mu_r}{Z_0 \Delta t} \frac{r^2 \sin\theta \Delta\varphi \Delta\theta}{\Delta r} - 4, \tag{2.129e}$$

$$Z_\theta = \frac{2\mu_\theta \mu_0}{Z_0 \Delta t} \frac{\sin\theta \Delta\varphi \Delta r}{\Delta\theta} - 4, \tag{2.129f}$$

while Eqs. 2.73 and 2.76 should be changed into

$$G_\varphi = \frac{\sigma_\varphi^e}{Y_0} \frac{\Delta r \Delta\theta}{\sin\theta \Delta\varphi}, \tag{2.130a}$$

$$G_r = \frac{\sigma_r^e}{Y_0} \frac{r^2 \sin\theta \Delta\varphi \Delta\theta}{\Delta r}, \tag{2.130b}$$

$$G_\theta = \frac{\sigma_\theta^e}{Y_0} \frac{\sin\theta \Delta\varphi \Delta r}{\Delta\theta}, \tag{2.130c}$$

$$R_\varphi = \frac{\sigma_\varphi^m}{Z_0} \frac{\Delta r \Delta\theta}{\sin\theta \Delta\varphi}, \tag{2.130d}$$

$$R_r = \frac{\sigma_r^m}{Z_0} \frac{r^2 \sin\theta \Delta\varphi \Delta\theta}{\Delta r}, \tag{2.130e}$$

$$R_\theta = \frac{\sigma_\theta^m}{Z_0} \frac{\sin\theta \Delta\varphi \Delta r}{\Delta\theta}. \tag{2.130f}$$

The form of Eqs. 2.129 and 2.130 is even more singular than that relative to the cylindrical nodes. Indeed, the values of the stubs depend on the radial coordinates, r, as well as on the zenithal one, θ, even for a homogeneous medium. This property of the spherical node is of direct consequence on the time-step, Δt; indeed, Eq. 2.98 becomes

$$\Delta t \leq \frac{\bar{\varepsilon_\varphi} \varepsilon_0}{2Y_0} \frac{\Delta r \Delta\theta}{\sin\theta \Delta\varphi}, \tag{2.131a}$$

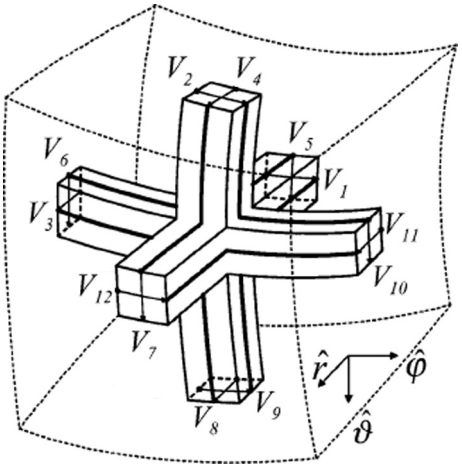

Figure 2.12: The TLM spherical symmetrical condensed node.

$$\Delta t \leq \frac{\varepsilon_r^- \varepsilon_0}{2Y_0} \frac{r^2 \sin\theta \Delta\varphi \Delta\theta}{\Delta r}, \tag{2.131b}$$

$$\Delta t \leq \frac{\varepsilon_\theta^- \varepsilon_0}{2Y_0} \frac{\sin\theta \Delta\varphi \Delta r}{\Delta\theta}, \tag{2.131c}$$

$$\Delta t \leq \frac{\mu_\varphi^- \mu_0}{2Z_0} \frac{\Delta r \Delta\theta}{\sin\theta \Delta\varphi}, \tag{2.131d}$$

$$\Delta t \leq \frac{\mu_r^- \mu_0}{2Z_0} \frac{r^2 \sin\theta \Delta\varphi \Delta\theta}{\Delta r}, \tag{2.131e}$$

$$\Delta t \leq \frac{\mu_\theta^- \mu_0}{2Z_0} \frac{\sin\theta \Delta\varphi \Delta r}{\Delta\theta}. \tag{2.131f}$$

Accordingly, Δt can be forced to be very small because of the r- and $\sin\theta$-dependence of these formulas.

Beyond this difficulty in selecting the optimum Δt, it is worth emphasizing the singularity of the spherical mesh at $\theta = 0$, i.e., at its poles. It is plain from Fig. 2.10(b) that there is convergence of nodes at the poles. The configuration at this point is displayed in Fig. 2.11(b) for 12 nodes along the azimuth, φ. The connection, along the centripetal radial direction, between the transmission lines that point toward the pole (line 1 and 5 for the transformation of Eq. 2.128) is conflictive given that the concept of adjacent nodes is meaningless at this particular point. This raises the following questions. How should we connect these transmission lines between each other? What is the termination of the ports of

the nodes that point towards the pole? The easiest solution would be to connect the lines that face each other. This option is only an approximation since nothing ensures that the pulses incoming from a certain line will be transmitted into the opposite one. A second solution would be to define a transfer matrix at the pole that would be capable of correctly distributing the energy. Finally, a third solution would be to locate a special TLM node whose center exactly coincides with the pole; the derivation of the scattering matrix associated to this node constituting the difficulty of this option. In any case, more analysis is required to rigorously figure out how to make the connection at the pole. In this dissertation, we will use the first and simplest option.

The scattering matrix of the spherical node is easily derived from Eq. 2.94 by substituting the subscripts according to Eq. 2.128.

The expression of the electromagnetic field in terms of the incident voltage pulses becomes

$$E_\varphi \equiv \frac{V_\varphi}{r\sin\theta\Delta\varphi} = \frac{2(V_1^i + V_2^i + V_9^i + V_{12}^i + Y_\varphi V_{13}^i)}{r\sin\theta\Delta\varphi(4+Y_\varphi+G_\varphi)}, \tag{2.132a}$$

$$E_r \equiv \frac{V_r}{\Delta r} = \frac{2(V_3^i + V_4^i + V_8^i + V_{11}^i + Y_r V_{14}^i)}{\Delta r(4+Y_r+G_r)}, \tag{2.132b}$$

$$E_\theta \equiv \frac{V_{r\Delta\theta}}{\Delta z} = \frac{2(V_5^i + V_6^i + V_7^i + V_{10}^i + Y_\theta V_{15}^i)}{r\Delta\theta(4+Y_z+G_z)}, \tag{2.132c}$$

$$H_\varphi \equiv \frac{I_\varphi}{r\sin\theta\Delta\varphi} = \frac{2(-V_4^i + V_5^i - V_7^i + V_8^i + V_{16}^i)}{Z_0 r\sin\theta\Delta\varphi(4+Z_\varphi+R_\varphi)}, \tag{2.132d}$$

$$H_r \equiv \frac{I_r}{\Delta r} = \frac{2(V_2^i - V_6^i - V_9^i + V_{10}^i + V_{17}^i)}{Z_0\Delta r(4+Z_r+R_r)}, \tag{2.132e}$$

$$H_\theta \equiv \frac{I_\theta}{r\Delta\theta} = \frac{2(-V_1^i + V_3^i - V_{11}^i + V_{12}^i + V_{18}^i)}{Z_0 r\Delta\theta(4+Z_\theta+R_\theta)}, \tag{2.132f}$$

Finally, the voltage set

$$V_1^i = \frac{1}{2}(r\sin\theta\Delta\varphi E_\varphi \frac{4+Y_\varphi+G_\varphi}{4+Y_\varphi} - r\Delta\theta Z_0 H_\theta \frac{4+Z_\theta+R_\theta}{4+Z_\theta}), \tag{2.133a}$$

$$V_2^i = \frac{1}{2}(r\sin\theta\Delta\varphi E_\varphi \frac{4+Y_\varphi+G_\varphi}{4+Y_\varphi} + \Delta r Z_0 H_r \frac{4+Z_r+R_r}{4+Z_r}), \tag{2.133b}$$

$$V_3^i = \frac{1}{2}(\Delta r E_r \frac{4+Y_r+G_r}{4+Y_r} + r\Delta\theta Z_0 H_\theta \frac{4+Z_\theta+R_\theta}{4+Z_\theta}), \tag{2.133c}$$

$$V_4^i = \frac{1}{2}(\Delta r E_r \frac{4+Y_r+G_r}{4+Y_r} - r\sin\theta\Delta\varphi Z_0 H_\varphi \frac{4+Z_\varphi+R_\varphi}{4+Z_\varphi}), \tag{2.133d}$$

$$V_5^i = \frac{1}{2}(r\Delta\theta E_\theta \frac{4+Y_\theta+G_\theta}{4+Y_\theta} + r\sin\theta\Delta\varphi Z_0 H_\varphi \frac{4+Z_\varphi+R_\varphi}{4+Z_\varphi}), \tag{2.133e}$$

$$V_6^i = \frac{1}{2}(r\Delta\theta E_\theta \frac{4+Y_\theta+G_\theta}{4+Y_\theta} - \Delta r Z_0 H_r \frac{4+Z_r+R_r}{4+Z_r}), \tag{2.133f}$$

$$V_7^i = \frac{1}{2}(r\Delta\theta E_\theta \frac{4+Y_\theta+G_\theta}{4+Y_\theta} - r\sin\theta\Delta\varphi Z_0 H_\varphi \frac{4+Z_\varphi+R_\varphi}{4+Z_\varphi}), \tag{2.133g}$$

$$V_8^i = \frac{1}{2}(\Delta r E_r \frac{4+Y_r+G_r}{4+Y_r} + r\sin\theta\Delta\varphi Z_0 H_\varphi \frac{4+Z_\varphi+R_\varphi}{4+Z_\varphi}), \tag{2.133h}$$

$$V_9^i = \frac{1}{2}(r\sin\theta\Delta\varphi E_\varphi \frac{4+Y_\varphi+G_\varphi}{4+Y_\varphi} - \Delta r Z_0 H_r \frac{4+Z_r+R_r}{4+Z_r}), \tag{2.133i}$$

$$V_{10}^i = \frac{1}{2}(r\Delta\theta E_\theta \frac{4+Y_\theta+G_\theta}{4+Y_\theta} + \Delta r Z_0 H_r \frac{4+Z_r+R_r}{4+Z_r}), \tag{2.133j}$$

$$V_{11}^i = \frac{1}{2}(\Delta r E_r \frac{4+Y_r+G_r}{4+Y_r} - r\Delta\theta Z_0 H_\theta \frac{4+Z_\theta+R_\theta}{4+Z_\theta}), \tag{2.133k}$$

$$V_{12}^i = \frac{1}{2}(r\sin\theta\Delta\varphi E_\varphi \frac{4+Y_\varphi+G_\varphi}{4+Y_\varphi} + r\Delta\theta Z_0 H_\theta \frac{4+Z_\theta+R_\theta}{4+Z_\theta}), \tag{2.133l}$$

$$V_{13}^i = \frac{1}{2} r\sin\theta\Delta\varphi E_\varphi \frac{4+Y_\varphi+G_\varphi}{4+Y_\varphi}, \tag{2.133m}$$

$$V_{14}^i = \frac{1}{2}\Delta r E_r \frac{4+Y_r+G_r}{4+Y_r}, \tag{2.133n}$$

$$V_{15}^i = \frac{1}{2} r\Delta\theta E_\theta \frac{4+Y_\theta+G_\theta}{4+Y_\theta}, \tag{2.133o}$$

$$V_{16}^i = \frac{1}{2} Z_\varphi Z_0 r\sin\theta\Delta\varphi H_\varphi \frac{4+Z_\varphi+R_\varphi}{4+Z_\varphi}, \tag{2.133p}$$

$$V_{17}^i = \frac{1}{2} Z_r Z_0 \Delta r H_r \frac{4+Z_r+R_r}{4+Z_r}, \tag{2.133q}$$

$$V_{18}^i = \frac{1}{2} Z_z Z_0 r\Delta\theta H_\theta \frac{4+Z_\theta+R_\theta}{4+Z_\theta}. \tag{2.133r}$$

should substitute Eq. 2.112. if the source is located in a lossless medium, $G = R = 0$, and Eq. 2.133 significantly simplifies.

2.5 Modeling of metamaterials with TLM

An electromagnetic metamaterial can be defined as an artificial homogeneous electromagnetic structure whose properties are not available in nature. The history of metamaterials started with the pioneering work proposed by V. G. Veselago who theoretically investigated plane wave propagation in a material that exhibits negative values for both the permittivity and permeability. He proved that the Poynting vector of a monochromatic plane wave propagating in such a media is antiparallel with respect of the direction of its phase velocity. This unusual behavior inspired him to call them left-handed (LH) materials. It should be understood that LH materials belong to a certain class of metamaterials, and are sometimes called negative refractive index media, backward-wave media, or double negative media to name, few terminologies. In this thesis we refer to any exotic electromagnetic materials as metamaterials. For more than 30 years after Veselago's work, metamaterials received very little attention, until D. R. Smith *et al.* realized composite media. These were based on a periodic array of interspaced conducting nonmagnetic split ring resonators [36] and continuous wires [37], that exhibits a frequency region in the microwave regime with simultaneously negative values of effective permeability and permittivity [38]. Since then, contributions on this topic have been plentiful, prompted by a variety of promising optical and microwave applications. Another approach that exploits an $L-C$ distributed network was proposed by Eleftheriades *et al.* [39], as an alternate perspective to the split ring resonators and continuous wires approach previously mentioned. Given that a TLM node can be represented by lumped inductors and capacitors [1], the transmission line approach is naturally of great interest.

As early as 1944, G. Kron [27] stressed the ability of distributed $L-C$ circuit networks for representing natural media by means of the direct analogy between circuit equations and Maxwell's equations. A unit cell of such a network is depicted in Fig. 2.13(a).

The possibility of backward electromagnetic waves in an $L-C$ network is briefly described in S. Ramo's book for instance [40]. The equivalent circuit, represented in Fig. 2.13(b), that supports such backward waves can be referred to as a dual $L-C$ network given that it differs from the original one in the position of L and C, which are simply interchanged. The analogy between the conventional backward wave phenomenon and the propagation of electromagnetic waves in metamaterials, naturally leads to the transmission line approach of negative refractive index media. More information about this analogy can be found

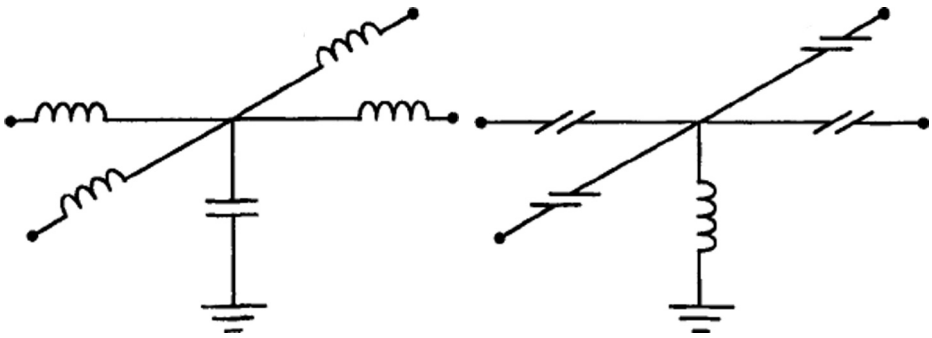

Figure 2.13: (a) Unit cell of an $L-C$ network describing usual media. (b) Unit cell of a dual $L-C$ network describing exotic media.

in [41, 42].

Recognizing that TLM is nothing more than the numerical incarnation of an $L-C$ network, So *et al.* presented a technique that allows the modeling of metamaterials based on the transmission line approach [43]. However, their new nodes requires a significant modification of the impulse scattering process when compared to the classical version, as they, themselves, pointed out in their innovative contribution. Considering that metamaterials are on the cutting-edge of current research, it is of great interest to render more comfortable the TLM modeling involving left-handed media. We have shown in two articles that such a drastic modification is actually not necessary [15, 16].

The positive quantities C and L, which represent an equivalent to the permittivity and permeability, respectively, should be made negative to account for the left-handedness. Referring to Fig. 2.5, the series inductor thus becomes a series capacitor, while the shunt capacitor becomes a shunt inductor. Let us now consider a capacitor with capacity C and an inductor with inductance L, the associated impedances being $Z_C = \frac{1}{j\omega C}$ and $Z_L = j\omega L$, respectively. Let us assume that $L = -\frac{1}{\omega^2 C}$. In this manner, $Z_L = j\omega L = -\frac{j\omega}{\omega^2 C} = \frac{1}{j\omega C}$ which is precisely Z_C. We can intuitively conclude that a capacitor is equivalent to a negative inductor whose inductance is

$$L_{eq} = -\frac{1}{\omega^2 C}. \tag{2.134}$$

However, the inductance is no longer constant, instead it is an explicit function of frequency. For the purpose of illustration, consider the series sub-circuit of SCN depicted in Fig. 2.8(b) that describes the z-component of the magnetic field.

In its original form, it is equipped with a positive inductive stub, line 18, whose inductance is $L = Z_z Z_0 \frac{\Delta t}{2}$ according to Table 2.1; Z_z being the impedance of the stub. Imagine that the positive inductive stub is substituted by a negative one; as mentioned before, the new stub adds a capacitance C to the node and, moreover, $C = Y_z Y_0 \frac{\Delta t}{2}$, as usual. According to Eq. 2.134,

$$\begin{aligned} L_{eq} &= -\frac{1}{\omega^2 Y_z Y_0 \frac{\Delta t}{2}} \\ &= -Z_z Z_0 \frac{2}{\Delta t \omega^2}. \end{aligned} \tag{2.135}$$

Furthermore, Eq. 2.96b becomes

$$4 Z_0 \frac{\Delta t}{2} + L_{eq} = \mu_z \mu_0 \frac{\Delta x \Delta y}{\Delta z} \tag{2.136}$$

with L_{eq} given by Eq. 2.135; we finally calculate the new expression of the stub's impedance:

$$Z_z(\omega) = -\frac{1}{4} \Delta t^2 \omega^2 [\frac{2\mu_z \mu_0}{Z_0 \Delta t} \frac{\Delta x \Delta y}{\Delta z} - 4]. \tag{2.137}$$

We remind that the usual value for Z_z is given by Eq. 2.97f:

$$Z_z = \frac{2\mu_z \mu_0}{Z_0 \Delta t} \frac{\Delta x \Delta y}{\Delta z} - 4. \tag{2.138}$$

Note that Eq. 2.137 does not differ much from Eq. 2.138, nonetheless the difference is fundamental:

- Z_z is now a function of the frequency ω,
- A factor $-\frac{1}{4} \Delta t^2 \omega^2$ appears.

In practice, the TLM procedure will be as follows: the impedance of the inductive stub, Z_z, is given by Eq. 2.138, except if a negative value is obtained. In this case Eq. 2.138 must be substituted by Eq. 2.137, and the stub is no longer inductive but capacitive.

The procedure is exactly the same for the other components of SCN, and more generally for the other TLM nodes evoked in this dissertation (2D Cartesian nodes, cylindrical node, spherical node).

2.6 Dispersion inherent to the TLM mesh in the modeling of metamaterials

It was shown in section 2.5 that reversing the positions of the capacitive and inductive stubs in the TLM node is equivalent to making the optical constant negative. The basic TLM procedure is not affected by this modification, except for the values of the stubs that must be multiplied by $-\frac{1}{4}\Delta t^2\omega^2$. Admittances and impedances are no longer constant, they are explicit functions of frequency via the quantity ω; this is in agreement with the dispersive nature of metamaterials. The aim of this section is to examine what kind of dispersion the TLM mesh exhibits.

First, consider SCN presented in section 2.3.3. Furthermore, for the sake of simplicity, let the node be a cube, i.e., $\Delta x = \Delta y = \Delta z = \Delta l$. Finally, consider, for instance, the z-component of the capacitive stub that is given by Eq. 2.137. It becomes:

$$Z_z(\omega) = -\frac{1}{4}\Delta t^2\omega^2[\frac{2\mu_z\mu_0\Delta l}{Z_0\Delta t} - 4]. \tag{2.139}$$

The numerical procedure consists of defining a working frequency, ω_0, for which the permeability is the required one, $\mu_z = \mu_z(\omega_0)$. The choice of these two values fixes the impedance of the capacitive stub, $Z_z(\omega_0)$.

On the other hand, Eq. 2.139 yields

$$\mu_z = \frac{2[\Delta t^2\omega^2 - Z_z(\omega)]Z_0}{\Delta l\Delta t\mu_0\omega^2}. \tag{2.140}$$

This means that μ_z is indirectly a function of the frequency. But beyond that, Eq. 2.140 depicts the fact that if we want the permeability to be the same as before ($\mu_z(\omega_0)$) but at a frequency different from ω_0, the stub's impedance can no longer be $Z_z(\omega_0)$. This is in contradiction with the statement that definitely fixes $Z_z(\omega)$ to be $Z_z(\omega_0)$. In this way, we understand that if we excite the mesh with a frequency that differs from ω_0 the mesh will not present the permeability $\mu_z(\omega_0)$. The frequency dependence is emphasized by adding a tild to the expression of the permeability given by Eq. 2.140. Substituting $Z_z(\omega)$ in Eq. 2.140 by its value

given by Eq. 2.139 at $\omega = \omega_0$ yields

$$\begin{aligned}\widetilde{\mu}_z(\omega) &= \frac{2[\Delta t^2\omega^2 - Z_z(\omega_0)]Z_0}{\Delta l \Delta t \mu_0 \omega^2} \\ &= \frac{\Delta l \mu_z(\omega_0)\mu_0\omega_0^2 + 2\Delta t(\omega^2 - \omega_0^2)Z_0}{\Delta l \mu_0 \omega^2} \\ &= \frac{2\Delta t Z_0}{\Delta l \mu_0} - \frac{\omega_0^2}{\omega^2}[\frac{2\Delta t Z_0}{\Delta l \mu_0} - \mu_z(\omega_0)]\end{aligned} \tag{2.141}$$

As it has been mentioned in section 2.3.3, the impedance of the connecting lines, Z_0, and the time-step, Δt, for SCN are very often chosen to be given by Eq. 2.100a and Eq. 2.100b, respectively. In this case, such values yield $\frac{2\Delta t Z_0}{\Delta l \mu_0} = 1$. Finally,

$$\widetilde{\mu}_z(\omega) = 1 - \frac{\omega_0^2}{\omega^2}[1 - \mu_z(\omega_0)]. \tag{2.142}$$

The relation of dispersion given by Eq. 2.142 is obviously reminiscent of the Drude's model, which is very often used when metamaterials are involved. In [44] for instance, FDTD simulations of electromagnetic plane wave in a Drude's model LH material was provided. Nevertheless, such FDTD simulations differ from TLM simulations in one important respect: with TLM, it is the mesh that is dispersive according to Drude's model; while with FDTD, dispersion has to be incorporated into the algorithm. The proof has been carried out for μ_z, but the same results are obtained for the other five components, however $\frac{2\Delta t Z_0}{\Delta l \mu_0} = 1$ has to be substituted by $\frac{2\Delta t Y_0}{\Delta l \varepsilon_0} = 1$ when we are dealing with permittivity. Thus for SCN, we can write that

$$\widetilde{\chi}_i(\omega) = 1 - \frac{\omega_0^2}{\omega^2}[1 - \chi_i(\omega_0)]. \tag{2.143}$$

where χ represents either ε or μ, and where the subscript i is either x, y, or z.

Let us now derive the dispersion relation in the 2D nodes. For instance, we are going to consider the TM-node and assume that $\Delta x = \Delta y = \Delta z = \Delta l$. Thus, Eq. 2.57 becomes

$$Y_x(\omega) = -\frac{1}{4}\Delta t^2\omega^2[\frac{2\varepsilon_x\varepsilon_0\Delta l}{Y_0\Delta t} - 2], \tag{2.144a}$$

$$Y_y(\omega) = -\frac{1}{4}\Delta t^2\omega^2[\frac{2\varepsilon_y\varepsilon_0\Delta l}{Y_0\Delta t} - 2], \tag{2.144b}$$

$$Z_z(\omega) = -\frac{1}{4}\Delta t^2\omega^2[\frac{2\mu_z\mu_0\Delta l}{Z_0\Delta t} - 4]. \tag{2.144c}$$

Similarly to what has been done before, we derive $\widetilde{\varepsilon}_x(\omega)$, $\widetilde{\varepsilon}_y(\omega)$, and $\widetilde{\mu}_z(\omega)$. We get:

$$\widetilde{\varepsilon}_x(\omega) = \frac{\Delta t Y_0}{\Delta l \varepsilon_0} - \frac{\omega_0^2}{\omega^2}[\frac{\Delta t Y_0}{\Delta l \varepsilon_0} - \varepsilon_x(\omega_0)], \tag{2.145a}$$

$$\widetilde{\varepsilon}_y(\omega) = \frac{\Delta t Y_0}{\Delta l \varepsilon_0} - \frac{\omega_0^2}{\omega^2}[\frac{\Delta t Y_0}{\Delta l \varepsilon_0} - \varepsilon_y(\omega_0)], \tag{2.145b}$$

$$\widetilde{\mu}_z(\omega) = \frac{2\Delta t Z_0}{\Delta l \mu_0} - \frac{\omega_0^2}{\omega^2}[\frac{2\Delta t Z_0}{\Delta l \mu_0} - \mu_z(\omega_0)]. \tag{2.145c}$$

The usual values of Z_0 and Δt are given by Eqs. 2.62a and 2.62b, which, together with Eq. 2.145 provide the final expression:

$$\widetilde{\varepsilon}_x(\omega) = 1 - \frac{\omega_0^2}{\omega^2}[1 - \varepsilon_x(\omega_0)], \tag{2.146a}$$

$$\widetilde{\varepsilon}_y(\omega) = 1 - \frac{\omega_0^2}{\omega^2}[1 - \varepsilon_y(\omega_0)], \tag{2.146b}$$

$$\widetilde{\mu}_z(\omega) = 2\{1 - \frac{\omega_0^2}{\omega^2}[1 - \mu_z(\omega_0)]\}. \tag{2.146c}$$

Note the factor 2 for the expression of $\widetilde{\mu}_z$, which is not present for $\widetilde{\varepsilon}_x$ and $\widetilde{\varepsilon}_y$. The dispersion is once again of Drude's model kind in each case. The results would be similar if the TE-node of section 2.3.1 were considered.

After having consider the natural dispersion of Cartesian meshes when metamaterials are involved, we are now concerned with curved meshes, in which we can distinguish the 2D cylindrical (section 2.4.1 and 2.4.2) and the 3D spherical nodes (section 2.4.3).

For the purposes of illustration, we focus first on the cylindrical TM-node presented in section 2.4.2. For metamaterials, Eq. 2.121 becomes

$$Y_r(\omega) = -\frac{1}{4}\Delta t^2\omega^2[\frac{2\varepsilon_r\varepsilon_0}{Y_0\Delta t}\frac{r\Delta\varphi\Delta z}{\Delta r} - 2], \tag{2.147a}$$

$$Y_\varphi(\omega) = -\frac{1}{4}\Delta t^2\omega^2[\frac{2\varepsilon_\varphi\varepsilon_0}{Y_0\Delta t}\frac{\Delta r\Delta z}{r\Delta\varphi} - 2], \tag{2.147b}$$

$$Z_z(\omega) = -\frac{1}{4}\Delta t^2\omega^2[\frac{2\mu_z\mu_0}{Z_0\Delta t}\frac{r\Delta\varphi\Delta r}{\Delta z} - 4]. \tag{2.147c}$$

Note that we cannot chose the size of the node to be the same in the three directions given that the node is naturally bigger near the outer boundary of the mesh. It is important to note that Eq. 2.147 differs from Eq. 2.144 in one important respect: the presence of a spatial coordinate, r, in the expression, which means that these parameters cannot be constant even if the material under consideration is homogeneous. Carrying out the same derivation as before yields

$$\widetilde{\varepsilon}_r(\omega) = \frac{\Delta t \Delta r Y_0}{r\Delta\varphi\Delta z\varepsilon_0} - \frac{\omega_0^2}{\omega^2}[\frac{\Delta t \Delta r Y_0}{r\Delta\varphi\Delta z\varepsilon_0} - \varepsilon_r(\omega_0)], \tag{2.148a}$$

$$\widetilde{\varepsilon}_\varphi(\omega) = \frac{\Delta t \;\; r\Delta\varphi Y_0}{\Delta r\Delta z\varepsilon_0} - \frac{\omega_0^2}{\omega^2}[\frac{\Delta t\, r\Delta\varphi Y_0}{\Delta r\Delta z\varepsilon_0} - \varepsilon_r(\omega_0)], \tag{2.148b}$$

$$\widetilde{\mu}_z(\omega) = \frac{2\Delta t \Delta z Z_0}{r\Delta r\Delta\varphi\mu_0} - \frac{\omega_0^2}{\omega^2}[\frac{2\Delta t\Delta z Z_0}{r\Delta r\Delta\varphi\mu_0} - \mu_z(\omega_0)]. \tag{2.148c}$$

Defining

$$A_r = \frac{\Delta t \Delta r Y_0}{r\Delta\varphi\Delta z\varepsilon_0}, \tag{2.149a}$$

$$A_\varphi = \frac{\Delta t \;\; r\Delta\varphi Y_0}{\Delta r\Delta z\varepsilon_0}, \tag{2.149b}$$

$$A_z = \frac{2\Delta t\Delta z Z_0}{r\Delta r\Delta\varphi\mu_0}, \tag{2.149c}$$

we get

$$\widetilde{\varepsilon}_r(\omega) = A_r - \frac{\omega_0^2}{\omega^2}[A_r - \varepsilon_r(\omega_0)], \tag{2.150a}$$

$$\widetilde{\varepsilon}_\varphi(\omega) = A_\varphi - \frac{\omega_0^2}{\omega^2}[A_\varphi - \varepsilon_\varphi(\omega_0)], \tag{2.150b}$$

$$\widetilde{\mu}_z(\omega) = A_z - \frac{\omega_0^2}{\omega^2}[A_z - \mu_z(\omega_0)]. \tag{2.150c}$$

Here we wish to comment an important point. The TLM timestep, Δt, must be chosen so that no admittances or impedances of the stubs can be negative, it is a requirement that fixes an upper limit on Δt. Once Δt has correctly been fixed, only permittivity or permeability less than unity would be able to make them negative. Thus, if metamaterials are considered, all the impedances or admittances less than unity should be multiplied by $-\frac{1}{4}\Delta t^2\omega^2$, which has the benefit to make them greater than unity anew. When Cartesian nodes are employed, this procedure

is in agreement with the dispersive nature of metamaterials: any optic constant less than unity is associated with an impedance/admittance less than unity, which result in the mesh to be dispersive. However, when cylindrical nodes are used, the situation is more complicated because of the presence of r in the expressions of the impedances/admittances. The sign of an optic constant and its associated impedance/admittance may not coincide, which is not consistent with the fact that metamaterials must disperse. Obviously, this would be of no consequence at the working frequency, ω_0, but may detrimentally alter the validity of any result at other frequency. Consequently, the election of Δt depends on the case under consideration, so are A_r, A_φ, and A_z. There is only one remaining caveat concerning whether Eq. 2.150 is causal or not. In section 4.7.1, a wide discussion about the choice of Δt and causality will be provided, in the particular case of the modeling of invisibility cloaking structures with cylindrical TLM nodes.

The procedure to obtain the dispersion of the cylindrical TE-node is rigorously the same. We start from the expression of the admittance and the impedances,

$$Z_r(\omega) = -\frac{1}{4}\Delta t^2\omega^2[\frac{2\mu_r}{B_r} - 2] \tag{2.151a}$$

$$Z_\varphi(\omega) = -\frac{1}{4}\Delta t^2\omega^2[\frac{2\mu_\varphi}{B_\varphi} - 2] \tag{2.151b}$$

$$Y_z(\omega) = -\frac{1}{4}\Delta t^2\omega^2[\frac{4\varepsilon_z}{B_z} - 2], \tag{2.151c}$$

with

$$B_r = \frac{\Delta t\Delta r Z_0}{r\Delta\varphi\Delta z\mu_0}, \tag{2.152a}$$

$$B_\varphi = \frac{\Delta t \;\; r\Delta\varphi Z_0}{\Delta r\Delta z\mu_0}, \tag{2.152b}$$

$$B_z = \frac{2\Delta t\Delta z Y_0}{r\Delta r\Delta\varphi\varepsilon_0}, \tag{2.152c}$$

which leads to

$$\widetilde{\mu}_r(\omega) = B_r - \frac{\omega_0^2}{\omega^2}[B_r - \mu_r(\omega_0)], \tag{2.153a}$$

$$\widetilde{\mu}_\varphi(\omega) = B_\varphi - \frac{\omega_0^2}{\omega^2}[B_\varphi - \mu_\varphi(\omega_0)], \tag{2.153b}$$

$$\widetilde{\varepsilon}_z(\omega) = B_z - \frac{\omega_0^2}{\omega^2}[B_z - \varepsilon_z(\omega_0)]. \tag{2.153c}$$

Finally, the spherical node is considered. From

$$Y_j = -\frac{1}{4}\Delta t^2\omega^2[\frac{4\varepsilon_j}{C_j} - 4], \tag{2.154a}$$

$$Z_j = -\frac{1}{4}\Delta t^2\omega^2[\frac{4\mu_j}{D_j} - 4], \tag{2.154b}$$

$$j = \{r, \theta, \varphi\}, \tag{2.154c}$$

with

$$C_r = \frac{2\Delta t\Delta r Y_0}{r^2\sin\theta\Delta\theta\Delta\varphi\varepsilon_0}, \tag{2.155a}$$

$$C_\theta = \frac{2\Delta t\Delta\theta Y_0}{\sin\theta\Delta r\Delta\varphi\varepsilon_0}, \tag{2.155b}$$

$$C_\varphi = \frac{2\Delta t\sin\theta\Delta\varphi Y_0}{\Delta r\Delta\theta\varepsilon_0}, \tag{2.155c}$$

$$D_r = \frac{2\Delta t\Delta r Z_0}{r^2\sin\theta\Delta\theta\Delta\varphi\mu_0}, \tag{2.155d}$$

$$D_\theta = \frac{2\Delta t\Delta\theta Z_0}{\sin\theta\Delta r\Delta\varphi\mu_0}, \tag{2.155e}$$

$$D_\varphi = \frac{2\Delta t\sin\theta\Delta\varphi Z_0}{\Delta r\Delta\theta\mu_0}, \tag{2.155f}$$

we get

$$\widetilde{\varepsilon}_j(\omega) = C_j - \frac{\omega_0^2}{\omega^2}[C_j - \varepsilon_j(\omega_0)], \tag{2.156a}$$

$$\widetilde{\mu}_j(\omega) = D_j - \frac{\omega_0^2}{\omega^2}[D_j - \mu_j(\omega_0)], \tag{2.156b}$$

$$j = \{r, \theta, \varphi\}. \tag{2.156c}$$

2.7 Summary

TLM is a time domain numerical method that has been efficiently employed since its introduction in problems involving wave propagation. TLM is based on the analogy between Maxwell's equations and the equations related to the transmission line theory. The mesh is made up of a large number of unitary structures, we refer to as nodes, that are form by intersecting transmission lines. Consequently, the problem of calculating electromagnetic fields propagating in space is substituted by that of calculating voltage and intensity pulses propagating in a transmission line network. The information relative to Maxwell's equations is contained in the scattering matrix that describes how the pulses are scattered at the center of the node.

In this chapter, we put emphasis on several points:

1. A remarkable property of TLM is that it is not only a pure numerical method to solve the field equations, but also the numerical equivalent of a real physical $L-C$ network. Furthermore, TLM is a low-frequency method since the maximum allowed frequency is reduced by the coarseness of the mesh. The spatial discretization length is usually chosen to be smaller than one-tenth of the wavelength.

2. The works following Johns' pioneering paper considered 2D nodes: the parallel node allowed the modeling of a wave that propagates with TE polarization in a medium where only ε and σ^e can vary; while the series node allowed the modeling of a wave that propagates with TM polarization in a medium where only μ and σ^m can vary.

3. SCN was an important contribution to solve 3D problems since it eliminates the disadvantages of other 3D nodes. SCN cannot be described by a unique circuit, but by six coupled shunt and series circuits, as suggested by Maxwell's equations, which are coupled equations.

4. Describing a node by coupling circuits has long been limited to SCN. However, we have shown in this dissertation that the parallel and series nodes should actually be described by coupled circuits too. We introduced the TE- and TM- nodes that are more versatile, both can deal with totally inhomogeneous media including electric and magnetic losses.

5. For the modeling of structures with cylindrical symmetry, one may prefer employing cylindrical nodes that directly assume the shape of the medium's geometry. This kind of nodes are easily obtained from the TE- and TM-nodes by a simple coordinate transformation.

6. In the same manner, the use of spherical nodes, obtained from SCN, may be preferred to solve problems with spherical symmetry.

7. The simulation of metamaterials, i.e., media with $\varepsilon \leq 1$ and $\mu \leq 1$, requires a slight modification of the usual TLM procedure. By simply switching the capacitive and inductive nature of the stubs, metamaterials can be modeled. It is worth noting that this numerical approach is based on the practical technique that consists in obtaining a dual $L-C$ network, which assumes backward wave propagation, from an usual $L-C$ network by interchanging the positions of its capacitors and inductors.

8. Real dual $L-C$ networks behave as a metamaterial that have the particularity to disperse with frequency. Therefore, the TLM mesh for metamaterials, that is, nothing more than the numerical equivalent of the dual $L-C$ network, is dispersive too. We have shown that the distribution of both $\varepsilon(\omega)$ and $\mu(\omega)$ in the TLM mesh strictly follows a Drude-like model for the Cartesian nodes, and a modify Drude-like model for the curved nodes .

Chapter 3

Composite materials

3.1 Introduction

The study of composite materials began more than 150 years ago. Actually, the first traces date from 1837 when Faraday proposed a model of a dielectric which consisted of a series of metallic globules separated from each other by insulating material. Since then, the interest keeps on increasing. Various famous physicians, like Mossotti, Clausius, or Maxwell, have turned their attention to this theoretical problem [45]. Nowadays, the problem is not only of a fundamental order, indeed composite materials are used massively in industry. Their success comes from the possibility to obtain many different properties in function of the different phases constituting the mixture. For reasons of mathematical analogy, all we can say about mixtures hold indifferently for the dielectric constant, magnetic permeability, electric conductivity, heat conductivity, and diffusivity [46]. However, in this study, we will be interested only in the permittivity, disregarding the other constants.

The concept of effective permittivity is practically indispensable in the study of composite materials at low frequency. It permits to describe a medium as homogeneous when a wave gets into its structure. It is worth noting that the size of the inhomogeneities has to be much smaller than the spatial variation of the electric field, i.e., its wavelength, in order to avoid dispersion effects. The effective permittivity depends on many parameters like the individual dielectric constants of the different phases, the volume fraction, the shape of the inclusions, the orientation of the inclusions with respect to the electric field, the localization of the inclusion, etc. Several analytical formulas exist whose ambitions are to derive the effective permittivity of a mixture in terms of the dielectric constant and the

volume fractions of the pure phases [47]. These expressions belong to the mixing rule family and provide a solution more or less exact depending on the individual case.

The complexity of the problem, especially for random mixtures, has caused that only in recent years, when powerful computers at reasonable cost are available, numerical techniques have been applied to this problem. In this chapter, TLM will be used for the modeling of composite mixtures.

- In section 3.2, the most employed theoretical models will be presented. We can distinguish between two kinds of approaches. Predictive formulas, as Maxwell-Garnett or Bruggeman, aim to determine the effective permittivity of a composite material in terms of the available constants of the problem, usually the permittivity and the volume fraction of the individual constitutive phases. Nevertheless, more information are very often required, and it can be more reasonable binding the solution using Wiener and Hashin-Shtrikman's bounds, for example.

- Section 3.3 will be the concern of determining the effective permittivity of composites made up of particles randomly embedded in a dielectric matrix. TLM will be employed and the results will be systematically compared to the models described in section 3.2.

- Section 3.4 will be devoted to the simulation of mixtures with periodic inclusions.

3.2 Theory

3.2.1 Maxwell-Garnett and Bruggeman's model

The study of the electromagnetic behavior and characterization of dielectric mixtures is a classical problem which has already been addressed by Maxwell himself more than a century ago. In 1904, J. C. Maxwell-Garnett (MG) improved Maxwell's work and obtained what we now refer to as MG's relation [48]. The paper due to this scientist deals with glasses containing small metal spheres. He considered the problem of finding the effective permittivity, ε_{eff}, of a medium formed with spheres, of permittivity ε_1, embedded in a host medium of permittivity ε_2. He drastically approximated that the inclusions as a whole are equivalent to a unique dipole that is isolated in the dielectric matrix, as depicted in Figs. 3.1(a)

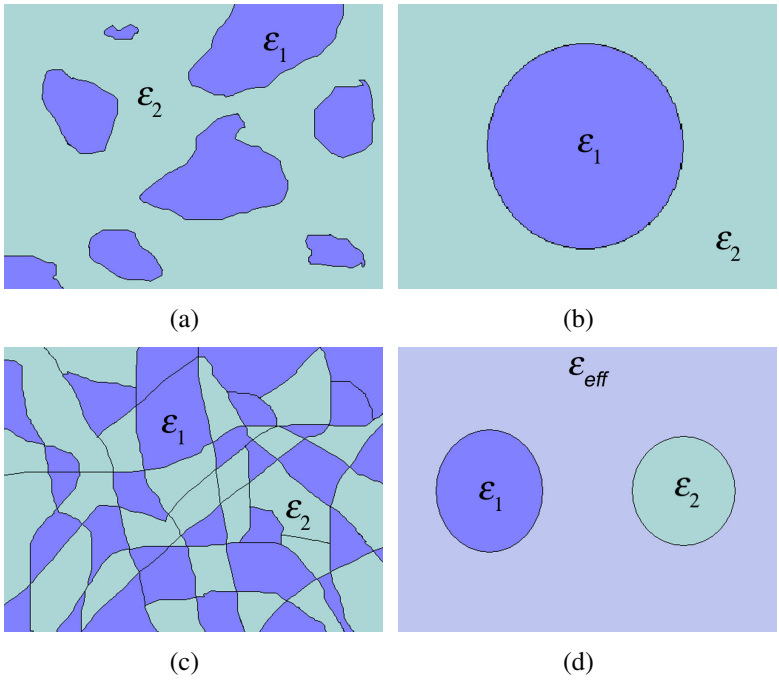

Figure 3.1: **(a,b)** Illustration of MG's model. **(c,d)** Illustration of Bruggeman's model.

and 3.1(b). This theory yields the following expression for ε_{eff} in terms of the dielectric constants ε_1, ε_2 and the volume fractions p_1, p_2 of the pure phases:

$$\frac{\varepsilon_{eff}-\varepsilon_2}{\varepsilon_{eff}+(d-1)\varepsilon_2} = p_1 \frac{\varepsilon_1-\varepsilon_2}{\varepsilon_1+(d-1)\varepsilon_2}. \tag{3.1}$$

The dimensionality d equals 2 if the problem is 2D or equals 3 in the case of considering a 3D media. MG's formula provides satisfactory permittivity values for low concentration of insertions. In particular, it is exact in the limit of very small p_1 but worsens when this concentration increases. Another stumbling block lies in the fact that a nontrivial percolation threshold is not predicted by this model. This means that for all values of p_1 except 0 and 1, $\varepsilon_{eff} \neq 0$ even when $\varepsilon_1 = 0$ or $\varepsilon_2 = 0$.

During the three decades following MG's paper, a lot of contributions were published. Nevertheless they did not bring a significant advance. In 1935, D. A. G. Bruggeman, a Dutch physicist, proposed a new approach [49]. He supposed that every components of the material is immersed in a medium whose permit-

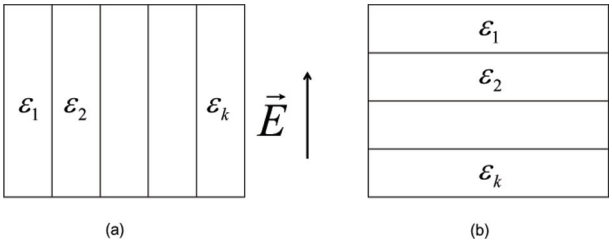

Figure 3.2: Two geometries for which ε_{eff} may be exactly determined.

tivity is equal to that of the mixture, as depicted in Figs. 3.1(c) and 3.1(d). This vision of the problem leads to a model that does take into account the interaction between each component. Moreover, it has the advantage of exhibiting a non trivial percolation threshold and also of being symmetric. By imposing that the field inside a single grain equals the field far from it, we have,

$$p_1 \frac{\varepsilon_1 - \varepsilon_{eff}}{\varepsilon_1 + (d-1)\varepsilon_{eff}} = p_2 \frac{\varepsilon_2 - \varepsilon_{eff}}{\varepsilon_2 + (d-1)\varepsilon_{eff}}. \tag{3.2}$$

Bruggeman's theory is usually considered as a better approximation than MG, particularly for cases where neither p_1 nor p_2 is small. Nevertheless, this affirmation requires qualification since there are situations for which MG is more suitable.

3.2.2 Wiener's bounds

Besides the two simple approximations described in section 3.2.1, many other mixing models exist and can be found in the literature [45]. Furthermore, it is possible to calculate the effective permittivity exactly for composites with very simple internal geometries. That is the case when the composite is made of a series of k parallel slabs of different pure materials. Fig.3.2 shows two of such multiple layer composites:

(a) Plane parallel layers parallel to the electric field.
(b) Plane parallel layers perpendicular to the electric field.

In these two cases a simple calculation provides

$$\varepsilon_{eff} = \sum_{i=1}^{k} p_i \varepsilon_i, \tag{3.3a}$$

$$\frac{1}{\varepsilon_{eff}} = \sum_{i=1}^{k} \frac{p_i}{\varepsilon_i} \tag{3.3b}$$

in the case (a) and (b), respectively. It is worth noting that case (a) actually corresponds to a set of capacitors connected in parallel, while case (b) corresponds to a set of capacitors connected in series. In particular, if we are dealing with a two-component composite material, Eqs. 3.3a and 3.3b becomes

$$\varepsilon_{eff} = p_1\varepsilon_1 + p_2\varepsilon_2, \tag{3.4a}$$

$$\varepsilon_{eff} = (\frac{p_1}{\varepsilon_1} + \frac{p_2}{\varepsilon_2})^{-1}, \tag{3.4b}$$

respectively. Eqs. 3.4a and 3.4b are important values and are known as upper and lower Wiener's bound [50], respectively. Indeed, admitting the difficulty, or even the impossibility, in predicting exact values of effective permittivity, mainly due to the lack of information regarding the actual geometry for a given volume occupation, other studies are devoted to the derivation of theoretical bounds which limit the range of possible values. Wiener's bounds belong to this category.

3.2.3 Hashin-Shtrikman's bounds

As it has been shown in section 3.2.2, the case in which the mixture consists of striations parallel or perpendicular to the current flow leads to Wiener's bounds, Eqs. 3.4a and 3.4b. Thus, considering a pair of two-phase materials in which the two constituents are present in the same proportion but in which the disposition is equivalent to a set of capacitors connected in parallel in one case and a set of capacitors connected in series in the other case, makes a big difference on the effective permittivities. This result brings to the fore that without some detailed geometrical information about the distribution of the two phases, an exact prediction of the effective permittivity is impossible [51]. In this sense, G. P. DeLoor was led to the same conclusion after an extensive experimental study within the framework of his thesis [52]. Therefore, if one wants the effective permittivity to be only defined in terms of the permittivities and the volume fractions of the pure constituents, the better result he can expect will be upper and lower bounds. Wiener's bounds were the first derived and constitute the less restrictive ones.

In 1962, Hashin and Shtrikman (HS) used a variational technique to obtain maximal and minimal bounds for a macroscopically homogeneous and isotropic

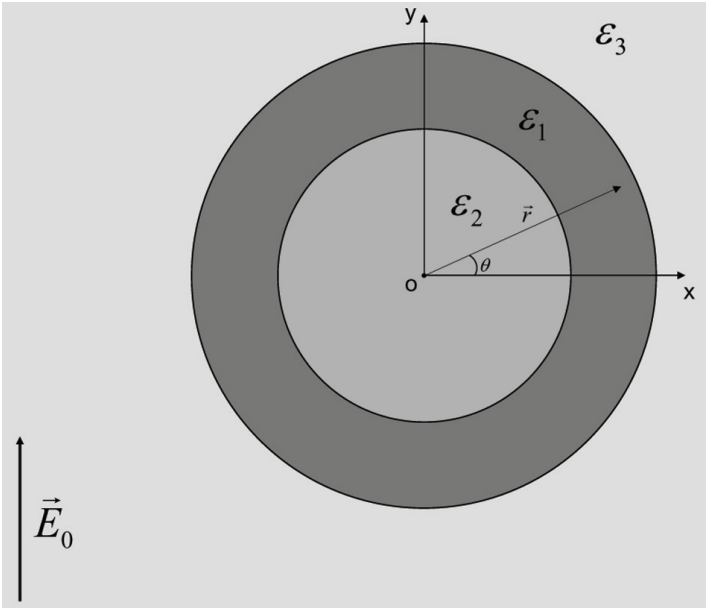

Figure 3.3: Hashin-Shtrikman's coated sphere.

medium [53]. They furthermore showed in the same paper that, in the case of a two-phase material, these bounds are the most restrictive ones that can be obtained in terms of phase volume fractions and permittivities. To improve the HS's bounds, additional information in the statistics of the spatial distribution of the phases is needed. These bounds can be attained by a special microscopic geometry. This occurs when the material is a composite consisting of two concentric spheres, as shown in Fig. 3.3. We assume phase 1 as coating and phase 2 as core. The concentric shell presents a radius a_1, a permittivity ε_1 and occupies a volume fraction p_1. The inner part presents a radius a_2, a permittivity ε_2 and occupies a volume fraction p_2. The volume ratio between the two phases is chosen equal to the volume ratio between the two components of the composite materials.

To prove this result, consider a homogeneous electric field E_0 applied far from the composite sphere. We want to determine the potential V in each one of the three regions. To do so, the Laplace's equation, $\Delta V = 0$, has to be solved. In Fig. 3.3, we can see a 2D representation of the problem. In a spherical coordinate system (r, θ, φ), we know that a general solution for the Laplace equation can be expressed in terms of Legendre's Polynomials, $P_n(\cos\theta)$. Furthermore, for axial symmetric reasons, the solution is not φ-dependent. Thus, the general formula for

the potential is:

$$V(r,\theta) = \sum_{n=0}^{\infty} (\alpha_n r^{-(n+1)} + \beta_n r^n) P_n(\cos\theta). \tag{3.5}$$

However, Eq. 3.5 has to be adapted to each region and then it has to be modified in accordance with the regions to be described:

1. In region 1, forming the concentric shell of the composite sphere, both terms have to be taken into account,

$$V_1(r,\theta) = \sum_{n=0}^{\infty} (A_n r^{-(n+1)} + B_n r^n) P_n(\cos\theta). \tag{3.6}$$

2. In region 2, forming the inner part of the composite sphere, the terms with inverse power of r cannot exist since they produce an infinite potential at the center. Therefore,

$$V_2(r,\theta) = \sum_{n=0}^{\infty} C_n r^n P_n(\cos\theta). \tag{3.7}$$

3. In region 3, i.e., outside the composite sphere, the term $-E_0 r\cos\theta = -E_0 r P_1(\cos\theta)$ has to be added in order to satisfy the condition at $r \to \infty$. Moreover, only the terms with inverse power of r have to be taken into account to avoid divergence at $r \to \infty$,

$$V_3(r,\theta) = -E_0 r P_1(\cos\theta) + \sum_{n=0}^{\infty} D_n r^{-(n+1)} P_n(\cos\theta). \tag{3.8}$$

On the one hand, the potential conservation condition at the interfaces is used, i.e., $V_1 = V_2$ at $r = r_2$ and $V_3 = V_1$ at $r = r_1$. Furthermore, both sides of the equations are multiplied by the polynomial $P_m(\cos\theta)$ and integrated with respect to the variable $\cos\theta$, this process aiming to take advantage of the orthogonal properties of Legendre's polynomials:

$$L_{nm} = \int_{-1}^{+1} P_n(\cos\theta) P_m(\cos\theta) d\cos\theta = \begin{cases} 0 & \text{if } m \neq n, \\ \frac{2}{2m+1} & \text{if } m = n. \end{cases} \tag{3.9}$$

Thus from the above mentioned potential conservation, we obtain

$$A_m r_2^{-(m+1)} + B_m r_2^m = C_m r_2^m, \tag{3.10a}$$

$$A_m r_1^{-(m+1)} + B_m r_1^m = D_m r_1^{-(m+1)} - E_0 r_1 \frac{2m+1}{2} L_{1m}. \tag{3.10b}$$

On the other hand, the normal conservation of the electric induction condition can be used, together with the orthogonal properties of Legendre's polynomial. Concretely, $-\varepsilon_1 \frac{\partial V_1}{\partial r} = -\varepsilon_2 \frac{\partial V_2}{\partial r}$ at $r = r_2$ and $-\varepsilon_1 \frac{\partial V_1}{\partial r} = -\varepsilon_3 \frac{\partial V_3}{\partial r}$ at $r = r_1$, which yields

$$\varepsilon_1[(m+1)A_m r_2^{-(m+2)} - mB_m r_2^{m-1}] = -\varepsilon_2 m C_m r_2^{m-1}, \tag{3.11a}$$

$$\varepsilon_1[(m+1)A_m r_1^{-(m+2)} - mB_m r_1^{m-1}] = \varepsilon_3[(m+1)D_m r_1^{-(m+2)} + E_0 \frac{2m+1}{2} L_{1m}, \tag{3.11b}$$

respectively.

Eqs. 3.10a, 3.10b, 3.11a, and 3.11b form a set of four equations with four unknowns A_m, B_m, C_m, D_m. The resolution of this system proves that the four constants equal invariably 0 if $m \neq 1$. The only nontrivial solution occurs when $m = 1$, which yields

$$A_1 = -\frac{3E_0(\varepsilon_1 - \varepsilon_2)\varepsilon_3 r_1^3 r_2^3}{(2\varepsilon_1 + \varepsilon_2)(\varepsilon_1 + 2\varepsilon_3)r_1^3 - 2(\varepsilon_1 - \varepsilon_2)(\varepsilon_1 - \varepsilon_3)r_2^3}, \tag{3.12a}$$

$$B_1 = -\frac{3E_0(2\varepsilon_1 + \varepsilon_2)\varepsilon_3 r_1^3}{(2\varepsilon_1 + \varepsilon_2)(\varepsilon_1 + 2\varepsilon_3)r_1^3 - 2(\varepsilon_1 - \varepsilon_2)(\varepsilon_1 - \varepsilon_3)r_2^3}, \tag{3.12b}$$

$$C_1 = -\frac{9E_0\varepsilon_1\varepsilon_3 r_1^3}{(2\varepsilon_1 + \varepsilon_2)(\varepsilon_1 + 2\varepsilon_3)r_1^3 - 2(\varepsilon_1 - \varepsilon_2)(\varepsilon_1 - \varepsilon_3)r_2^3}, \tag{3.12c}$$

$$D_1 = \frac{E_0(2\varepsilon_1 + \varepsilon_2)(\varepsilon_1 - \varepsilon_3)r_1^6 - E_0(\varepsilon_1 - \varepsilon_2)(2\varepsilon_1 + \varepsilon_3)r_1^3 r_2^3}{(2\varepsilon_1 + \varepsilon_2)(\varepsilon_1 + 2\varepsilon_3)r_1^3 - 2(\varepsilon_1 - \varepsilon_2)(\varepsilon_1 - \varepsilon_3)r_2^3}. \tag{3.12d}$$

The composite sphere, in which one part has a permittivity ε_1 whilst the other part has a permittivity ε_2, can be viewed as a uniform sphere with permittivity ε_{eff}. So the question is: what is the value ε_3 for which the composite sphere completely merges with the external material? In other words, what is the value ε_3 for which the presence of the composite sphere cannot be detected? In this situation, it is clear that the electric field outside the composite sphere would not be perturbed by its presence. This means that $D_1 = 0$ which, after some calculus, is proven to

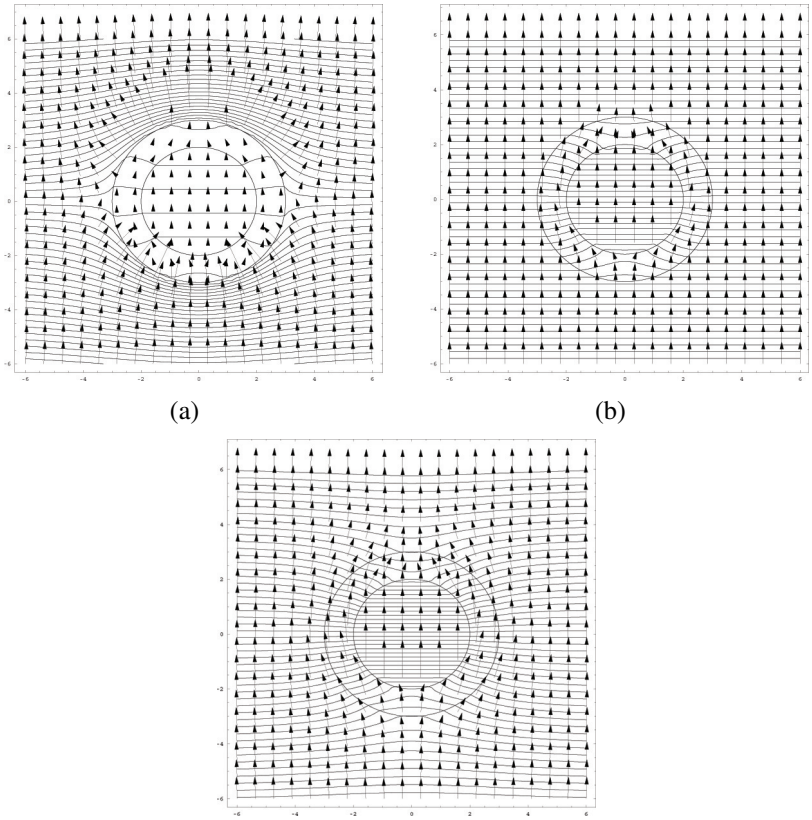

(a) (b)

(c)

Figure 3.4: Equipotential surfaces and electric induction lines (everywhere perpendicular between them) of a coated sphere located in a uniform electric field. $\varepsilon_1 = 18$, $\varepsilon_2 = 2$, $p_1 = 0.704$, $p_2 = 0.296$. Phase 3 permittivity is: $\varepsilon_3 = 1$, $\varepsilon_3 = 50$, and $\varepsilon_3 = \varepsilon_{eff}$, respectively.

be equivalent to

$$\varepsilon_{eff} = \varepsilon_1 + \frac{(\frac{r_2}{r_1})^3}{\frac{1}{\varepsilon_2 - \varepsilon_1} + \frac{1-(\frac{r_2}{r_1})^3}{3\varepsilon_1}}. \tag{3.13}$$

Moreover, we have $p_2 = (r_2/r_1)^3$ and $p_1 = 1 - p_2$ which provides the Hashin-Shtrikman's formula

$$\varepsilon_{eff} = \varepsilon_1 + \frac{p_2}{\frac{1}{\varepsilon_2 - \varepsilon_1} + \frac{p_1}{3\varepsilon_1}}. \tag{3.14}$$

As an illustration, Fig. 3.4 is the electric induction lines and the equipotentials for a coated sphere in which $\varepsilon_1 = 18$, $\varepsilon_2 = 2$, and $p_2 = 0.296$. In Fig. 3.4(a),

the permittivity of the host medium is free space, $\varepsilon_{eff} = 1$; while $\varepsilon_{eff} = 50$ in Fig. 3.4(b). Obviously, the presence of the composite sphere perturbs the external field in both case. According to Eq. 3.14, the effective permittivity of the sphere is given by $\varepsilon_{eff} = 12.01$. If the permittivity of the host medium is chosen to be $\varepsilon_3 = \varepsilon_{eff}$, it is plain from Fig. 3.4(c) that the electric induction lines are no longer perturbed by the presence of the composite sphere.

The maximal and minimal bounds are obtained from Eq. 3.14. The composite material is composed of two phases of permittivity ε_1 and ε_2, let ε_+ and ε_- be the greatest and smallest one, respectively. The values p_+ and p_- represent the volume fraction of the medium whose permittivity is ε_+ and ε_-, respectively. Thus, the upper and lower bounds are given by

$$\varepsilon_{eff,max} = \varepsilon_+ + \frac{p_-}{\frac{1}{\varepsilon_- - \varepsilon_+} + \frac{p_+}{3\varepsilon_+}}, \tag{3.15a}$$

$$\varepsilon_{eff,min} = \varepsilon_- + \frac{p_+}{\frac{1}{\varepsilon_+ - \varepsilon_-} + \frac{p_-}{3\varepsilon_-}}, \tag{3.15b}$$

respectively. To obtain Eq. 3.15b, we have considered the complementary mixture which can be obtained by substituting ε_+ by ε_- and p_+ by p_-. Furthermore, note that the factor 3 appearing in Eqs. 3.15a and 3.15b must be replaced by d when the dimensionality is d.

It is worth noting that the lower limit coincides exactly with the MG's mixing rule, while the upper limit is the dual of MG. By dual, we mean that the inversion in terms of permittivity and concentration must be done by substituting the variables of one phase by the same variable of the other phase as we did to obtain Eq. 3.15b.

3.3 Effective dielectric constant of two-dimensional random composite materials

3.3.1 Pure TLM vs hybrid TLM approach

The effective permittivity of different two-phase dielectric mixtures that consist of different shape insertions with permittivity ε_1 embedded in a host medium of permittivity ε_2 [13] is numerically obtained in the current and the two following sections. A dielectric slab, with its own internal geometry composition, is perpendicularly illuminated by an electromagnetic plane wave and the reflected signal is

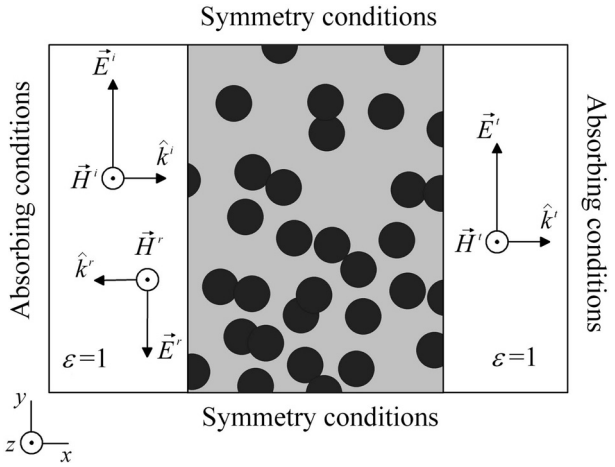

Figure 3.5: Geometry of the problem. In this example, the composite material is made of circular inclusions.

numerically calculated by using the TLM method. Fig. 3.5 illustrates the process. With TLM, a time-domain result is obtained. By using a Fourier transform, we can translate it to the frequency domain which allows to determine the reflection and transmission coefficients for each frequency steps $\Delta f = f_{max}/N_{sample}$. The reflection and transmission coefficients are a list of complex numbers corresponding to the frequencies $f = n\Delta f$, with $n = 0,1,2,\ldots,N_{samples}-1$. Although the TLM results are valid for wavelengths below the dispersion limit, $\Delta l < 0.1\lambda_{min}$, most of the results presented in this work are concerned with the first frequency point, corresponding to a quasi-static solution. Thus, the numerical reflection (or equivalently transmission) coefficient is compared to the theoretical reflection coefficient of a planar dielectric slab of permittivity ε_{eff}, thus the effective value is easily obtained. For the sake of completion, we give here the reflection, R, and transmission, T, coefficients for a slab–with permittivity ε, permeability μ, electric conductivity σ, and thickness e–that is embedded in free space and illuminated by a wave whose angular frequency is ω:

$$R(\varepsilon,\mu,\sigma,e,\omega) = \frac{j\tan ke(\eta^2-\eta_0^2)}{-2\eta\eta_0 + j\tan ke(\eta^2+\eta_0^2)}, \tag{3.16a}$$

$$T(\varepsilon,\mu,\sigma,e,\omega) = \frac{2}{2\cos ke - j(\frac{\eta}{\eta_0}+\frac{\eta_0}{\eta})\sin ke}, \tag{3.16b}$$

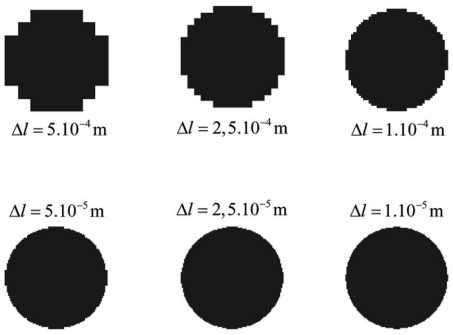

Figure 3.6: Cartesian nodes used to approximate a curved geometry.

where η_0 and η are the impedances of free space and the slab, respectively, while k is the wavenumber.

The insertions considered afterwards are circles, squares, and ellipses (with different eccentricities). In this chapter, the Cartesian nodes presented in chapter 2.3 will be employed. To describe the circular shapes, the mesh has therefore to be thin enough, which means that Δl has to be much smaller than the typical size of the insertions. Indeed, the greater the number of nodes composing the insertion, the greater the precision with which the shape can be described, as it is shown in Fig. 3.6. However, increasing the numbers of nodes produces high memory requirements and also a reduction in the maximum allowable time step. These memory and time computing limitations prevent from modeling the insertions with all the precision we would like.

Karkkainen *et al.*, in a bunch of three papers [54–56], proposed a way to partially avoid this problem of memory and time limitation. In these works, Δl does not have to be that small. The geometry details are taken into account by subdividing the main node into N parts along each direction, thus generating secondary cells of side $\Delta l/N$. This subdivision allows defining two dual circuits of series connected capacitors or parallel connected capacitors, which provide lower and upper bounds for the ε_{eff} of the nodes. The situation is depicted in Fig. 3.7 for $N = 2$. Finally, the effective permittivity of this main node is supposed to be the average of these bounds. Of course, this approximation gets better as N increases. The idea is combining the advantages of using large values of Δl for the main node, i.e., less memory and time computing requirements, but simultaneously describing the geometry with a finer detail. For this reason, we refer to this technique as hybrid TLM method even though the original work was initially implemented

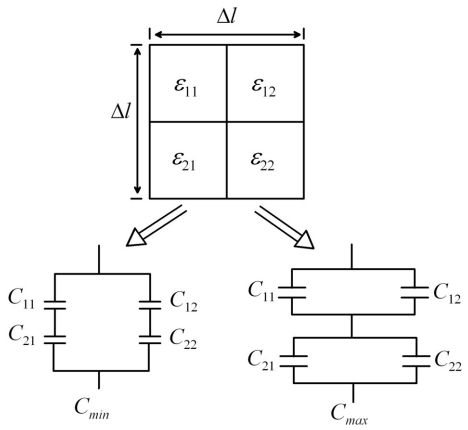

Figure 3.7: Subgriding approach used to determine ε_{eff}.

with the FDTD method. As already noted by Karkkainen, the approach is expected to behave properly when interfaces between different materials are vertical or horizontal. However, arbitrary oriented surfaces, such as those presented by spheres, are only approximately described. For this reason, the treatment consisting in directly model the inclusions without approximation (pure TLM method) will not be abandoned and systematically compared with the hybrid method.

3.3.2 Random circular inclusions

In this section, 2D circular insertions are randomly inserted in a host medium. We have used the technique of Minimal Standard Generator to obtain random numbers, these numbers being then used as the coordinates of the inclusion centers. This technique, proposed by Park and Miller [57], has the advantage of being suitably tested and easy to implement. Overlapping between insertions is allowed, which complicates even more the initial spherical geometry with possible clusters. The slab width, in the x-direction, is 20 mm and is periodic along the y-direction. Two regions, made of vacuum and whose width is 20 mm, surround the slab on each side. Absorbing boundary conditions at both limits of the x-axis are imposed, by connecting the transmission lines reaching these limits to a lumped load with the vacuum impedance. This impedance matching condition is a remarkably simple boundary condition in the TLM method and provides accurate results for normally incident waves. The inclusions in the slab cause inhomogeneities and thus avoid this normal incidence to be met at points near this material. However,

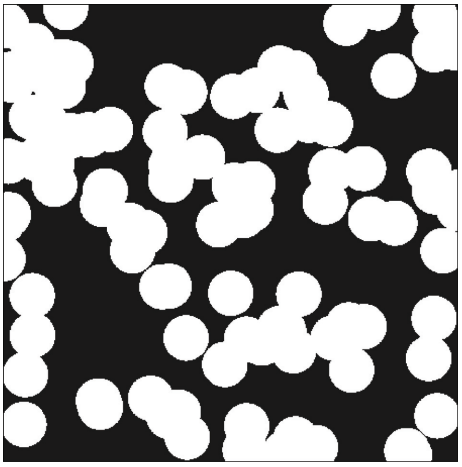

Figure 3.8: 100 circular inclusions randomly distributed.

boundaries along the x-direction are chosen far enough so that it is reasonable to consider that the nonphysical reflections are absorbed.

The first modeled material corresponds to 100 circular inclusions having a higher permittivity than that of the environment region. The radius of the circular inclusions is 1 mm and $\Delta l = 0.1$ mm. We choose $\varepsilon_1 = 18$ and $\varepsilon_2 = 2$ for the subsequent applications. Fig. 3.8 is an illustration of the typical geometry for which ε_{eff} has to be determined. Intuitively, a modification in the location of the inclusions will have repercussions on ε_{eff}. To underline this, we fix the volume fraction of the inclusions to $p_1 = 0.5$, we generate different geometries and, for each one, we determine the corresponding ε_{eff}. In practice, this is done by changing the seed of the random numbers generator so that a unique seed value describes entirely a given mixture configuration. A total of 1000 random distributions is modeled and the results are given in the histogram form showed in Fig. 3.9(a). Obviously, the shape of the distribution is reminiscent of a Gaussian distribution with a mean value of 5.438 and a standard deviation of 0.219.

Fig. 3.9(b) depicts the result if hybrid TLM nodes are employed. The obtained Gaussian distribution has identical standard deviation, but the mean value is 5.715. It is interesting to notice that the hybrid method gives an account of the different configurations of the composite in the same proportion as for the pure method even if a gap, of the order of 5% in this case, between the two values exists.

One can wonder what happens if the radius of the inclusions is increased. To

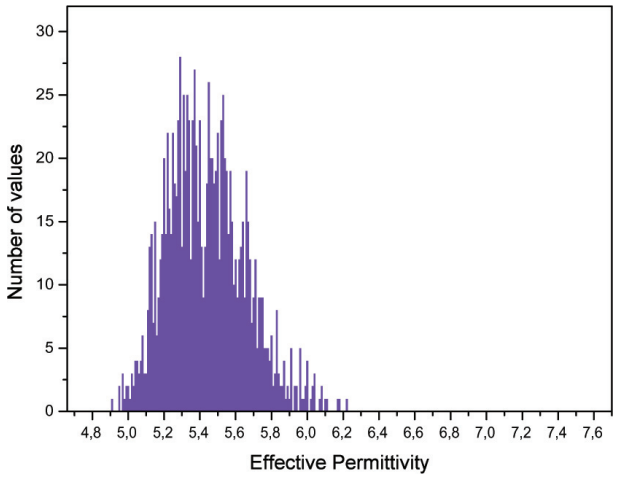

(a)

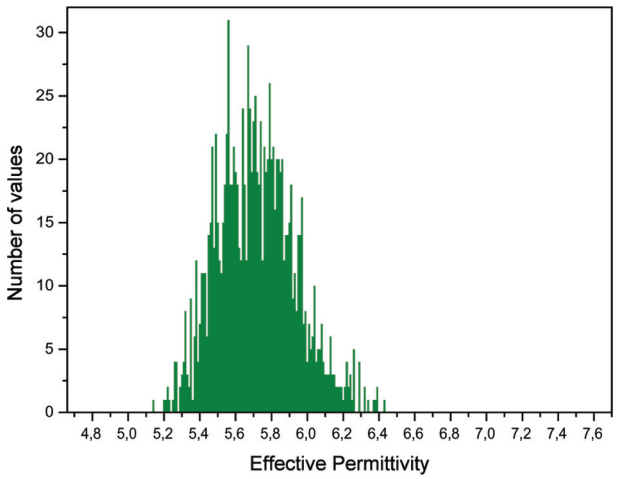

(b)

Figure 3.9: Histogram of the effective permittivity of circular inclusions randomly distributed derived with **(a)** the pure TLM method and **(b)** the hybrid TLM method. The radius of the inclusions is 1 mm. Range limits of ε_{eff} correspond to HS's bounds.

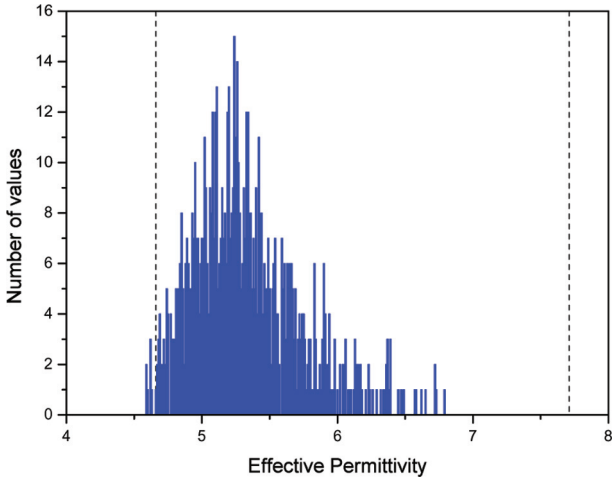

Figure 3.10: Histogram of the effective permittivity of circular inclusions randomly distributed derived with the pure TLM method. The radius of the inclusions is 2 mm. HS's bounds are represented with dashed lines.

answer this question, the preceding study (with 775 samples) is repeated using a radius of 2 mm instead of 1 mm and maintaining $p_1 = 0.5$ with 24 circular inclusions. The result is shown in Fig. 3.10. The Gaussian distribution is again observed, the mean value is 5.321, while the standard deviation is 0.402. The Gaussian shape is slightly distorted, but the most remarkable fact is that the distribution is wider. HS's bounds have even been surpassed in a non-negligible number of geometries, which constitutes a serious limitation to the validity of HS's bounds. We explain this result by the possibility for the inclusions to overlap between one another. Bigger inclusions yield therefore less predictive results. For small inclusions, a higher number of insertions is required to reach a certain concentration. Therefore, if the position of a given particle is randomly modified, the fact that there is still a high number of small insertions to be located means that it is relatively likely that another particle occupies the available area. Smaller insertions cause the different geometries to be more similar and, thus, the effective permittivity of the mixture is more concentrated around its mean value. It is worth noting that this effect of concentration is of high interest in the design and practical manufacturing of composite dielectrics, since the natural uncertainty due to differences in the internal structure is minimized.

Furthermore, it is interesting to visualize which kind of changes in the internal geometry makes such a big difference in ε_{eff}. In Fig. 3.11, the mixture samples

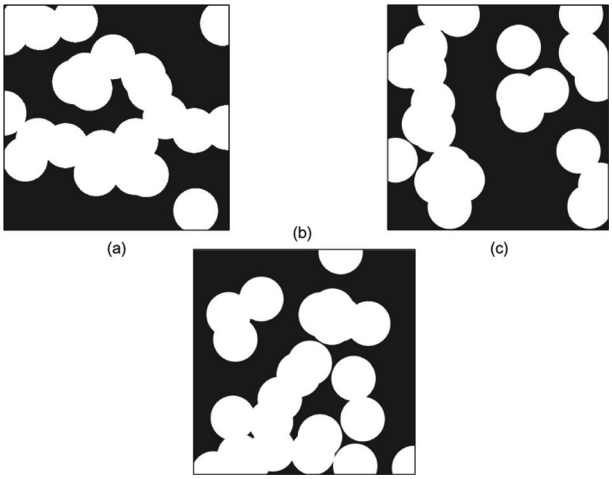

Figure 3.11: Composites that offered: **(a)** minimum ε_{eff}, **(b)** average ε_{eff}, **(c)** maximum ε_{eff}, respectively. White and black colors correspond to $\varepsilon_1 = 18$ and $\varepsilon_2 = 2$, respectively. The radius of the inclusions is 2 mm.

that offered the minimum, the mean value, and the maximum effective permittivity are shown. It underlines that **(a)** is reminiscent of parallel plates perpendicular to the electric field, while **(c)** is reminiscent of parallel plates parallel to the electric field; both tend therefore to the Wiener's geometries in Fig. 3.2.

In the preceding examples, we have arbitrarily chosen $\Delta l = 0.1$ mm, assuming that 100 nodes would be sufficient to properly model a unitary inclusion. To determinate the accuracy of this choice, a convergence test is now performed. In the case in which the radius of the sphere is 1 mm, we pick three particular geometries that provide ε_{eff} close to the mean (seed=35783), maximum (seed=35831), and minimum (seed=32998) values for this concentration. The test begins with a reference size of $\Delta l_{ref} = 1mm$. A finer detail is achieved in the pure TLM solution by considering smaller main nodes of length $\Delta l = \Delta l_{ref}/N$. By increasing the subdivision parameter, N, we improve the precision, and thus the accuracy of the ε_{eff} value, at the expense of higher memory requirements in the numerical modeling of the propagation of the signal in the TLM mesh. Regarding the hybrid TLM method, the parameter N is only an auxiliary subdivision parameter that splits Δl_{ref} into N parts along each direction. This leads to a set of two dual circuits like those presented in Fig. 3.7, corresponding to the upper and lower bounds for the permittivity of the node. Nevertheless, it is worth noting that, for any value

Table 3.1: Convergence

Pure TLM method ($\Delta l = 1/N$ **mm**)				
	$N = 10$	$N = 20$	$N = 40$	$N = 80$
Low ε_{eff} distribution	4.915	4.881	4.865	4.860
Medium ε_{eff} distribution	5.289	5.257	5.247	5.243
High ε_{eff} distribution	6.220	6.152	6.143	6.138
Hybrid TLM method ($\Delta l = 1$ **mm**)				
Low ε_{eff} distribution	5.134	5.133	5.145	5.147
Medium ε_{eff} distribution	5.524	5.509	5.506	5.504
High ε_{eff} distribution	6.416	6.425	6.428	6.429

of N, the mesh size and the time step are conserved, $\Delta l = \Delta l_{ref}$ and $\Delta t = \frac{\Delta l_{ref}}{2c}$, respectively. So, by increasing N, the only generated requirement concerns the construction of the internal geometry within the planar sheet, i.e., the determination of the permittivity of a given TLM node, but leaves the TLM requirements unaltered. The table shows the effective permittivity obtained for different values of N in both cases. It can be seen that the results obtained with the hybrid technique and the pure TLM technique have the same behavior as regards the convergence process. Both require the same value of N, around 40 or 80, to reach an acceptable result. For the hybrid method, the numerical requirement is not significantly increased because the mesh size is always maintained to 1 mm, while higher values of N for the pure TLM method produce a considerable increase in memory storage and time computing requirements.

We consider again the problem consisting in modeling a mixture composed of circular inclusions having a higher permittivity than that of the environment. The difference is that ε_{eff} is obtained in the whole range of p_1 with $\varepsilon_1 = 18$ and $\varepsilon_2 = 2$. Both pure and hybrid methods are used and the radius of the inclusions is still 1 mm. We realize different values of p_1 by locating more or less particles in the slab. In order to avoid obtaining a geometry that is nothing more than the mere carbon-copy of the previous one, but with a sphere added or taken away, a different seed value is attributed to each configuration. Results for the pure TLM method using $N = 20$ and the hybrid method with $N = 80$ are shown in Figs. 3.12(a) 3.12(b), respectively. Results are qualitatively similar, they are located within the Wiener and HS's bounds, but a sensible difference is observed between the pure and the hybrid TLM results. Concerning the predictive formulas, Bruggeman's approach is more accurate than MG (equivalent to the lower HS's bound) model; in any case, predictions become poorer as the volume fraction increases, the most affected model being MG as expected. The mixing approach presented in [58] collects dielectric mixing rules into one family according to

$$\frac{\varepsilon_{eff} - \varepsilon_2}{\varepsilon_{eff} + \varepsilon_2 + \nu(\varepsilon_{eff} - \varepsilon_2)} = p_1 \frac{\varepsilon_1 - \varepsilon_2}{\varepsilon_1 + \varepsilon_2 + \nu(\varepsilon_{eff} - \varepsilon_2)} \tag{3.17}$$

where ν is a dimensionless parameter. The value $\nu = 0$ gives the MG's rules, whilst $\nu = 1$ gives the Bruggeman's approach, note that some other values of ν give other known prediction formulas not mentioned in this work. It is of interest to determine which value of ν fits the obtained distribution. For the pure method, $\nu = 0.51$ turns out to be the most suitable value, while $\nu = 0.63$ is found for the hybrid method. In Figs. 3.12(a) and 3.12(b), the corresponding curves are plotted.

Let us now consider the inverted mixture, i.e. with $\varepsilon_1 = 2$ and $\varepsilon_2 = 18$, made of circular inclusions having a lower permittivity than that of the environment. The result is depicted in Figs. 3.13(a) and 3.13(b). It turns out that $\nu = 0.86$ is the most suitable value for the modeling carried out with the pure method, while $\nu = 0.91$ is found for the hybrid method. It is interesting to note that in this case the difference between the pure and hybrid methods is less significant. Furthermore, the inverted mixture seems to present an effective permittivity, in terms of the volume fraction, close to the Bruggeman's distribution.

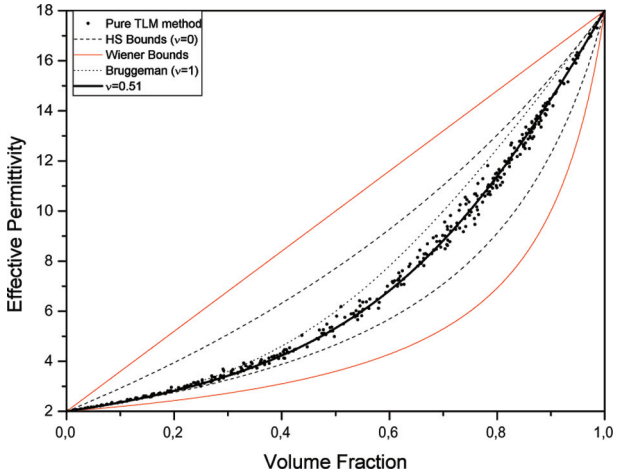

(a)

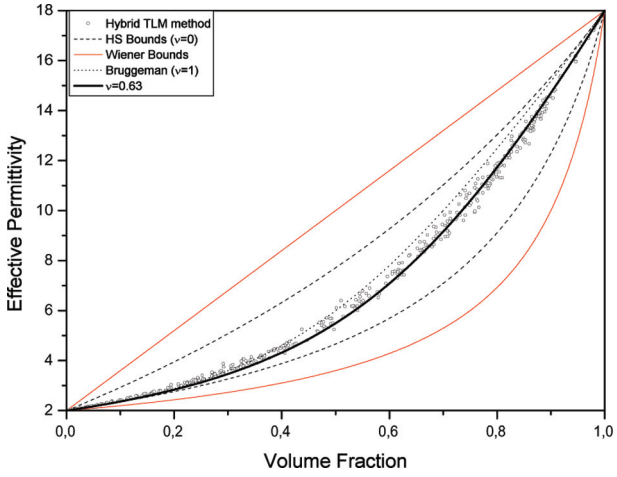

(b)

Figure 3.12: Results for $\varepsilon_1 = 18$ and $\varepsilon_2 = 2$. Simulation is carried out with the **(a)** pure and **(b)** hybrid TLM method.

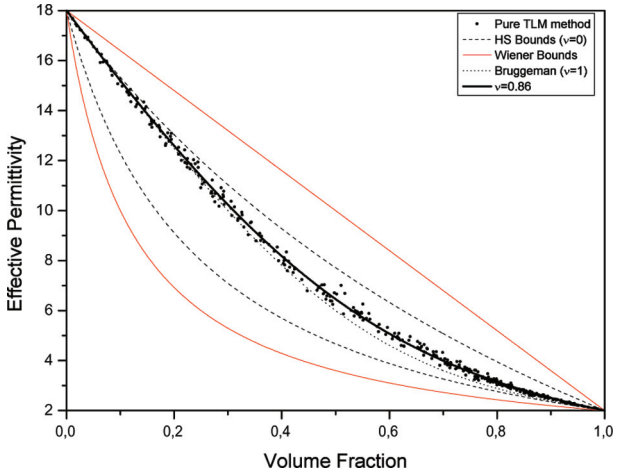

(a)

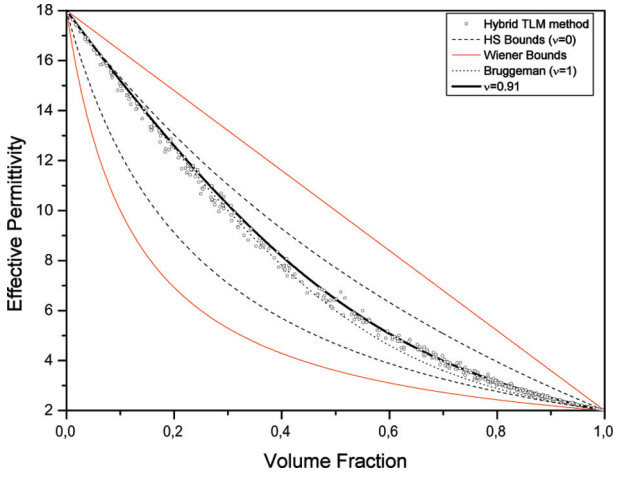

(b)

Figure 3.13: Results for $\varepsilon_1 = 2$ and $\varepsilon_2 = 18$. Simulation is carried out with the **(a)** pure and **(b)** hybrid TLM method.

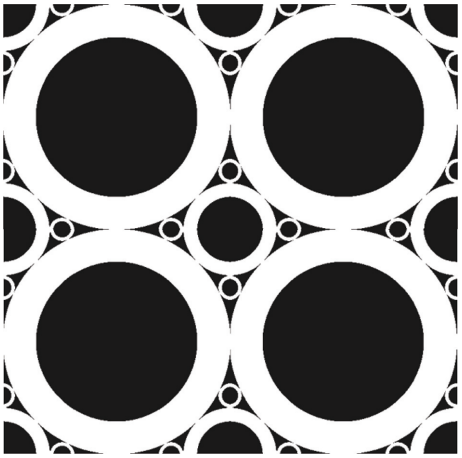

Figure 3.14: Periodic structure with effective permittivity equal to HS's bound.

3.3.3 About the Hashin-Shtrikman's bounds

Differences between numerical pure and hybrid TLM results are not due to a problem of convergence. Therefore a remaining worry is to determine which of these numerical results is most accurate. The pure solution should intuitively provide the best results since details are considered directly, without averaging approaches. However, an appropriate numerical test is required to validate this intuition. We have previously verified that the effective permittivity of mixtures always falls in the range predicted by the Wiener's bounds. Even if HS's bounds have been shown to fail in some situations, see Fig. 3.10, they considerably improved Wiener's bounds. They have been claimed to be the most restrictive ones if only the host and insertion permittivities, as well as the concentration are known [53]; in other words, most restrictive bounds would require additional information, such as the size and the specific spatial distribution of the insertions. In section 3.2.3, it has been shown that HS's bounds can actually be attained by a specific geometry: a material in which spheres of one phase are coated by a spherical shell of the other phase. In practice, once the coated spheres have been arranged in such a way that they occupy a maximum of the available volume, identical but smaller structures must be located in the remaining free space. This periodic assemblage is infinitely repeated with many coated spheres until the whole space is filled. This process is actually impossible since we cannot fill the entire slab with circles. However, we can approach the ideal configuration, as suggested in Fig. 3.14, with three levels of insertions. Let us assume phase 1 as core and phase 2

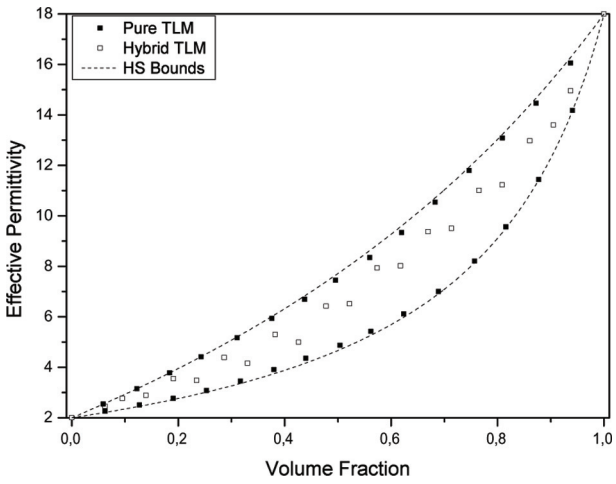

Figure 3.15: Distributions providing HS's bounds for pure TLM and hybrid TLM solution. The lower branches model $\varepsilon_1 = 18$ and $\varepsilon_2 = 2$, while upper branches correspond to the dual mixture.

as coating. The effective permittivity is a function of the volume fraction p_+ of the phase presenting the highest permittivity. It is then worth noting that the case $\varepsilon_1 > \varepsilon_2$ represents the lower HS's bound, while the dual case, $\varepsilon_2 > \varepsilon_1$, yields the upper HS's bounds.

Our test will consist in simulating the geometry of Fig. 3.14 with both TLM approaches and represent the effective permittivity in terms of p_+. Pure and hybrid TLM results for $\varepsilon_1 > \varepsilon_2$ and $\varepsilon_2 > \varepsilon_1$ are shown in Fig. 3.15 with solid and hollow circles, respectively. The lower branch in each TLM model corresponds to $\varepsilon_1 = 18$ and $\varepsilon_2 = 2$, while the upper one corresponds to a dual situation with inverted permittivities. As expected, pure TLM results are in close agreement with the theoretical HS's bounds, while the hybrid TLM approach is unable to accurately reproduce the behavior of this challenging geometry. As a consequence of this result, the following mixtures will only be modeled with the pure TLM method in the next section.

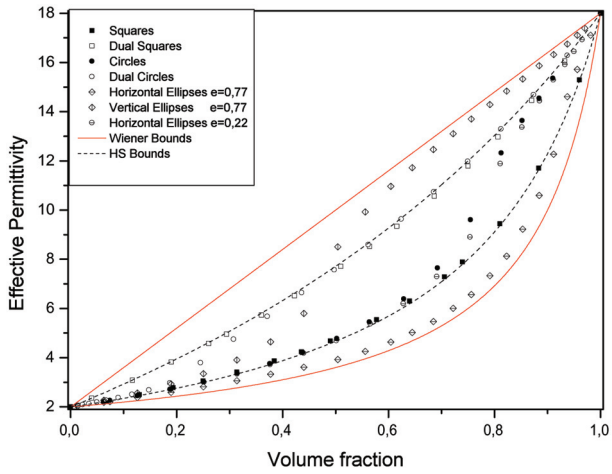

Figure 3.16: Effective permittivity versus concentration for an homogeneous distribution of 2D inclusions of different shape.

3.4 Effect of the shape of the inclusions on the effective dielectric constant of periodic composites

In this section, we consider several types of inclusions with different shapes. The geometries of the studied inclusions are: circles, squares, and ellipses with different eccentricities. For the sake of simplicity, the inclusions, whose relative permittivity is again $\varepsilon_1 = 18$, are now periodically placed in a host medium whose permittivity is $\varepsilon_2 = 2$. The section of the inclusions is variable which permits the study of ε_{eff} in terms of the volume fraction. The results are depicted in Fig. 3.16. Wiener and HS's bounds are also included. Let us also remember that the lower HS's bound corresponds to MG's prediction formula. As we could expect, for low concentrations and irrespective of the type of inclusions, results are in good agreement with MG, i.e., the lower HS's bound, while a deviation is observed as the concentration increases due to interaction between neighbor insertions. This deviation depends on the shape of the inclusions. The ellipses with high eccentricity, $e = 0.77$, overlap between each other from the concentration $p_1 = 0.504$. As a result, the configuration tends to be similar to the vertical or horizontal planar capacitor of Fig. 3.2. This explains the sudden variation of ε_{eff} in this case for both orientations. For instance, ε_{eff} significantly increases for vertical ellipses around $p_1 = 0.5$. This abrupt variation on ε_{eff} is in agreement with the overlapping value, $p_1 = 0.504$. From this limit, the dielectric mixture looks like the

vertical distribution corresponding to the upper Wiener's limit. The same kind of comment can be made for the horizontal ellipses, substituting the upper Wiener's bound by the lower one. This variation in the overlapping region is also observed for horizontal ellipses with a small eccentricity of 0.22. Furthermore, it is interesting to notice that this low eccentricity permits all the same to dissociate the corresponding effective permittivity from the perfect circle one, this dissociation being clearer as the concentration increases. Of course it is anyway possible to explain the divergence between a sphere and an ellipse (even for low eccentricity) towards high or low ε_{eff}, underlining that the configuration begins to converge towards the Wiener's bounds.

The distribution of ε_{eff} in terms of the concentration for the square inclusions is striking. It follows the lower HS's bounds, i.e., the MG's distribution for the all range. This observation has already been mentioned in other works, and since MG is supposed to be accurate only for low concentration, it has been qualified of surprising [59, 60]. In fact, one might claim that this result is not that surprising if such a distribution is related to the HS's bounds. As mentioned in section 3.3.3, Fig. 3.14 represents a geometry that is capable of providing the lower or upper HS's bounds, depending on the composition of the concentric circles. If the permittivity of the core is greater than that of the coating, ε_{eff} corresponds to the lower HS's bound and vice-versa. This is rigourously true only in the case of an infinite number of composite circles capable of totally filling the whole space, rendering the realization of such a geometry unpracticable. On the other hand, square inclusions periodically embedded in a dielectric medium may be viewed as coated squares put next to one another, which is a geometry reminiscent of Fig. 3.14, provided that the circular inclusions are substituted by square inclusions. Moreover, the latter inclusions can fill the whole space with no need of adding new levels of smaller squares. Therefore, it appears natural that periodic square particles be described by one of the HS's bound, and thus by MG's formula, irrespective of the volume fraction. For the sake of completion, ε_{eff} for the dual mixture, in which square insertions with $\varepsilon_1 = 2$ are homogeneously distributed in a host medium whose permittivity is $\varepsilon_2 = 18$, is also plotted in Fig. 3.16. As expected, it follows the upper HS's bound.

Results for 3D mixtures are shown in Fig. 3.17. The node size is $\Delta l = 0.1$ mm and the inclusions are: sphere, cube, and ellipsoid. For the ellipsoids, the semi-axis along the y- and z-directions have the same length. Every insertions are uniformly distributed, so symmetry conditions are imposed to model only one

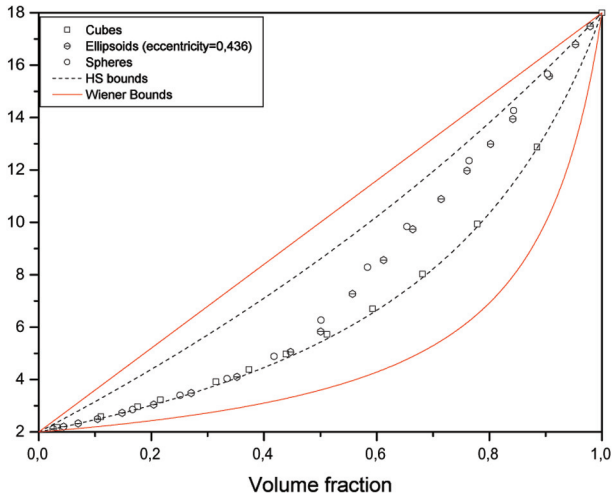

Figure 3.17: Effective permittivity obtained with the pure TLM model versus concentration for an homogeneous distribution of 3D inclusions with different shape.

fourth of each insertion and thus reducing memory and time calculation requirements. Results are qualitatively similar to those presented in 2D situations, but now overlapping happens at lower concentration values and deviations from the HS's limits are observed earlier.

3.5 Summary

In this chapter, we have been concerned with the numerical calculation of the quasi-static permittivity of 2-phase composite materials that exhibit various types of internal microgeometries.

1. Two TLM numerical approaches have been considered. First, a hybrid TLM technique which, by means of an auxiliary subgriding technique leading to a pair of dual capacitor circuits, allows the use of a mesh size comparable to the inclusion dimensions. Second, a pure TLM approach has also been considered in which a finer detail is achieved by using a mesh size smaller than the typical dimension of the insertions. We have shown that the hybrid method, even if it allows to save computational requirements, cannot provide accurate results for some geometries.

2. Circular dielectric inclusions randomly embedded in a homogeneous medium were considered. Hundreds of TLM simulations were carried out in order to get a statistical behavior of such mixtures.

    - This treatment has pointed out that no prediction theory is able to offer a specific value of effective permittivity for random media. Indeed, all values belonging to the range defined by Wiener's bounds are possible, but the task consisting in finding what is the exact value is inaccessible with analytical methods. Therefore, numerical methods must be used if an exact value is required.
    - If the concentration is constant, the possible effective permittivities obtained for different internal distribution of insertions follows a distribution of Gaussian nature with a mean value and a standard deviation.
    - HS's bounds were claimed to be the most restrictive bounds that it is possible to obtain in terms of the permittivities and volume fraction of the pure phases. Nevertheless, this has to be put in doubt given that HS's bounds have been surpassed in a non-negligible number of geometries because of the overlapping between the insertions.
    - It seems that the smaller the size of the inclusions the smaller the standard deviation of the distribution. In other words, the effective permittivity of a composite material made of small randomly distributed insertions, is close to the mean value. Thus, if one knows the volume fraction of small inclusions, he will be able to predict with good precision the effective permittivity of the mixture, whatever the arrangement of the inclusions. This conclusion is of high interest in the design and practical manufacturing of composite dielectrics.
    - If the full range of volume fraction is considered, we have observed that the prediction theories are well suited for low concentrations, but neither Bruggeman nor MG are able to describe with precision the behavior when the concentration increases. However, Bruggeman appears to be closer to the numerical results, above all in the case of inclusions with permittivity smaller than that of the host medium.

3. Secondly, the effect of the shape of the inclusions on ε_{eff} was studied. Therefore, composites containing different types of periodical inclusions have been investigated.

- As long as the concentration is not too elevated, the mixtures are described with good accuracy by MG's formula, irrespective of the kind of inclusions under consideration.
- When the concentration increases, ε_{eff} tends to diverge from MG's formula, the degree of divergence depends on the shape of the inclusions.
- Once the overlapping limit is exceeded, ε_{eff} exhibits a drastic change and tends towards the Wiener's bounds. This can been explained by the similarity between parallel plate distributions and overlapped geometries.
- The square inclusions can be clearly distinguished from the other shapes since they present the particularity to match MG's formula regardless of the volume fraction.

Chapter 4

Cloaking structures

4.1 Introduction

The invisibility cloak has been proposed by Pendry *et al.* [61]. Basically, the idea is to create a hole in which any electromagnetic radiation is excluded. For this purpose, the electromagnetic radiation must be steered around the cloaked region, which seems to face Fermat's principle stipulating that any electromagnetic wave starting out traveling along a certain direction is constrained to stay on that line. Nonetheless, we might imagine another space related to the starting space by a mathematical transformation. Let us consider a warped lattice that creates a concealment volume, as depicted in Fig. 4.1. As a result, any electromagnetic wave propagating in this distorted lattice is naturally swept around the void region. The point is to determine what happens to Maxwell's equations when the coordinate transformation is done. It turns out that the equations have exactly the same form [62], but the dielectric and the magnetic constants are scaled by

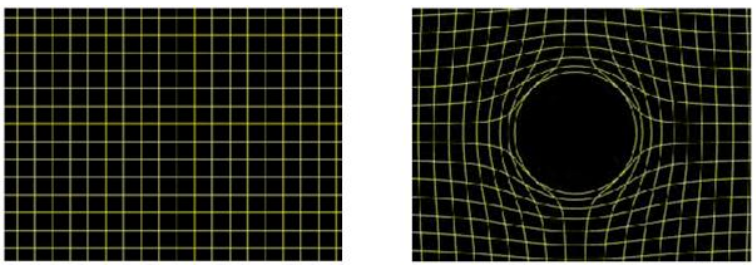

Figure 4.1: From the original space to the distorted space.

a certain factor. Therefore, transforming the material properties is equivalent to distorting the original space. This means that the space outside the concealment volume might be replaced by a new material: the cloak. It is worth noting that the obtained cloaking parameters, irrespectively of their complicatedness, are fully consistent with the physics laws.

- Section 4.2 will be concerned with the coordinate transformations that lead to the constitutive parameters of the cloak.
- Section 4.3 will be dedicated to a short review of the research done in the framework of the cloaking topic.
- In section 4.4, we will focus on the importance of numerical simulations to study cloaking structures.
- In section 4.5, the first modeling of a cloak with TLM will be presented. It will be shown in particular that approximating the material constituting the cloak by an effective medium allows removing the anisotropic nature of the invisible shell.
- Section 4.6 will illustrate that using the curved TLM nodes presented in section 2.4 yields very accurate results. Furthermore, it will be proven that TLM allows assuming strictly infinite values for the permittivity and permeability. This capability of TLM is of importance because the accuracy of the modeling is enhanced and opens the way to the study of challenging problems.
- In section 4.7, the dispersiveness of a 2D cloak will be emphasized and taken into account to study the frequency shift and the time delay that affect an electromagnetic plane wave propagating through a cloaking shell. Furthermore, we will demonstrate in section 4.7.1 that the fact that the cloak is a metamaterial fixes some of the TLM parameters if cylindrical nodes are employed.
- Section 4.8 will be related to the anticloak concept. The anticloak is a material that has been recently shown capable of defeating the cloaking effect. However, we numerically show that the presence of a layer with extreme constitutive parameters actually renders the anticloak unable to produce its effect. Moreover, we will propose a simple theoretical model that leads to the same conclusion if the cloak is slightly dissipative.

4.2 Coordinate transformations

At this point, the difficulty is to obtain the needed permittivity and permeability to make a cloak. We choose the hidden object to be a sphere of radius R_1 and the cloaking region to be contained within the annulus $R_1 < r < R_2$. Therefore, we have to choose a simple transformation that can compress all fields contained in region $0 \leq r \leq R_2$ into the region $R_1 \leq r \leq R_2$. Let r' and r be the radial coordinates in the original space and the new space, respectively; and let the function f be the so-called coordinate transformation so that:

$$r' = f(r). \tag{4.1}$$

Obviously, r' and r can be connected according to the following expression:

$$r = R_1 + r' \frac{R_2 - R_1}{R_2}. \tag{4.2}$$

In this manner, $r' = 0 \Rightarrow r = R_1$ and $r' = R_2 \Rightarrow r = R_2$, in accordance with the space compression we want to carry out. Finally, Eqs. 4.1 and 4.2 lead to

$$f(r) = \frac{r - R_1}{R_2 - R_1} R_2, \tag{4.3}$$

which is the transformation used in [61] (the prime symbol convention is different). But from a general point of view, it should be noted that any continuous function f is suitable as long as $f(R_1) = 0$ and $f(R_2) = R_2$ [63], as it is the case for Eq. 4.3. In particular, a non-linear function such as

$$f(r) = \left(\frac{r - R_1}{R_2 - R_1}\right)^{1/\alpha} R_2 \tag{4.4}$$

can be used [64, 65]. If $\alpha = 1$, Eq. 4.4 gives again 4.3.

One remaining worry: What is the expression of the new permittivity and permeability? A transformation approach provides them in terms of f; deep details of the procedure can be found in [66].

- **2D cloak** The constitutive parameters of a cylindrical cloak turn out to be given by

$$\varepsilon_r = \mu_r = \frac{1}{f'} \frac{f}{r}, \tag{4.5a}$$

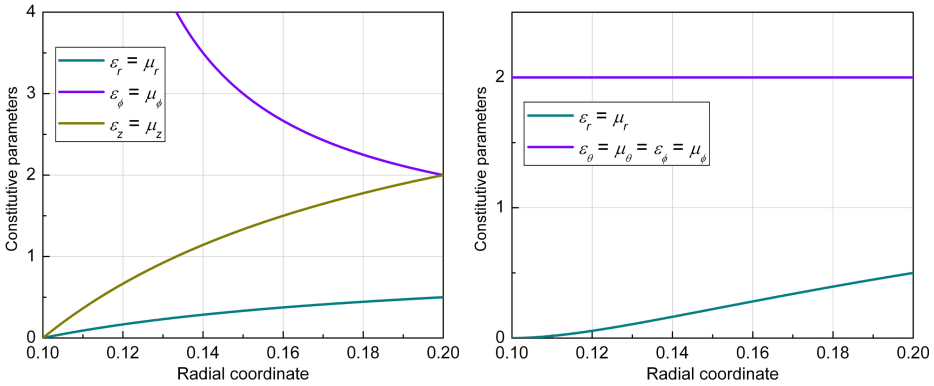

(a) (b)

Figure 4.2: Plot of the constitutive parameters for **(a)** a cylindrical cloak, and **(b)** a spherical cloak. In this example, the inner and outer boundaries of the cloak have been chosen to be $R_1 = 0.1$ and $R_2 = 0.2$, respectively.

$$\varepsilon_\varphi = \mu_\varphi = f' \frac{r}{f}, \tag{4.5b}$$

$$\varepsilon_z = \mu_z = f' \frac{f}{r}, \tag{4.5c}$$

f' being the derivative of the function f. This leads, using the expression of f given by Eq. 4.3, to

$$\varepsilon_r = \mu_r = \frac{r - R_1}{r}, \tag{4.6a}$$

$$\varepsilon_\varphi = \mu_\varphi = \frac{r}{r - R_1}, \tag{4.6b}$$

$$\varepsilon_z = \mu_z = \left(\frac{R_2}{R_2 - R_1} \right)^2 \frac{r - R_1}{r}. \tag{4.6c}$$

Each one of these optic constants is plotted in Fig. 4.2(a).

- **3D cloak** For a spherical cloak, we get

$$\varepsilon_r = \mu_r = \frac{f^2}{r^2 f'}, \tag{4.7a}$$

$$\varepsilon_\varphi = \mu_\varphi = f', \tag{4.7b}$$

$$\varepsilon_\theta = \mu_\theta = f', \tag{4.7c}$$

which, using the expression of f given by Eq. 4.3, leads to

$$\varepsilon_r = \mu_r = \frac{R_2}{R_2 - R_1}\left(\frac{r - R_1}{r}\right)^2, \tag{4.8a}$$

$$\varepsilon_\theta = \mu_\theta = \frac{R_2}{R_2 - R_1}, \tag{4.8b}$$

$$\varepsilon_\varphi = \mu_\varphi = \frac{R_2}{R_2 - R_1}. \tag{4.8c}$$

These constitutive parameters are plotted in Fig. 4.2(b).

This means that the process consists in surrounding the object we want to make invisible by an anisotropic material whose permittivity and permeability are tensors given by:

$$\begin{aligned} \bar{\bar{\varepsilon}} &= \varepsilon_r(r)\widehat{rr} + \varepsilon_\varphi(r)\widehat{\varphi\varphi} + \varepsilon_z(r)\widehat{zz}, \\ \bar{\bar{\mu}} &= \mu_r(r)\widehat{rr} + \mu_\varphi(r)\widehat{\varphi\varphi} + \mu_z(r)\widehat{zz}, \end{aligned} \tag{4.9}$$

for the 2D case, and given by:

$$\begin{aligned} \bar{\bar{\varepsilon}} &= \varepsilon_r(r)\widehat{rr} + \varepsilon_\theta(r)\widehat{\theta\theta} + \varepsilon_\varphi(r)\widehat{\varphi\varphi}, \\ \bar{\bar{\mu}} &= \mu_r(r)\widehat{rr} + \mu_\theta(r)\widehat{\theta\theta} + \mu_\varphi(r)\widehat{\varphi\varphi}, \end{aligned} \tag{4.10}$$

for the 3D case. This prescription will exclude all fields from the central region, while no field can escape from this region.

Note in passing that the cloaking material constants given by Eqs. 4.6 and 4.8 can take values less than unity. Concretely, for the 2D cloak, the radial components are less than unity and the azimuthal ones are greater than unity for all r such that $R_1 < r < R_2$; while the vertical components are less than one for $R_1 < r < \frac{R_2^2}{2R_2 - R_1}$ and greater than one for $\frac{R_2^2}{2R_2 - R_1} < r < R_2$. For the 3D cloak, only the radial components can be unusual: they are less than unity for all r. Hence, the cloaking structure is obviously a metamaterial and its modeling requires the use of special nodes such as those presented in section 2.5.

Furthermore, it is worth emphasizing that the φ-components, Eq. 4.6b, tend to infinity at the cloak's inner boundary, i.e., $r = R_1$; while the r-components in Eqs. 4.6a and 4.8a, as well as the z-components in Eq. 4.6c are zero. These exotic values will give rise to discussion in the next sections.

4.3 Review on cloaking

Since the publication of the precursor article [61], the cloaking topic has received much attention. We propose hereinafter a review on the recent progress.

The work proposed by Pendry *et al.* was mainly devoted to the presentation of the cloaking concept obtained by coordinate transformations. Beyond that, the authors discussed whether the cloaking effect is broadband or specific to a single frequency. In this sense, they pointed out that the phase velocity within the cloaking shell must be greater than the velocity of light in vacuum, which violates no physical law. However, the group velocity can never exceed it. Therefore, presence of dispersion is required so that the phase and group velocity will be different. Consequently, the cloaking parameters must disperse with frequency, leading to the conclusion that the cloak is only efficient at a single frequency, except if the constitutive parameters are tunable. In this sense, let us mention the work proposed by D. Wang *et al.* in which a cloak based on active metamaterials is presented [67], the working frequency having the ability of being reconfigurable.

After having proven that a cloak of invisibility is theoretically possible, at least over a narrow frequency band, Schurig *et al.* proposed the first practical realization of a 2D cloak [68]. The cloak was constructed by using structured metamaterials made up of split ring resonators, which are known to exhibit strange magnetic properties if they are activated by a magnetic field normal to the plane of the rings [69]. The design of the cloak is shown in Fig. 4.3. The incident electromagnetic wave was TE (electric field along the axial z-direction), which means that only μ_r, μ_φ, and ε_z are relevant in Eq. 4.6. Moreover, they simplified the realization by reducing the parameters given by Eq. 4.6 [64, 70]. Instead they assume that $\mu_\varphi = 1$, which leads to another set of equations:

$$\mu_r = \left(\frac{r-R_1}{r}\right)^2, \tag{4.11a}$$

$$\mu_\varphi = 1, \tag{4.11b}$$

$$\varepsilon_z = \left(\frac{R_2}{R_2-R_1}\right)^2. \tag{4.11c}$$

Using Eq. 4.11 has the benefit of making only one component spatially inhomogeneous and also eliminates any infinite values, which are difficult to experimentally implement. Of course the efficiency of the cloak is expected to be affected by such a prescription. In section 4.5, we will come back on the reduced pa-

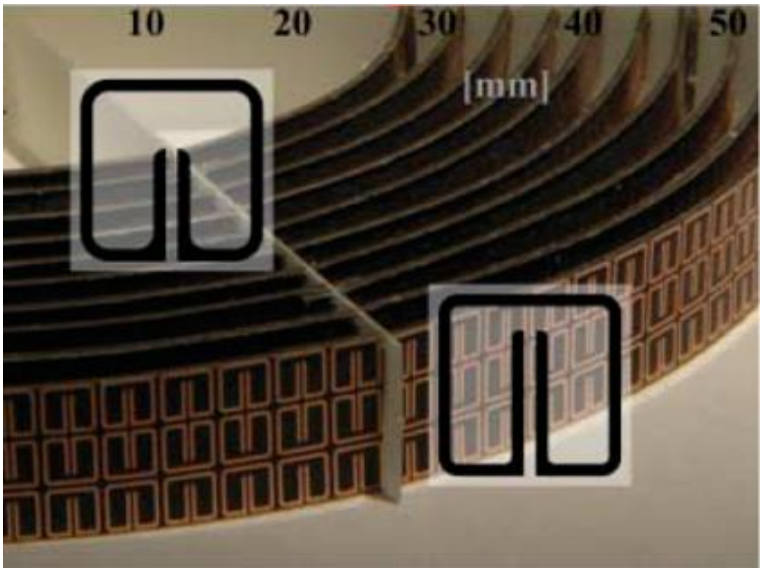

Figure 4.3: Schurig *et al.*'s experimental cloak made up of split ring resonators [68].

rameters. Finally, the experimental results show good agreement with numerical simulations, the experimental cloak being able to significantly decrease scattering from the hidden object.

More insight into the physics behind the cloaking has been obtained from analytical scattering model. In this sense, Chen *et al.* analytically established the interactions between electromagnetic waves and spherical cloaks by using a full wave Mie scattering model [71]. Thanks to this description, they could confirm that the total scattering cross section of an ideal cloak, i.e., rigorously described by Eq. 4.8, is absolutely zero. Another interesting conclusions they drew are in regard to the nonideal cloak. They made the device imperfect by introducing losses to the material, and observed that the scattered power increases as the loss increases, except in the backward direction for which the scattering remains zero, irrespectively of the value of the loss. Furthermore, as long as the ratio between the radial and angular component of the permittivity/permeability in Eq. 4.8 has the same value, that is $(r-R_1)^2/r^2$, the field cannot penetrate the concealed region, even if the material is lossy. This means that the scattered power is wholly induced by the cloak itself.

All these original properties are peculiar to the spherical cloak and does not hold for its 2D equivalent, the cylindrical cloak. First, Ruan *et al.* demonstrated

that the ideal 2D cloak is perfect [72]. The study of a nonideal cloak is also important given that experimental realizations have to adopt some approximations as we have mentioned before; in particular, the infinite value of ε_φ and μ_φ at $r = R_1$ makes the inner boundary of the cloak arduous to describe. Hence, figuring out how sensitive the device is to finite perturbations is widely significant. In the same paper, Ruan *et al.* thus introduced a small deviation into the ideal cloak, and instead of strictly calculate the value of the electromagnetic constants at the inner boundary, they calculate them at a very small distance, δ, from it. In this manner, the effect of δ on the performance of the cloak can be observed; by gradually decreasing the δ value, they showed that the convergence toward the no-scattering situation is a very slow process: as long as δ is not strictly zero, the incoming wave can penetrate the hidden region and can be scattered. This means that the cylindrical cloak is highly sensitive to slight perturbations. Zhang *et al.* gave a physical explanation to this phenomenon [73]: in the ideal case, a surface current that shields the concealed region appears at the inner boundary of the cloak. This surface current is a consequence of the infinite value of ε_φ and μ_φ. So, the nonideal case differs in one important respect: the lack of surface current at $r = R_1$ that permits the field to enter the hidden region. Furthermore, it is also proven in the same paper, that for a cylindrical cloak made up of a lossy material, the scattering occurs along all the directions, particularly in the backward one, unlike the spherical case.

Still concerning theoretical contributions, Chen *et al.* obtained the energy transport velocity distribution for a 3D ideal cloak [74]. They showed that the transport velocity near the inner boundary tends to zero, resulting in long time-delays for beams to cross the cloak. Let us also mention a work proposed by the same authors dealing with the curious concept of anticloak [75]. By anticloak, they mean a kind of materials obtained by coordinate transformations that have the capability of defeating the cloaking effect of an invisible cloak. The last two issues will be discussed, completed, and improved in sections 4.7.3 and 4.8.

4.4 Numerical simulations of cloaks

As we have discussed in section 4.3, invisible cloaking has been the matter of many studies spanning different approaches since Pendry's original paper. By analytically solving Maxwell's equations, it has been possible to theoretically analyze the cloaking phenomenon and interpret the underlying physics. Furthermore, the

first practical realization of a cloak has confirmed the model to be experimentally feasible.

Naturally, numerical simulations have an important role to play here through the useful information they are able to provide. In this sense, the first modeling of a cloaking structure was reported by Cummers *et al.*, who proposed a full-wave finite-element simulation to confirm the effectiveness of the transformation [70]. In addition, they used in the related paper simplified permittivities and permeabilities to show that the arising reduced cloaking materials exhibit good performance. Nevertheless, these calculations are performed with a commercial software, Comsol Multiphysics, which does not allow the versatility needed in some situations. Afterward, most of the contributions about invisibility involved numerical simulations based on Comsol. The aim of the following sections is to propose a cloak modeling based on our own TLM code for more flexibility. Moreover, employing a time domain method as TLM presents several assets. The most obvious are that the process dynamics of the cloaking phenomenon can be studied and that a simple Fourier Transform can provide its complete frequency behavior.

4.5 Cloaks made up of alternating isotropic layers

Before we rush to carry out our first modeling of a cloaking structure, we must pause to consider some important issues. Indeed, the simulation of an invisible cloaking with TLM is not straightforward. In the first paper we published [16], we faced two main difficulties that we had to fix:

1. The first one lies in the fact that the cloak requires the use of metamaterials, i.e., materials with relative constitutive parameters below unity and, in particular regions, values very close to zero. In their original forms, the classical TLM nodes are unable to model such media without some modifications. As it has been mentioned in section 2.5, So *et al.* have proposed a TLM node for modeling metamaterials [43]. But as they pointed out, their approach required significant modifications to the original TLM procedure, making the use of the related method difficult to implement. Fortunately, we have shown in section 2.5 that such a drastic modification is actually not necessary [15, 16].

2. The second difficulty comes from the anisotropic nature of the coating material. In its original form, TLM works with Cartesian nodes leading to

permittivity and permeability tensors that exhibit off-diagonal elements in Cartesian coordinates. The modeling of anisotropic materials in TLM was presented in [76, 77], however the proposed implementation in both cases is very complicated, and, anyway would not permit the simulation of metamaterials easily. On the other hand, Huang *et al.* have proposed an approach that allows substituting the anisotropic medium by a concentric layered structure of alternating homogeneous isotropic materials [78]. The angular $(\varepsilon_\varphi, \mu_\varphi)$ and radial (ε_r, μ_r) components of the electromagnetic (EM) parameters can indeed be considered as the effective permittivity or permeability of a composite made of a series of parallel layers whenever the layers are thin enough compared with the wavelength. This statement is based on the effective medium theory and permits to match the angular components with the upper Wiener's bound, while the radial components correspond to the lower Wiener's bound [50]. We will choose this technique to carry out our first cloaking simulation.

We can now tackle the modeling. Let us consider a plane wave incident upon an infinite Perfect Electric Conductor (PEC) cylinder of radius R_1. The incident wave is a 2 GHz TE polarized plane wave with electric field parallel to the axis z of the cylinder. The incident wave vector, $\bar{k}$, is x-oriented while the magnetic field is y-oriented. The PEC cylinder is surrounded by a cloaking material with outer radius R_2. According to the coordinate transformation, the anisotropic relative permittivity and permeability of the cloaking material in cylindrical coordinates follow the radius dependence formulas given by Eq. 4.6. Moreover, since the polarization is TE, the only constitutive parameters of interest are ε_z, μ_r, and μ_φ. As mentioned above, it has been shown that the anisotropic cloaking shell can be mimicked by concentric alternating layers made up of two homogeneous isotropic sub-layers A and B [78], chosen in this study to have the same thickness. The permittivity, ε_z, of each one is thus given by Eq. 4.6c, while the permeabilities μ_A and μ_B can be obtained from the Wiener's formula. In this manner, Eqs. 3.4a and 3.4b leads to

$$\mu_\varphi = \frac{\mu_A + \mu_B}{2}, \tag{4.12a}$$

$$\frac{1}{\mu_r} = \frac{1}{2\mu_A} + \frac{1}{2\mu_B}, \tag{4.12b}$$

respectively. From this set of equations, μ_A and μ_B take the values

$$\mu_A = \mu_\varphi + \sqrt{\mu_\varphi(\mu_\varphi - \mu_r)}, \tag{4.13a}$$

$$\mu_B = \mu_\varphi - \sqrt{\mu_\varphi(\mu_\varphi - \mu_r)}, \tag{4.13b}$$

where μ_r and μ_φ are given by Eqs. 4.6a and 4.6b, respectively.

The TE-node presented in section 2.3.1 is employed to model this problem and obtain the electric field distribution. A TLM mesh formed with 2800 nodes along the x- and y-directions is used for the modeling. The node size is $\Delta x = \Delta y = 5.10^{-4}$ m and the maximum allowable time step for these lengths, $t = 1.1785$ ps, is used. Typically, the boundary conditions used in cloaking studies are chosen to be absorbent along the direction of propagation and Perfectly Magnetic Conducting (PMC) for vertical directions [70], i.e., along the y-direction in this work, which is equivalent to artificially simulate a periodic structure of cylinders along the y-direction. However, the cloaking we are numerically considering is not ideal, and so a certain scattering is expected at each cylinder. In this manner, if we want to characterize the cloaking performance of the coating for a given cylinder, the existence of neighbor cylinders in the periodic structure would artificially magnify the non-ideality of the results. In other words, we are interested in the study of the capability of a single coating structure to make a certain region invisible, and deviations of this ideal goal are better identified if only one coating element are considered. In this sense, the PMC boundaries are not a satisfactory choice but, on the other hand, they cannot be directly substituted by absorbent boundaries because the plane wave condition corresponding to excitation would be broken. The problem is worked out by employing the Huygens surface technique which consists of dividing the mesh into an inner total field (incident and scattered) region and an outer scattered field region, as depicted in Fig. 4.4. The source conditions for the plane wave excitation are then enforced on the interface separating these regions, which presents two benefits: first, absorbing boundary conditions can be directly applied to the limits of the mesh, since excitation has been removed at these points; and second, an illustrative map of the scattered field is directly obtained at the outer region. Finally, the far field will be obtained in all cases using the transformation proposed in [79]. The technique considers the tangential EM fields on an imaginary surface surrounding the cylinder in the scattered field region as equivalent electric and magnetic sources. A numerical integration, together with a frequency-dependent amplitude transformation which allows using

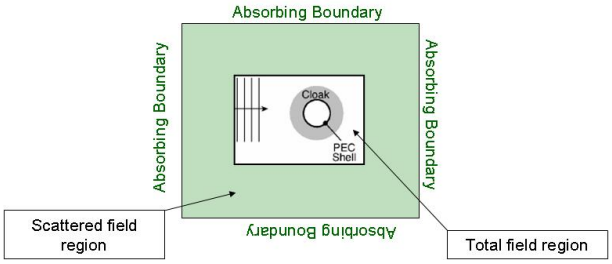

Figure 4.4: Computational domain using Huygens surface technique.

a 3D scheme on a 2D problem, provides the far field response. For the numerical simulation, the cloaking shell is made up of 10 pairs of layers A-B (in total, 20 sub-layers) and $R_1 = 0.1$ m while $R_2 = 0.2$ m. This means that the thickness of a single layer is 1 cm, while the wavelength of the incident wave is 15 cm: the thin layer condition is thus satisfied [78]. First, ε_z, μ_r, and μ_φ are calculated at the center of the isotropic layers (i.e., at the interface separating layer A and layer B), the corresponding far field pattern is depicted in Fig. 4.5 (red color). For comparison, this field has been normalized by the maximum value of the field when no cloaking structure is present. This reference far field pattern, which is checked to perfectly coincide with the theoretical one [80], can be observed in the same figure. A significant reduction of the scattering is noticed in almost all directions at the notable exception of the forward scattering. By judiciously adjusting the simulation parameters, we will show below that this scattering reduction can be enhanced.

Instead of calculating the parameters ε_z, μ_r, and μ_φ at the center of the isotropic layers, we now calculate them at the boundary between each layer. However, this process gives an infinite value of μ_φ for the first layer (at $r = R_1$) and, therefore, the electromagnetic parameters will not be calculated exactly at the inner boundary of the layers but at a distance $10^{-4}\delta$ of the later, where δ is the thickness of one layer. The far field pattern is displayed in Fig. 4.5 (blue color) and, compared to the previous case, shows an even stronger scattering reduction. This reduction now occurs for all the direction and the forward scattering has been in particular reduced by 4.3 dB, while the backward scattering has been reduced by 15.1 dB. This confirms that the cloaking performance is highly sensitive to the value of the parameters of the inner layer since it is the most affected layer by this change. Furthermore, the simulated electric field in the last case is plotted in Fig. 4.6. It is straightaway clear that, once in the cloaking shell, the wave front is deviated and

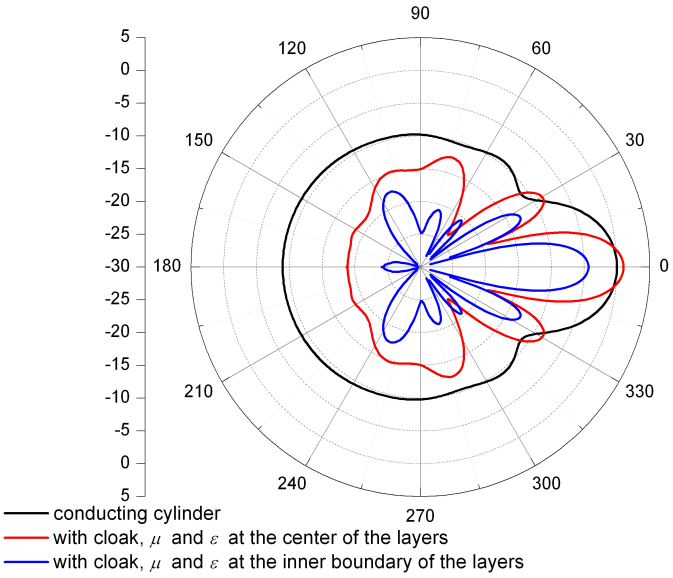

Figure 4.5: Far field pattern for an uncloaked cylinder and for two different cloaking made up of alternating layers. The incident plane wave is TE.

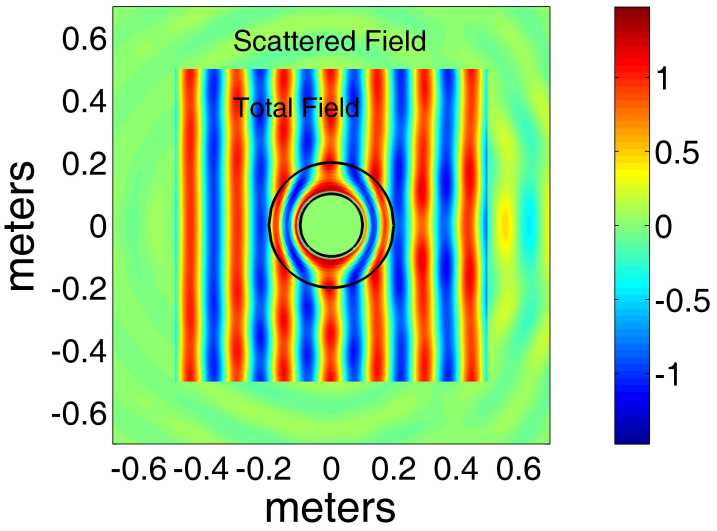

Figure 4.6: Total and scattered amplitude field plot at the vicinity of the coated cylinder for ε and μ sampled at the inner boundary of each layer.

conducted around the cloaked cylinder, while outside the object under consideration, it emerges almost unperturbed. Moreover, the Huygens technique allows visualizing in the same picture the scattered field at the outer almost green square region, with the incident field directly filtered out, that ostensibly takes the form of concentric waves. To give more insight into the physics behind, let us mention that the presence of the concentric scattering is mainly due to the absence of the magnetic surface current on the inner boundary of the cloak [73] we have mentioned in section 4.3. Indeed, for an ideal cloaking, the permittivity and permeability for $r = R_1$ is enforced by Eq. 4.6 to be $\varepsilon_z \to 0$, $\mu_r \to 0$, and $\mu_\varphi \to \infty$. These extreme values induce a magnetic surface current exactly located at the inner boundary of the cloak once illuminated by the incident wave. Such a current shields the cloaked region and then avoids the field to enter this area. On the other hand, $\mu_\varphi(R_1)$ is not infinite in our simulation, so this surface current does not exist here and, then, scattering occurs on the interface of the PEC cylinder, making the cloaking structure of Fig. 4.6 imperfect.

In order to facilitate experimental realization (see section 4.3) or in order to avoid infinite values for the electromagnetic constants, reduced material parameters are often used for the cloaking shell. These reduced parameters usually consist of choosing one of the constants to be unity, the penalty being only the loss of the reflectionless property, because of the mismatch of the impedance conditions, as claimed in some papers [68, 70]. Nevertheless, Yan *et al.* have showed that using reduced parameters experiments more scattering than intended and is more than just nonzero reflectance [81]. To verify this statement for the proposed layered cloaking structure, the far field calculation is calculated for two types of reduced parameters and displayed in Fig. 4.7(a). One corresponds to $\mu_\varphi = 1$, while the other one to $\varepsilon_z = 1$ (the choice $\mu_r = 1$ is not allowed since the corresponding ε_z would not be spatially uniform), both with parameters calculated at the center of the layers. As expected, the performance of the cloaking is deteriorated; however, it is worth noting that in both cases the forward scattering is now reduced especially for the choice $\varepsilon_z = 1$ (by 7dB). Finally, it is worth noting from Fig. 4.7(a) that the greater the reduction in the forward direction, the lesser the reduction in the backward direction, which seems to be associated to energy conservation.

Similarly, it is of interest to study the effect of a nonlinear transformation on the effectiveness of the proposed layered cloaking structure [63, 65]. A nonlinear transformation can be characterized by the coordinate transformation of Eq. 4.4. Consequently, the electromagnetic parameters of Eqs. 4.6 turn out to be changed

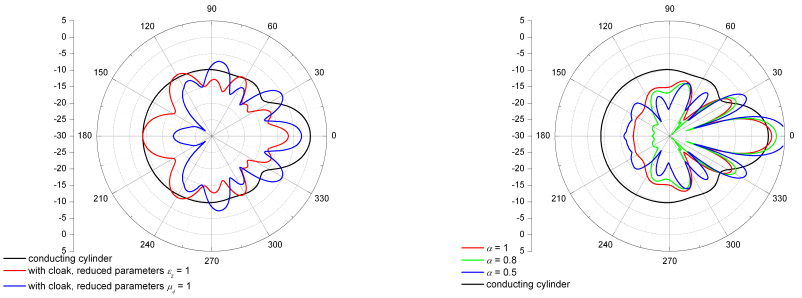

(a) (b)

Figure 4.7: **(a)** Far field pattern for reduced parameters. **(b)** Far field pattern for non-linear transformations.

into:

$$\varepsilon_r = \mu_r = \alpha \frac{r - R_1}{r}, \tag{4.14a}$$

$$\varepsilon_\varphi = \mu_\varphi = \frac{r}{\alpha(r - R_1)}, \tag{4.14b}$$

$$\varepsilon_z = \mu_z = \frac{R_2^2}{(R_2 - R_1)^{2/\alpha}} \frac{(r - R_1)^{2/\alpha - 1}}{\alpha r}, \tag{4.14c}$$

where $\alpha \in]0,1]$. Note that the value $\alpha = 1$ corresponds to the linear transformation. The far field pattern, for $\alpha = 1$, $\alpha = 0.8$, and $\alpha = 0.5$, is depicted in Fig. 4.7(b) for the full parameters of Eq. 4.6 calculated at the center of the layers. It can be observed that the choice $\alpha = 0.8$ globally improves the cloaking performance, particularly for angle contained between 90^o and 270^o in the backward direction. Concerning the $\alpha = 0.5$ transformation, it appears that the result is not convincing although it offers some improvement for some directions.

As mentioned in section 2.5, modeling electromagnetic fields by means of transmission line networks is a well-known technique harking back to the works proposed by Whinnery *et al.* in the 1940s [28]. Furthermore, the fact that these networks support backward-waves has sometimes been mentioned, notably by the same authors in a textbook [40], but without any practical applications. However the impressive progress in the design of metamaterials pushed Eleftheriades *et al.* to proposed an alternate perspective to the usually employed discrete periodic scatters: they designed metamaterials that exploit the *L*-*C* distributed network [39]. By simply interchanging the position of *L* and *C*, they obtained

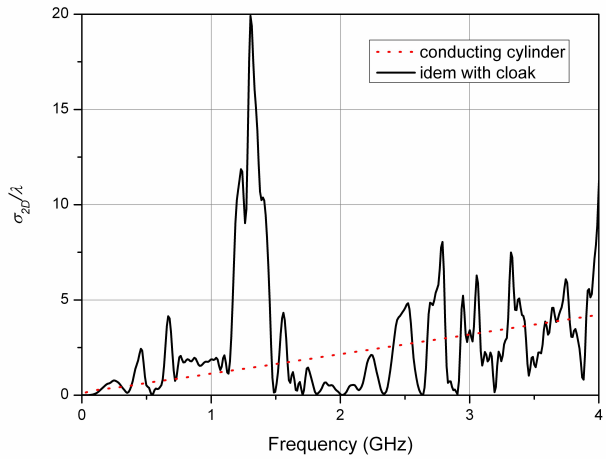

Figure 4.8: 2D scattering width, σ_{2D}/λ, versus frequency of a conducting cylinder and cloaked cylinder whose working frequency is 2 GHZ.

an equivalent dispersive material that assumes negative values for both ε and μ. Therefore, a cloaking structure could also be built with such a network. Given that TLM is nothing more than the numerical incarnation of a *L-C* network, the results obtained with TLM are expected to exactly follow the behavior of the real structure. This means that the TLM solution is expected to reproduce the behavior of the cloaking material not only at the design frequency of 2 GHz, but also for a wide-band of frequencies by using a simple Fourier Transform. We have shown in section 2.6 that the TE-node we are employing here behaves according to the Drude model, which makes the modeling realistic. Let us consider, the most efficient cloaking, depicted in Fig. 4.6, that was obtained with the electromagnetic parameters calculated at the inner boundary of each layers. By doing a Fourier transform of the response to a Gaussian-shaped incident field, information at other frequencies can be directly obtained from a time domain simulation. Fig. 4.8 shows the 2D backscattering width normalized to λ, σ_{2D}/λ, for the cloaking device compared to that of the simple conducting cylinder. As expected, 2 GHz is the frequency for which the effectiveness of the cloaking material is optimum. However, the resonant nature of dual *L-C* networks causes that regions of reduced and magnified radiation alternate on both sides of the 2 GHz design frequency.

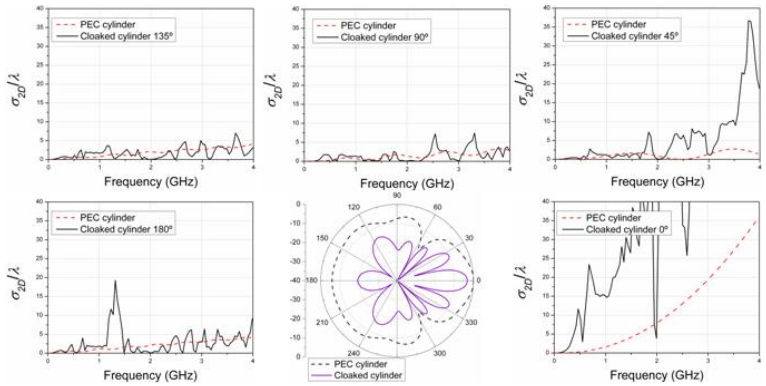

Figure 4.9: Far field pattern of a cloaking structure at 2 GHz, and its scattering width versus frequency for 0^o, 45^o, 90^o, 135^o, 180^o.

Having the far backward scattering of the cloak on hand, we can compute it in other directions. In order to validate the TM-node (section 2.3.2) as a suitable node for the modeling of cloaking structures, we now consider a TM plane wave (magnetic field parallel to the axis of the cylinder). The geometry of the object is precisely the same, i.e., it is made up of 10 pairs of layers A-B. Moreover 2 GHz is still chosen to be the working frequency, the far field pattern at this frequency is depicted in Fig. 4.9. By using a simple Fourier Transform, the far field in terms of the frequency for five different angles (from 0^o to 180^o using 45^o steps) is obtained and shown in the same Fig. 4.9, around the polar plot. As expected, the cloaking shell is manifestly efficient for the 2 GHz functional frequency, but it is worth noting that a frequency band appears around this frequency for all directions at the noticeable exception of 0^o. This last direction is characterized by a very narrow low radiation region, which remarks that it is the most conflictive direction.

For completion sake, the scattering from 0^o to 135^o is also computed for the TE mode; it turns out that the results for this polarization are exactly the same as for the TM mode. This means that, although the cloaking is not perfect, the PEC cylinder is well concealed by the cloaking shell. Indeed, it is well known, and moreover verified by our TLM simulations, that the scattering width of a simple circular conducting cylinder depends strongly on the polarization. In order to get a decisive confirmation of this observation, the PEC cylinder is substituted by free space, and once again, the same results are obtained. This means that the scattering we are observing is in fact only due to the cloaking shell, irrespectively

of the object located in the concealed region. To explain this, let us note that the first layer of the cloaking shell in our simulation has a relative permittivity $\varepsilon = 2.10^5$, and relative permeability $\mu = 4.10^{-5}$. It is reasonable to think that these extreme values shield the central region. Nevertheless, the other layers are not perfectly able to steer the radiation around themselves due to the numerical discretization and to the approximation consisting on substituting the theoretical anisotropic material by isotropic layers, which produces the observable forward scattering.

4.6 Modeling of cloaks with curved TLM nodes

4.6.1 Cylindrical cloaks

We have shown in the previous sections that to be effective, the dielectric and magnetic constants of the anisotropic cloaking shell must take the specific values given in Eq. 4.6. The permittivity and the permeability are both expressed in cylindrical coordinates. However, Cartesian coordinates are usually employed in the papers dealing with numerical simulation of cloaking structures [15,16,70,82,83]. In our case, using Cartesian coordinates has required substituting the anisotropic material by a concentric layered structure of alternating homogeneous isotropic material since TLM cannot easily process tensors with off-diagonal elements. This has been the matter of section 4.5. But, beyond that, Cartesian coordinates lead to staircase approximations when one wants to model the curved geometry, as mentioned in [82].

In order to reduce these numerical errors, we propose in this section to carry out the study with the TLM cylindrical nodes presented in sections 2.4.1 and 2.4.2. The shape of these special nodes assumes the geometry of the cloaking shell. Therefore, with such nodes, it is not necessary to approximate the curved geometry with many Cartesian cells anymore, the number of nodes filling the mesh is then highly reduced without losing details in the central area. Moreover, the cylindrical node directly simulates permittivity and permeability with cylindrical components, so that the A-B layers technique does not have to be employed.

We have mentioned in section 4.1 that ε_φ and μ_φ tend to infinity at the inner boundary of the cloak. In order to push further the accuracy of the modeling, it would be convenient to be able to model infinite values for ε and μ, which would avoid approximations arising from the truncation of the inner layer. We are going to show that, with TLM, such extreme values do not have any detrimental conse-

quence, since the limits of the TLM scattering matrix elements still remain finite in this case. Let us consider the TM-node (components of the electromagnetic field: E_x, E_y, H_z) presented in section 2.3.2, and let us consider the elements of the scattering matrix in Eq. 2.63. As in section 2.3.2, let k represents coordinate x or y.

1. $\varepsilon_k \to \infty$.
   In this case, the admittance Y_k of the capacitive stub tends to infinity. Eq. 2.64 becomes:

$$\begin{aligned} a_k &= -\tfrac{2}{4+Z_z} & f &= \tfrac{4-Z_z}{4+Z_z} \\ b_k &= -1+\tfrac{2}{4+Z_z} & g &= \tfrac{2}{4+Z_z} \\ c &= \tfrac{2}{4+Z_z} & h_k &= 1 \\ d &= \tfrac{2Z_z}{4+Z_z} & i_k &= 2 \\ e_k &= 0 \end{aligned} \tag{4.15}$$

2. $\mu_z \to \infty$.
   In this case, the impedance Z_z of the inductive stub tends to infinity. Eq. 2.64 becomes:

$$\begin{aligned} a_k &= \tfrac{2}{2+Y_k} & f &= -1 \\ b_k &= -\tfrac{Y_k}{2+Y_k} & g &= 0 \\ c &= 0 & h_k &= \tfrac{Y_k-2}{Y_k+2} \\ d &= 2 & i_k &= \tfrac{2Y_k}{Y_k+2} \\ e_k &= \tfrac{2}{2+Y_k} \end{aligned} \tag{4.16}$$

3. $\varepsilon_k \to \infty$ **and** $\mu_z \to \infty$.

In this case, both Z_z and Y_k tend to infinity. Eq. 2.64 become:

$$\begin{aligned} a_k &= 0 & f &= -1 \\ b_k &= -1 & g &= 0 \\ c &= 0 & h_k &= 1 \\ d &= 2 & i_k &= 2 \\ e_k &= 0 \end{aligned} \tag{4.17}$$

Therefore, the elements of the matrix effectively remain finite in all case: infinite ε and μ can be used in the modeling, contributing to the improvement of the accuracy of the numerical simulation.

As it has been done in the previous section, a cloaked infinite PEC cylinder surrounded by free space is modeled. The cloaking shell, with $R_1 = 0.1$ m and $R_2 = 0.2$ m, is made up of 200 layers, which means that there are 200 TLM nodes in the radial direction, r, inside the shell. Note that the cylindrical cloak presents an obvious symmetry. The electromagnetic field is therefore supposed to be the same on both sides of the symmetrical axis; this means that the mesh to be modeled can be divided by two. The whole mesh is finally constituted by 1000 nodes along r, and 180 nodes rectifier along the azimuth φ (one per degree). The total number in the mesh is 180000, which is more than 40 times less than the mesh used in section 4.5. To be exact, the mesh in section 4.5 was not reduced by two when the symmetry allowed it. But even like that, the number of nodes involved in the current modeling would have been 20 times less. That is why we are able to model a cloak with a significant number of layers. Again, the Huygens surface technique is used in order to be able to employ absorbing boundary conditions at the outer boundaries of the mesh. The frequency of the TM incident plane wave (modeled by a sinusoidal signal in the numerical simulation) is 2 GHz. The magnetic field plot for the uncloaked cylinder is depicted in Fig. 4.10(a), while that for the cloaked cylinder is plotted in Fig. 4.10(b). The difference in terms of scattering between the two last figures is very substantial. It is plain from Fig. 4.10(b) that the cloaking effect can be achieved with high precision by using the TLM modeling proposed here; this is particularly evident in region 4, where the scattering is almost zero in all the directions. Region 2 clearly illustrates how energy is

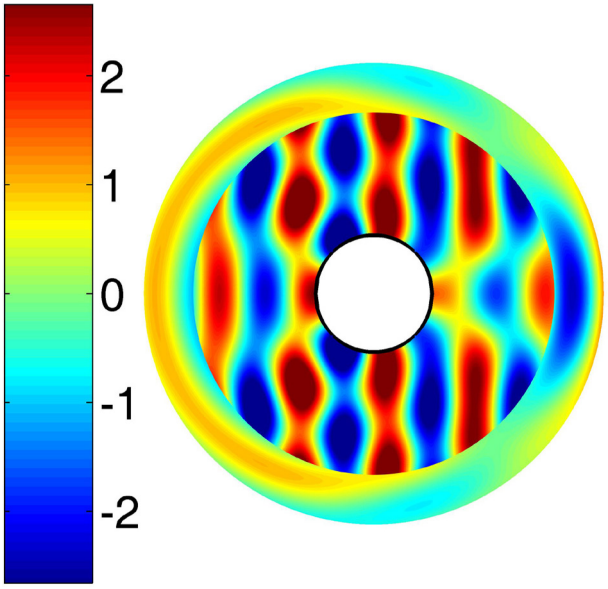

(a)

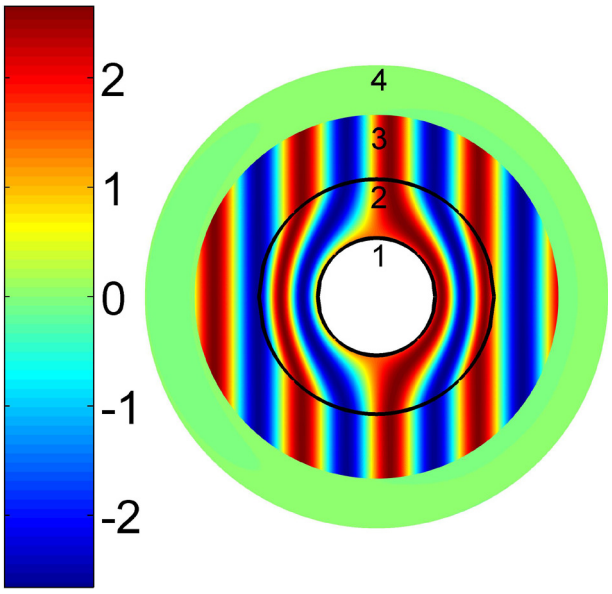

(b)

Figure 4.10: **(a)** Magnetic field ($\times 10^{-3}$) mapping in the vicinity of a PEC cylinder at 2 GHZ. **(b)** Magnetic field ($\times 10^{-3}$) mapping in the vicinity of a cloaked PEC cylinder at 2 GHZ once stability has been reached. Four regions are apparent: (1) Cylinder, (2) Cloaking shell, (3) Free space, (4) Scattering region.

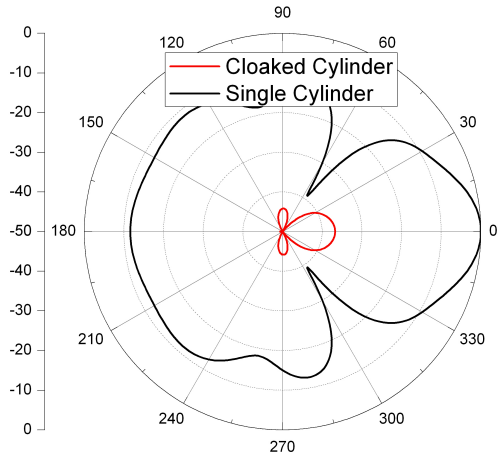

Figure 4.11: Far-field pattern comparison between cloaked cylinder and single cylinder.

smoothly bent around the cylinder, while region 3 seems to be unperturbed by the presence of the object.

Quantitatively, we have numerically calculated the far field; it is plotted in Fig. 4.11 and it turns out that the scattering in the far zone for the cloaked cylinder has been reduced by about 37 dB in the forward direction and backward directions, and even by more along other directions, compared to the simple cylinder scattering. This significant reduction attests that the cylindrical node is well suited for the modeling of cylindrical cloaking.

4.6.2 Spherical cloaks

In Pendry's precursor work [61], the analysis was focused on the description of a 3D spherical cloak. But since then and for the sake of simplicity, most of the attention has been given to the 2D cylindrical cloak. For instance, in order to avoid the difficulties inherent to the construction of a real 3D structure, the first experimental realization consisted of a cloaked copper cylinder [68]. Concerning the numerical simulations, the difficulty of 3D modeling lies in the high computational requirements; therefore, the works dealing with numerical simulations use to involve cylindrical cloaking [70]. Therefore, providing such a modeling is especially challenging. However, we have shown in section 4.6.1 that the number of required nodes to the modeling of a cylindrical cloak can be significantly reduced by using cylindrical nodes, the adverse effect being a diminution of the frequency

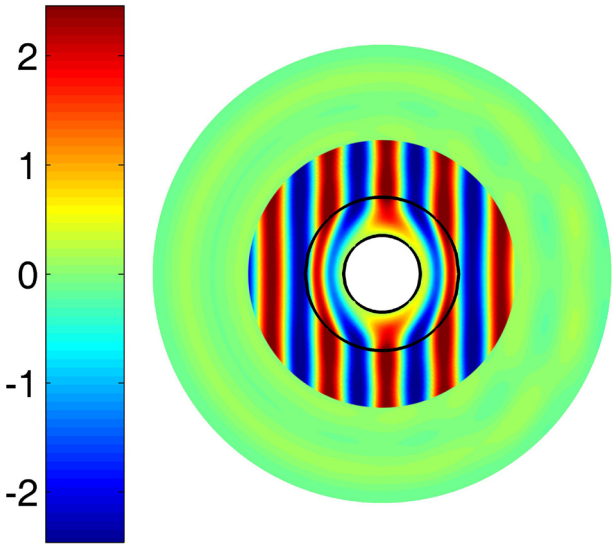

Figure 4.12: Magnetic field ($\times 10^{-3}$) mapping (in the plan corresponding to $\theta = \pi/2$) in the vicinity of the cloaked (with 40 layers) PEC sphere once stability has been reached.

range validity. In the same way, we now model a 3D cloak by employing the spherical node presented in section 2.4.3. The employed coordinate system is displayed in Fig. 2.11(a).

A plane wave with frequency 2 GHz is incident, along the x-direction, upon a PEC sphere cloaked by a shell made up of 40 layers. The magnetic field is z-oriented, while the electric field is y-oriented. The spherical structure presents a clear symmetry in the y- and z-directions, so that the whole mesh can be reduced to the quarter part. The spherical TLM node allows accurate modeling of the object shape with relatively few nodes. Indeed, the mesh is made up of 200 nodes in the r-direction, 90 nodes in the zenithal θ-direction (one by degree), and 180 in the azimuthal φ-direction (one by degree). The magnetic field plot, once the stability is reached, is depicted in Fig. 4.12. In order to ensure a consistent comparison with the cylindrical cloak, the plane perpendicular to the magnetic field is considered, i.e., $\theta = \pi/2$ in spherical coordinates. As expected, the wave front is well conducted around the PEC sphere in the shell, and emerges unperturbed in the free space surrounding the cloak. The magnetic field in the scattered region is clearly very weak. Nonetheless, it seems to be slightly more intense than it was for the cylindrical cloak; we believe this is due to low numerical errors arising from the poles of the sphere. Indeed, the poles have been shown to constitute conflictive

regions in section 2.4.3 given that the 180 TLM nodes along the φ-direction are adjacent at this precise point.

4.7 Two-dimensional dispersive cloaks

4.7.1 Dispersive constitutive parameters

To be ideal, a 2D cloak has to be:

- lossless,
- non-dispersive with frequency,
- anisotropic,
- made of spatially inhomogeneous metamaterial,
- made of material whose permittivity and permeability span the entire range from zero to infinity.

Otherwise, if one of this condition is not satisfied, the cloaking effect is imperfect. Actually, each one of this condition is difficult or even impossible to rigourously fulfill in practice. What is more, the non-dispersiveness violates the physical law of causality.

For instance, let us consider the lossless condition. The cloak is made up, at least partially, of metamaterial; given that such materials are not available in nature, the experimental fabrication proposed by Schurig *et al.* [68] required the use of a lattice of metallic split ring resonators [37], as shown in Fig. 4.3, that may exhibit, in a resonance frequency region, negative effective permeability; as well as periodic lattice of thin metallic wires that behaves as a medium with negative effective permittivity [36]. It is also worth mentioning here the design of an optical cloak, having a non-magnetic nature and working under TM illumination, proposed by Cai and his coworkers [84]. Using reduced parameters, $\mu_z = 1$, $\varepsilon_\varphi = (\frac{R_2}{R_2-R_1})^2$, and $\varepsilon_r = (\frac{R_2}{R_2-R_1})^2(\frac{r-R_1}{r})^2$, which prevent the material to be magnetic whereas ε_φ remains finite, Cai realized the required distribution of ε_r by using metal wires of subwavelength size in the radial direction that are embedded in a dielectric material. The cloaking shell can thus be assimilated to a composite material consisting in Cai's paper of silver nanowires embedded in a silica tube. A full-wave finite-element numerical analysis showed that the imaginary part of

ε_r is about 0.1, which is likely to weaken the cloaking effect. However, 0.1 being a small value, they showed that the cloaking effect can be decently achieved in these conditions. Finally, in both Schurig and Cai's cases, the introduction of metals into the structure creates unavoidable losses, which makes the lossless condition unlikely.

Furthermore, the non-dispersive condition is also affected by the presence of resonant structures. But in this case, there are deeper reasons that avoid a purely non-dispersive cloak. It has been pointed out by Pendry [61] that the cloak must disperse with frequency for the sake of causality. Imagine rays incoming on the cloak; once in the cloaking shell, each of the rays is required to follow a curved, and therefore longer, trajectory than it would have done in free space. Since the rays have to emerge from the cloaking shell with the same phase, the phase velocity must be greater than that of light in free space, which is pretty common and does not violate any physical law. However, in the absence of dispersion, the phase velocity is equal to the group velocity. Given that the group velocity cannot exceed that of light, the cloaking parameters of Eq. 4.6 must disperse. As a consequence, the cloak is efficient at a single working frequency we will refer to as ω_0 (actually, ω_0 is the angular frequency). For this reason, most of the works dealing with cloaking have long been focused on monochromatic waves [64, 71–73, 81, 85], which eludes the dispersion effect. In the same manner, the first works dealing with or proposing modeling of invisibility were carried out by using the commercial software package Comsol [70, 86] which is based on the finite-element method. Comsol is frequency domain technique that cannot take into account the effect of the dispersion. However, authors have also looked into more physical dispersive cloaks by employing time-domain methods, such as FDTD, which can better reflect the real physics process of cloaking [83, 87].

The same kind of comments holds for the other conditions. Nonetheless, the degree of invisibility depends on the degree of sensitivity of the detector (antennas, or eyes quite simply). So, one can imagine a nonideal cloak that is however undetectable if the ideal condition are almost reached. That is why it is interesting to move away from the ideal cloak and consider more physical situation.

As a time-domain method, TLM is well-suited to the study of dispersive cloaks. In sections 4.7.2 and 4.7.3, we wish to focus on two problems that involve the dispersive nature of the cloak: the frequency-shift [88] and time-delay [74] phenomenons.

Previously, an important issue is in regard to the dispersion of the cloaking material in the numerical modeling. Let us consider the linear coordinate transformation of Eq. 4.3 that leads to Eq. 4.6. Accordingly, the cylindrical cloaking shell is made up of an anisotropic material that involves different categories of EM constants: the azimuth component is always greater than one, the radial component is always less than one, while the axial component is either greater than one or less than one on both sides of the limit value $r = R_l = \frac{R_2^2}{2R_2 - R_1}$. We have show in sections 2.5 that the TLM mesh for the modeling of metamaterials is dispersive. We have calculated in section 2.6 that the dispersion generated by the TLM mesh is given by Eq. 2.150 if the polarization is TM or by Eq. 2.153 if the polarization is TE, relations that are reminiscent of a Drude's model for both the permittivity and permeability. To explain the similarity with Drude's model, let us consider a dispersive medium whose permittivity and permeability, represented by $\chi(\omega)$, follow the Drude's model [36, 89]

$$\chi(\omega) = 1 - \frac{\omega_p^2}{\omega^2}, \tag{4.18}$$

where ω_p is the plasma frequency and where the absorption is neglected (the usual damping term is equal to zero). From Eq. 4.18, we find that

$$\omega_p^2 = \omega_0^2[1 - \chi(\omega_0)] \quad \Rightarrow \chi(\omega) = 1 - \frac{\omega_0^2}{\omega^2}[1 - \chi(\omega_0)], \tag{4.19}$$

Note that if the dispersive medium under consideration is a cylindrical cloak, $\chi(\omega_0)$ is given by Eq. 4.6. We conclude that $\widetilde{\mu}_z$ and $\widetilde{\varepsilon}_r$ in Eq. 2.150, or $\widetilde{\varepsilon}_z$ and $\widetilde{\mu}_r$ in Eq. 2.153 are reminiscent of a Drude's model, the factor 1 being substituted by the function A_z and A_r, or B_z and B_r. It is worth remarking that the dispersion obtained in a Cartesian mesh, given by Eqs. 2.145 or 2.143 for the TM-node or SCN, respectively, is really identical to that got in Eq. 4.19.

Although in some studies the Lorentz model [37] has been employed for the permeability, other contributions dealing with left handed metamaterials [44] or cloaking [82], do use the Drude's model. It is worth emphasizing that the Drude's model employed here does not alter any conclusions we will obtain from the numerical simulation.

Let us suppose that the plane wave has a TM polarization. The optic constants of interest in Eq. 4.6 are μ_z, ε_r, and ε_φ, which are related to the admittances/impedances of the stubs Z_z, Y_r, and Y_φ; respectively. These last values are

given by Eq. 2.121, and have to be multiplied by the factor $-\frac{1}{4}\Delta t^2\omega^2$ if they are less than one, as pointed out in section 2.5. On the one hand, Z_z, Y_r, and Y_φ are ω-dependent only if they were previously less than unity. On the other hand and even if only free space is rigourously non-dispersive, the dispersion for an usual material can be neglected in a certain bandwidth. This approximation is particularly justifiable when compared to metamaterials which are highly dispersive media. Accordingly, in the TLM procedure, a metamaterial should be characterized by a negative Z_z, Y_r, or Y_φ if μ_z, ε_r, or ε_φ, respectively, is less than one. Since an example is worth a thousand words, let us focus on μ_z. If μ_z is less than one, the associated Z_z has to be negative, and has then to be multiplied by the factor $-\frac{1}{4}\Delta t^2\omega^2$. Otherwise, if a positive Z_z were associated with μ_z less than one, the simulated material would not be dispersive. On the contrary, if μ_z is greater than one, the associated Z_z has to be positive. Otherwise, its relation of dispersion would follow a Drude's model which is unlikely for a usual material.

Since the constitutive parameters of the cloak can be usual in a certain region while being of exotic nature in another one, the greatest heed has to be given to the previous paragraph. In the following, we wish to examine the consequence of such requirements.

1. **Consequence of the distribution of $\mu_z(r)$.**
   Together, Eqs. 4.6c and 2.121c lead to

$$Z_z = \frac{2\mu_0}{Z_0\Delta t}\frac{\Delta r\Delta\varphi}{\Delta z}\left(\frac{R_2}{R_2-R_1}\right)^2(r-R_1)-4. \tag{4.20}$$

   Thus, Z_z is a straight line whose slope is strictly positive. Moreover,

$$\mu_z(r)=1 \Rightarrow r=\frac{R_2^2}{2R_2-R_1} \tag{4.21}$$

   indicating that

$$\begin{cases} \text{if } r \geq \frac{R_2^2}{2R_2-R_1} \Rightarrow \mu_z(r)\geq 1, & \text{then } Z_z \text{ must be positive,} \\ \text{if } r \leq \frac{R_2^2}{2R_2-R_1} \Rightarrow \mu_z(r)\leq 1, & \text{then } Z_z \text{ must be negative.} \end{cases} \tag{4.22}$$

   Given that Z_z is a monotonic continuous function of r,

$$r=\frac{R_2^2}{2R_2-R_1} \Rightarrow Z_z=0, \tag{4.23}$$

which implies

$$\Delta t = \frac{\mu_0 R_2^2 \Delta r \Delta \varphi}{2Z_0(2R_2 - R_1)\Delta z}. \tag{4.24}$$

To summarize, Eq. 4.22 imposes a condition on the TLM time-step that is thus given by Eq. 4.24.

2. **Consequence of the distribution of $\varepsilon_\varphi(r)$.**
The φ-component of the permittivity of the cloak given in Eq. 4.6b is a monotonically decreasing function that is always greater than one. Consequently Y_φ must be positive for all r into the cloak, and we must prevent Y_φ to become negative. Usually, the cloak will be immerse in vacuum. In this case, the φ-component of the permittivity of the cloak is greater than that of the host media for all r. According to Eq. 2.121b, this means that Y_φ reaches its smallest value, i.e., the least favorable situation, at the outer boundary, $r = R_3$, of the TLM mesh where the permittivity is equal to one. Accordingly, the condition becomes

$$\frac{2\varepsilon_0}{Y_0 \Delta t}\frac{\Delta r \Delta z}{R_3 \Delta \varphi} - 2 \geq 0, \tag{4.25}$$

which implies

$$\Delta t \leq \frac{\varepsilon_0 \Delta r \Delta z}{Y_0 R_3 \Delta \varphi} = \Delta t_2. \tag{4.26}$$

3. **Consequence of the distribution of $\varepsilon_r(r)$.**
Y_r is given by Eq. 2.121a. Furthermore, Eq. 4.6a indicates that the r-component of the permittivity of the cloak is a monotonically increasing function that is always less than unity. Thus, Y_r has to be such that $Y_r \leq 0$ inside the cloak, i.e., if $r \leq R_2$. In this case,

$$Y_r = \frac{2\varepsilon_0}{Y_0 \Delta t}\frac{\Delta \varphi \Delta z}{\Delta r}(r - R_1) - 2. \tag{4.27}$$

Hence,

$$r \leq R_2 \Rightarrow \Delta t \geq \frac{\varepsilon_0 (r - R_1)\Delta \varphi \Delta z}{Y_0 \Delta r}, \tag{4.28}$$

from which it is plain that the greatest value of Δt is reached at $r = R_2$, which fix the condition:

$$\Delta t \geq \frac{\varepsilon_0 (R_2 - R_1)\Delta \varphi \Delta z}{Y_0 \Delta r} = \Delta t_3. \tag{4.29}$$

In the same manner, assuming that the host medium is vacuum, we have to ensure that $Y_r \geq 0$ outside the cloak, i.e., if $r \geq R_2$. In this case we have

$$Y_r = \frac{2\varepsilon_0}{Y_0 \Delta t} \frac{r \Delta\varphi \Delta z}{\Delta r} - 2, \tag{4.30}$$

and hence,

$$r \geq R_2 \Rightarrow \Delta t \leq \frac{\varepsilon_0 r \Delta\varphi \Delta z}{Y_0 \Delta r}. \tag{4.31}$$

The least favorable case occurring at $r = R_2$, we get

$$\Delta t \leq \frac{\varepsilon_0 R_2 \Delta\varphi \Delta z}{Y_0 \Delta r} = \Delta t_4. \tag{4.32}$$

Eqs. 4.24, 4.26, 4.29, and 4.32 form a set of four conditions on Δt that involves four quantities we have referred to as Δt, Δt_2, Δt_3, and Δt_4. These quantities depend on the parameters of the TLM node (Δr, $\Delta\varphi$, Δz, and $Z_0 = 1/Y_0$), the physical system we are modeling (R_1 and R_2), the size of the mesh (R_3), the permittivity and permeability of free space (ε_0 and μ_0). These quantities are enforced by Eqs. 4.24, 4.26, 4.29, and 4.32; but the fact that they are all interlinked in the set of equations makes difficult the task of drawing a general rule for the values that are allowed. However a discussion is proposed in the following.

- The value of Δt must be chosen accordingly to Eq. 4.24.
- It is plain from Eqs. 4.26 and 4.29 that Δt_2 must be greater than Δt_3. This provides the requisite:

$$R_3 \leq (\frac{\Delta r}{\Delta\varphi})^2 \frac{1}{R_2 - R_1}, \tag{4.33}$$

  which is a necessary but not sufficient condition. Even if Eq. 4.33 is fulfilled, the completion of Eqs. 4.26 and 4.29 should be verified.
- Another conclusion to be drawn is in regard to the authorized values for Δz. We are dealing with a 2D case, therefore Δz is apparently a degree of freedom as long as the TLM fundamental condition $\Delta z \leq \frac{\lambda}{10}$ is met,λ being the wavelength. However, Eqs. 4.26, 4.29, and 4.32 have to be fulfilled, which is of significant consequence on Δz. Δt being fixed by Eq. 4.24, Eq.

4.26 can be written as

$$\Delta z \geq \frac{\eta_0}{\sqrt{2}Z_0}\frac{\Delta\varphi R_2\sqrt{R_3}}{\sqrt{2R_2-R_1}}, \tag{4.34}$$

Eq. 4.29 provides

$$\Delta z \leq \frac{\eta_0}{\sqrt{2}Z_0}\frac{\Delta r R_2}{\sqrt{2R_2-R_1}\sqrt{R_2-R_1}}, \tag{4.35}$$

while Eq. 4.32 leads to

$$\Delta z \geq \frac{\eta_0}{\sqrt{2}Z_0}\frac{\Delta r\sqrt{R_2}}{\sqrt{2R_2-R_1}}. \tag{4.36}$$

As shown in section 2.6, the dispersion generated by the TLM mesh is given here by Eqs. 3.12a and 2.150. If we take into account Eq. 4.24, the former equation becomes

$$A_z = \frac{R_2^2}{2R_2-R_1}\frac{1}{r} = \frac{R_l}{r}, \tag{4.37a}$$

$$A_r = \frac{\eta_0^2}{2Z_0^2}\left(\frac{\Delta r}{\Delta z}\right)^2\frac{R_2^2}{2R_2-R_1}\frac{1}{r}. \tag{4.37b}$$

Note that A_φ is not involved given that ε_φ can be considered as non-dispersive. Since A_z and A_r depend on parameters of the numerical simulation, we will have to ensure that $\widetilde{\mu}_z(\omega)$ and $\widetilde{\varepsilon}_r(\omega)$ be in agreement with the causality condition

$$\partial(\omega\widetilde{\chi}(\omega))/\partial\omega \geq 1, \tag{4.38}$$

where $\widetilde{\chi}$ represents either $\widetilde{\mu}_z(\omega)$ or $\widetilde{\varepsilon}_r(\omega)$. This condition can be derived from the Kramers-Kronig relations, which are a direct consequence of the causality principle [90]. Note that Yaghjian showed that considerations involving electromagnetic energy conservation are capable of providing the same inequality, but he moreover proved that the relation

$$\partial(\omega\widetilde{\chi}(\omega))/\partial\omega \geq \widetilde{\chi}(\omega)^2 \tag{4.39}$$

should be employed for diamagnetic metamaterials [91]. Metamaterials consisting of open or closed split-ring resonators exhibit a strong diamagnetic re-

sponse [92]. So the causality conditions used here are:

$$\frac{\partial \omega \widetilde{\mu}_z(\omega)}{\partial \omega} - \widetilde{\mu}_z(\omega)^2 \geq 0, \tag{4.40a}$$

$$\frac{\partial \omega \widetilde{\varepsilon}_r(\omega)}{\partial \omega} - 1 \geq 0. \tag{4.40b}$$

First, let us consider the condition on $\widetilde{\mu}_z(\omega)$. Using Eqs. 4.6 and 4.37, Eq. 2.150 becomes

$$\widetilde{\mu}_z(\omega) = \frac{R_l}{r} - \frac{\omega_0^2}{\omega^2}[\frac{R_l}{r} - (\frac{R_2}{R_2 - R_1})^2 \frac{r - R_1}{r}]. \tag{4.41}$$

Detailed calculations provide that the related causality condition, expressed in Eq. 4.40a, is completed when $r \leq R_l$. Since μ_z has to be dispersive only for $r \leq R_l$ (beyond R_l the permeability is greater than one), the causality condition is perfectly fulfilled. It is worth noting that the Eq. 4.38 condition, which will be applied to the permittivity, turns out to give exactly the same result.

Second, let us consider the condition on $\widetilde{\varepsilon}_r(\omega)$. Focusing on Eq. 4.37, let γ be the quantity $\frac{\eta_0^2}{2Z_0^2}(\frac{\Delta r}{\Delta z})^2 \frac{R_2^2}{2R_2 - R_1}$ so that $A_r = \frac{\gamma}{r}$. We get

$$\widetilde{\varepsilon}_r(\omega) = \frac{\gamma}{r} - \frac{\omega_0^2}{\omega^2}[\frac{\gamma}{r} - \frac{r - R_1}{r}]. \tag{4.42}$$

The causality condition expressed in Eq. 4.40b turns out to yield

$$\begin{aligned} & r \leq \gamma + \frac{R_1}{(\frac{\omega}{\omega_0})^2 + 1}, \\ \Leftrightarrow \quad & \gamma \geq r - \frac{R_1}{(\frac{\omega}{\omega_0})^2 + 1}, \\ \Rightarrow \quad & \gamma \geq R_2 - \frac{R_1}{(\frac{\omega}{\omega_0})^2 + 1}. \end{aligned} \tag{4.43}$$

If $(\frac{\omega}{\omega_0})^2 \ll 1$, this condition becomes $\gamma \geq (R_2 - R_1)$, while it becomes $\gamma \geq R_2$ if $(\frac{\omega}{\omega_0})^2 \gg 1$. The most restrictive condition should be conserved; therefore, we can conclude that the causality condition imposes $\gamma \geq R_2$, which is equivalent to the expression

$$\Delta z \leq \frac{\eta_0}{\sqrt{2} Z_0} \frac{\Delta r \sqrt{R_2}}{\sqrt{2R_2 - R_1}}. \tag{4.44}$$

This causality condition must be coherent with Eq. 4.36. As a result, Δz is fixed by the causality condition and must be equal to

$$\Delta z = \frac{\eta_0}{\sqrt{2}Z_0}\Delta r\sqrt{\frac{R_2}{2R_2 - R_1}}, \tag{4.45}$$

or, equivalently,

$$\gamma = R_2. \tag{4.46}$$

From Eq. 4.42, we get the final form for the dispersive permittivity originated by the TLM mesh:

$$\widetilde{\varepsilon}_r(\omega) = \frac{R_2}{r} - \frac{\omega_0^2}{\omega^2}[\frac{R_2}{r} - \frac{r - R_1}{r}]. \tag{4.47}$$

As well, the causality condition has to be coherent with Eq. 4.34. That leads to

$$R_3 \leq (\frac{\Delta r}{\Delta\varphi})^2 \frac{1}{R_2}, \tag{4.48}$$

which is a more restrictive condition than the condition expressed by Eq. 4.33. In section 4.6.1, $R_1 = 0.1$ m and $R_2 = 0.2$ m, while the dimensions of the node were $\Delta r = (R_2 - R_1)/200 = 0.5$ mm and $\Delta\varphi = 2\pi/2520 \simeq 2.5$ mm. As a result, Eq. 4.48 becomes $R_3 \lesssim R_2$ which is impossible since R_3 represents the outer boundary of the mesh: the cloak proposed in section 4.6.1 was not causal, which was of no consequence in the corresponding results given that the plane wave was monochromatic. If the plane is non-monochromatic, Δr has to be increased (giving rise to less precision) or $\Delta\varphi$ has to be decreased (giving rise to more precision) in order to enhance the allowed maximum value for R_3.

For the purpsose of illustration, we plot $\widetilde{\mu}_z(\omega/2\pi)$ (given in Eq. 4.41) and $\widetilde{\varepsilon}_r(\omega/2\pi)$ (given in Eq. 4.47) for $r = R_1$ and R_l in Fig. 4.13.

4.7.2 Frequency-shift phenomenon

It has been theoretically shown that the frequency center of a quasimonochromatic wave is blueshifted in the forward direction after passing through a spherical cloak [88]. We propose in this section to study what happens for a cylindrical cloak illuminated by a quasimonochromatic plane wave. By quasimonochromatic, we mean that the wave is no longer monochromatic but the frequency bandwidth has to be however small enough to prevent the cloaking effect, which is strictly achievable only at the single working frequency, to totally disappear.

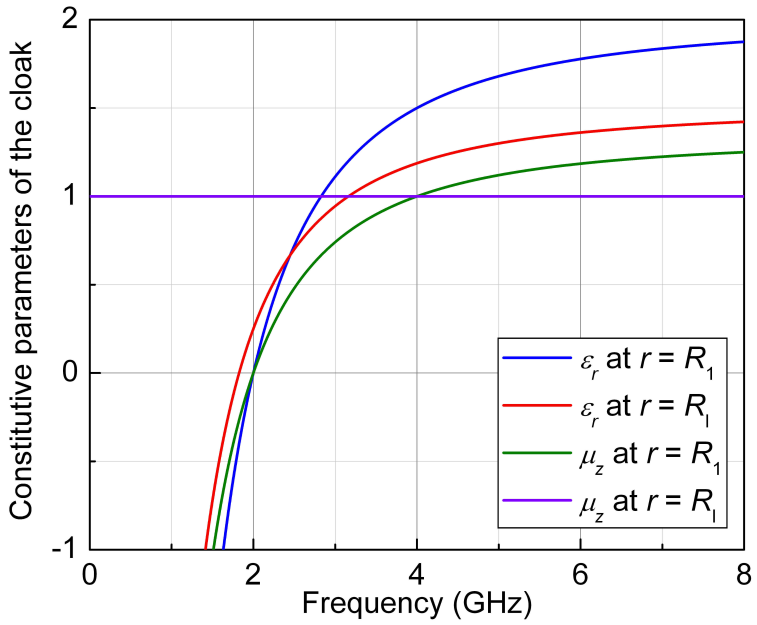

Figure 4.13: Cloak's constitutive parameters, μ_z and ε_r, in terms of the frequency, for $r = R_1$ and $r = R_l$. $R_1 = 0.1$ m, $R_2 = 0.2$ m, and the working angular frequency is $\omega_0 = 2\pi.2$ GHz.

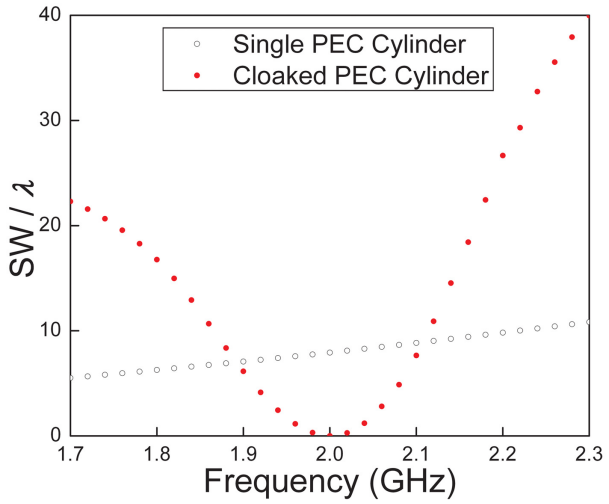

Figure 4.14: Scattering width of a PEC cylinder with/without the cloaking shell around along the forward direction. The scattering is reduced in a narrow-band around the 2 GHz working frequency.

Let us consider a PEC cylinder surrounded by a dispersive cloaking shell whose functional frequency is $f_0 = 2$ GHz. The parameters of the modeling are in agreement with section 4.7.1; accordingly, the constitutive parameters of the cloak are ω-dependent and follow Eqs. 4.41 and 4.47. The structure is illuminated by a TM wave. In order to exactly see how the cloaking effectiveness is affected by a deviation on the frequency, we first compute the scattering width of the cloaked PEC cylinder in terms of the frequency. Numerically, the process consists of using a Gaussian pulse, then calculating the radiated far-field, and finally operating a Fourier Transform to get the frequency domain representation. The result in the forward direction is depicted in Fig. 4.14 and compared with the scattering width of a simple PEC cylinder. As expected, the cloak is effective only for f_0, the working frequency. However, the scattering width is obviously very low in a certain bandwidth centered on f_0 and for which the object is still undetectable. The size of such a bandwidth depends on the sensitivity of the detector located outside the structure.

For a time domain method as TLM, a quasimonochromatic electromagnetic wave can be modeled by using a modulated sinusoid in terms of time, t, such that

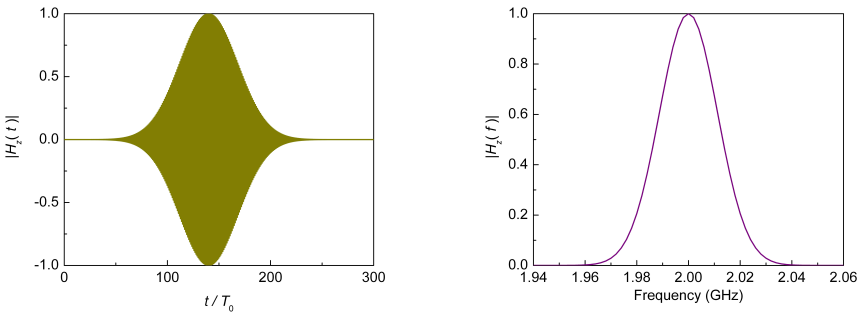

(a) (b)

Figure 4.15: **(a)** Frequency domain representation of the incoming wave for $\omega = 2\pi.2$ GHz and $g = 5.10^7 s^{-1}$. So highly does $H_z(t)$ oscillate that the distribution of points totally obscure the area within the envelop, but it should be kept in mind that $H_z(t)$ is a sinusoid signal. **(b)** Frequency domain representation of the incoming wave.

the incoming magnetic field H_z is given by:

$$H_z(t) = \frac{\sin(\omega t)\exp[-g^2(t-t_m)^2]}{\eta_0} \tag{4.49}$$

where g and t_m are two real numbers that define the bandwidth of the signal. $H_z(t)$ is plotted in Fig. 4.15(a). In the frequency domain, such an incoming wave behaves as a quasimonochromatic wave, as shown in Fig. 4.15(b) in which the Fourier Transform of $H_z(t)$ is depicted. Indeed, the frequency domain representation of the original function is a Gaussian pulse centered on ω. The quasimonochromatic nature of the wave is controlled by the parameter g: the smaller the g constant, the narrower the pulse in the frequency domain. Therefore, if g is chosen to be small enough, any scattering due to the dispersion inherent to the cloak is minimized around the cloaking frequency; and the frequency domain representation of the wave that passes through the cloak, i.e., the transmitted wave, should be a Gaussian too. In this example, the bandwidth of the signal has been selected to be $g = 5.10^7 s^{-1}$, and it turns out that the whole frequency domain plot of Fig. 4.15(b) may be considered as contained in the domain of undetectability of the cloak. This affirmation can be staten referring to Fig. 4.14 in which it is observed that the radiation of the bare cylinder was significantly reduced in the range from 1.96 to 2.04 GHz. Consequently, the quasimonochromatic plane

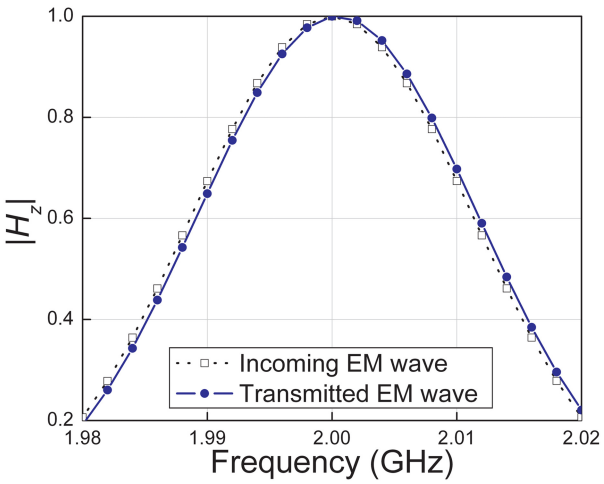

Figure 4.16: The *black dotted line* is the Fourier Transform of the incident wave, which is the curve already plotted in Fig. 4.15(a). The *blue solid line* is the frequency domain representation of the transmitted wave in the forward direction. The frequency center of the latter signal is blueshifted compared to the former signal.

wave displayed in Fig. 4.15 will be used in the numerical determination of the frequency-shift that follows.

While a strictly monochromatic wave would pass the cloak strictly unaltered, the situation might slightly change for a quasimonochromatic wave even if the bandwidth is narrow as it is the case here. First, let us examine what is happening in the forward direction. The H-field is computed at a distance λ_0 (incoming radiation wavelength) from the outer boundary of the cloak. The corresponding frequency domain representation, obtained by Fourier Transform, is displayed in Fig. 4.16 (blue solid line). The frequency center of the new pulse is shifted towards a higher frequency, which corresponds to a blueshift of the wavelength. Concretely, it turns out that the frequency center of the pulse has been shifted by 0.6 MHz. We now numerically calculate the frequency shift along other directions; the result is depicted in Fig. 4.17. The shift continuously spans a large spectrum, going from negative values to positive values. The corresponding redshift occurs around 40°. Note that such a redshift was expected since the energy has to be conserved. In conclusion, an observer looking at an object through a cloak will see the object with a frequency-shift; moreover, the amplitude of the frequency-shift depends on the position from where the object is observed.

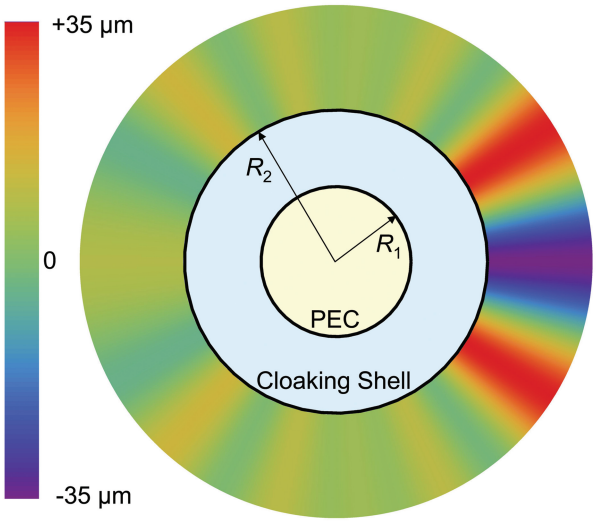

Figure 4.17: Distribution of the shifted frequency center in terms of the observation angle for a quasimonochromatic EM wave traveling from left to right.

4.7.3 Time-delay phenomenon

Because the EM constants of the cloak are r-dependent, the wave velocity is expected to follow a certain distribution: Chen has shown that velocity decreases when getting closer to the inner boundary of the invisible shell for a spherical cloak [74]. What about the cylindrical cloak?

Let us consider a TM wave incident upon a dispersive cylindrical cloak, the incoming magnetic and electric field can be expressed as:

$$H_z^{inc}(r) = H_0 \exp[j\frac{\omega}{c} r\cos\varphi], \tag{4.50a}$$

$$E_r^{inc}(r) = E_0 \exp[j\frac{\omega}{c} r\cos\varphi]\sin\varphi, \tag{4.50b}$$

$$E_\varphi^{inc}(r) = E_0 \exp[j\frac{\omega}{c} r\cos\varphi]\cos\varphi, \tag{4.50c}$$

from which we can derive the electromagnetic field in the cloak using the equations [91],

$$H_z = H_z^{inc}[f(r)], \tag{4.51a}$$

$$E_r = f'(r)E_r^{inc}[f(r)], \tag{4.51b}$$

$$E_\varphi = \frac{f(r)}{r} E_\varphi^{inc}[f(r)], \tag{4.51c}$$

where $f(r)$ is the transformation function in Eq. 4.3. Calculations give:

$$H_z = H_0 \exp[i\frac{\omega}{c}\frac{R_2}{R_2-R_1}(r-R_1)\cos\varphi], \tag{4.52a}$$

$$E_r = E_0 \frac{R_2}{R_2-R_1} \exp[i\frac{\omega}{c}\frac{R_2}{R_2-R_1}(r-R_1)\cos\varphi]\sin\varphi, \tag{4.52b}$$

$$E_\varphi = E_0 \frac{R_2}{R_2-R_1}\frac{r-R_1}{r} \exp[i\frac{\omega}{c}\frac{R_2}{R_2-R_1}(r-R_1)\cos\varphi]\cos\varphi. \tag{4.52c}$$

The total electromagnetic energy density can be written as [90]:

$$\overline{W} = \frac{1}{4}[\varepsilon_0 \frac{\partial(\omega\varepsilon)}{\partial\omega} EE^* + \mu_0 \frac{\partial(\omega\mu)}{\partial\omega} HH^*]. \tag{4.53}$$

For an anisotropic medium, this equation becomes

$$\begin{aligned}\overline{W} &= \frac{1}{4}[\varepsilon_0 \frac{\partial(\omega\varepsilon_{ik})}{\partial\omega} E_i E_k^* + \mu_0 \frac{\partial(\omega\mu_{ik})}{\partial\omega} H_i H_k^*] \\ &= \frac{1}{4}[\varepsilon_0 \frac{\partial(\omega\varepsilon_r)}{\partial\omega} E_r E_r^* + \varepsilon_0 \frac{\partial(\omega\varepsilon_\varphi)}{\partial\omega} E_\varphi E_\varphi^* + \mu_0 \frac{\partial(\omega\mu_z)}{\partial\omega} H_z H_z^*].\end{aligned} \tag{4.54}$$

From Eq. 4.52, we get

$$\begin{aligned}\overline{W} = \frac{1}{4}[&\varepsilon_0 \frac{\partial(\omega\varepsilon_r)}{\partial\omega} \frac{E_0^2 R_2^2}{(R_2-R_1)^2}\sin^2\varphi \\ &+\varepsilon_0 \frac{\partial(\omega\varepsilon_\varphi)}{\partial\omega} \frac{E_0^2 R_2^2}{(R_2-R_1)^2}(\frac{r-R_1}{r^2})^2\cos^2\varphi \\ &+\mu_0 H_0^2 \frac{\partial(\omega\mu_z)}{\partial\omega}].\end{aligned} \tag{4.55}$$

Tthe time-average Poynting vector over one period, see [80] (pages 28-29), is equal to

$$\overline{S} = \frac{1}{2}\Re[E \times H^*], \tag{4.56}$$

which leads to

$$|\overline{S}| = \frac{1}{2}\frac{E_0 H_0 R_2}{R_2-R_1}[\sin^2\varphi + (\frac{r-R_1}{r^2})^2\cos^2\varphi]^{1/2}. \tag{4.57}$$

From Eqs. 4.55 and 4.57, we can get the velocity using the formula [90]

$$u = \frac{|\overline{S}|}{\overline{W}}; \tag{4.58}$$

the calculation gives:

$$u = c\frac{2R_2\sqrt{(\frac{r-R_1}{r})^2\cos^2\varphi+\sin^2\varphi}}{(R_2-R_1)[(\frac{R_2\sin\varphi}{R_2-R_1})^2\frac{\partial(\omega\varepsilon_r)}{\partial\omega}+(\frac{r-R_1}{r}\frac{R_2\cos\varphi}{R_2-R_1})^2\frac{\partial(\omega\varepsilon_\varphi)}{\partial\omega}+\frac{\partial(\omega mu_z)}{\partial\omega}]}, \tag{4.59}$$

where c is the speed of light in free-space.

In agreement with Eqs. 4.41 and 4.47,

$$\begin{aligned}
\mu_z(\omega) &= \begin{cases} \frac{R_l}{r}-\frac{\omega_0^2}{\omega^2}[\frac{R_l}{r}-(\frac{R_2}{R_2-R_1})^2\frac{r-R_1}{r}] & \text{if } r\le R_l \\ (\frac{R_2}{R_2-R_1})^2\frac{r-R_1}{r} & \text{if } r>R_l, \end{cases} \\
\varepsilon_r(\omega) &= \frac{R_2}{r}-\frac{\omega_0^2}{\omega^2}[\frac{R_2}{r}-\frac{r-R_1}{r}] \qquad \forall r, \\
\varepsilon_\varphi(\omega) &= \frac{r}{r-R_1} \qquad \forall r.
\end{aligned} \tag{4.60}$$

For the purpose of illustration, the distribution of the permeability μ_z is shown in Fig. 4.18 for $\omega = \omega_0$ and $\omega = 1.2\omega_0$. The velocity distribution, given in Eq. 4.59, in a dispersive cloak whose constitutive parameters follow Eq. 4.60 can be plotted. The result is shown in Fig. 4.19(a). Furthermore, the velocity in terms of the radius of the cloak is plotted for $\varphi = 0^o$ and 90^o in Fig. 4.19(b). It is plain from Fig. 4.19(b) that the velocity is smaller near the inner boundary of the cloak. Thus, once the EM wave has passed through the cloak, the process of reaching different points located on a plane normal to the direction of propagation should be completed with a time delay. This phenomenon can be illustrated using a ray-tracing simulation, but this treatment is unable to take into account material effects that might affect the solution. Moreover, on-axis ray problems make the obtained results incomplete. On the contrary, a full wave time-domain simulation constitutes a deeper evidence of the time-delay effect.

Such a time-delay cannot be computed if the incoming wave is monochromatic, i.e., modeled by a simple sinusoid: the incident and the transmitted signal would overlap (the cloaking effect is perfect at the corresponding frequency) making impossible the distinction between each other. Instead using a quasimonochro-

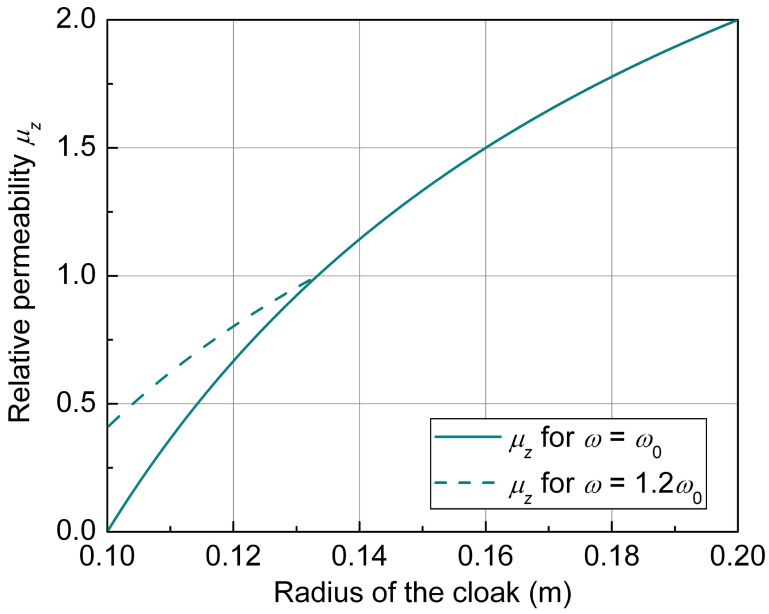

Figure 4.18: Distribution of the permeability $\mu_z(r)$ for $\omega = \omega_0$ and $\omega = 1.2\omega_0$. Since $\mu_z(r)$ is dispersive from R_1 to R_l, the curves diverge in this range before converging at $r = R_l$.

matic incoming wave, modeled using the modulated sinusoid of Eq. 4.49, makes possible the distinction thanks to the envelop of the signal. It is worth noting that the frequency representation of the quasimonochromatic wave has to be narrow enough in order to avoid distortion due to the dispersion. In other word, using a purely gaussian excitation would be of no interest, it would give rise to a wild bandwidth that would destroy the cloaking effect.

Let the cloaking frequency be $f_0 = 6$ GHz. The H-field is calculated in the forward direction at the distance $x_0 = \lambda_0$ from the cloak outer boundary. In Fig. 4.20, we compare the H-field in the absence and in the presence of the whole structure in terms of time, normalized by the period of the incident wave, $T_0 = 1/f_0$. Obviously, if the envelope of the signal is considered, the presence of the cloak results in the EM wave to reach x_0 with a time delay. Since the wave frequency is high, oscillations resulting from the sine in Eq. 4.49 cannot be observed; that is why we have enlarged a certain portion of Fig. 4.20, where it can be seen that the transmitted wave propagates with the same phase as the incident one. This result was expected since the wave is required to arrive on the far side of the cloak with the same phase in order to have the cloaking effect achieved. Moreover, it confirms

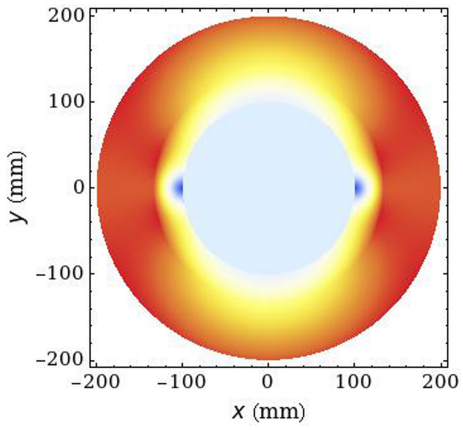

(a)

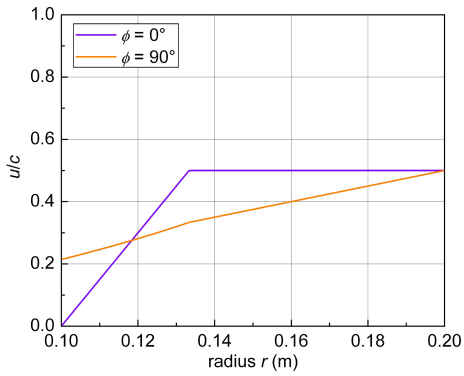

(b)

Figure 4.19: **(a)** Velocity distribution within the cloaking shell. The velocity tends to decrease when getting closer to the inner boundary of the cloak. There are two regions in which the velocity is particularly low: in the vicinity of $r = R_1$ for 0^o and 180^o. **(b)** The velocity distribution is plotted along the backward direction (0^o) and along the 90^o-direction. The low value of the velocity, noticed in (a), is particularly apparent.

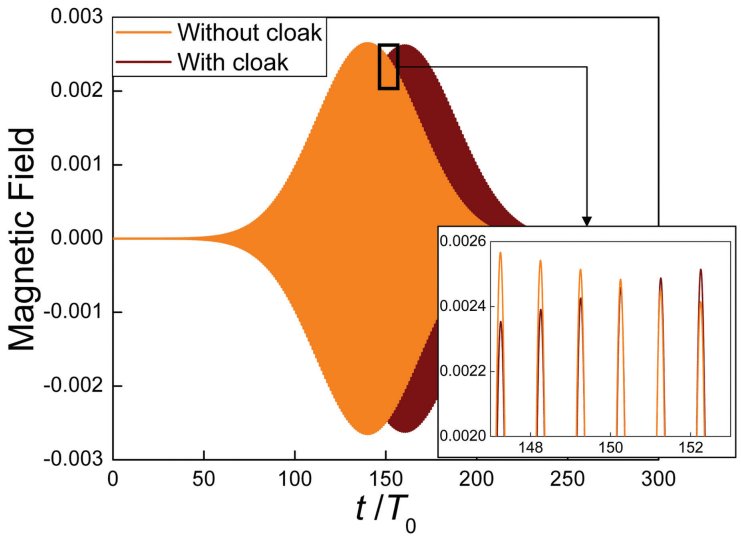

Figure 4.20: H-field plot in terms of the normalized time. The envelope of the signal does not reach x_0 at the same time depending on whether the cloaking structure is present or not. On the other hand, the phase is unchanged in agreement with the cloaking effect requirement.

the correctness and accurateness of our numerical simulation.

As previously mentioned, the time delay is a consequence of the dependence in terms of r of the cloak's parameters. Therefore, it is interesting to study the response of cloaking devices based on non-linear coordinate transformations, i.e., with values of α not equal to unity in Eq. 4.4. In this case, the permittivity and permeability of the cloak is given by Eq. 4.14. Because of the modification of the constitutive parameters of the cloak, the analysis carried out in section 4.7.1 must be accordingly modified if $\alpha \neq 1$. With this new definition:

- ε_r is still an increasing function. It is less than unity if we ensure that $\alpha \leq \frac{R_2}{R_2 - R_1}$, which is a fulfilled condition given that $\alpha \in]0,1]$.
- ε_φ is still a decreasing function. It is greater than unity since $\alpha \leq \frac{R_2}{R_2 - R_1}$.
- μ_z is a continuous function with positive slope. On the one hand $\mu_z(R_1) = 0$, on the other hand $\mu_z(R_2) > 1$; according to the intermediate value theorem, there is a real number R_n such that $\mu_z(R_n) = 1$. If $\alpha = 1$, R_n is what we referred to as R_l in section 4.7.1.

Obviously, Eqs. 4.32 and 4.26 are unchanged. On the other hand, Eq. 4.29 must be modified, the new condition is:

$$\Delta t \geq \frac{\alpha \varepsilon_0 (R_2 - R_1) \Delta\varphi \Delta z}{Y_0 \Delta r}. \tag{4.61}$$

Finally, the expression of Δt (given by Eq. 4.24 in section 4.7.1) is derived from the equality $Z_z(R_n) = 0$, which implies

$$\Delta t = \frac{\mu_0 R_2^2 \Delta r \Delta\varphi (R_2 - R_1)^{-\frac{2}{\alpha}} (R_n - R_1)^{\frac{2}{\alpha}-1}}{2\alpha Z_0 \Delta z}. \tag{4.62}$$

The causality condition that was given in Eq. 4.40 must be taken into account. Furthermore, let γ_z be the quantity such that $\gamma_z = \frac{2\Delta t \Delta z Z_0}{\Delta r \Delta\varphi \mu_0}$, and let γ_r be the quantity such that $\gamma_r = \frac{\Delta t \Delta r Y_0}{\Delta\varphi \Delta z \varepsilon_0}$. Accordingly,

$$\widetilde{\mu}_r(\omega) = \frac{\gamma_z}{r} - \frac{\omega_0^2}{\omega^2}\left[\frac{\gamma_z}{r} - \mu_z(\omega_0)\right], \tag{4.63a}$$

$$\widetilde{\varepsilon}_r(\omega) = \frac{\gamma_r}{r} - \frac{\omega_0^2}{\omega^2}\left[\frac{\gamma_r}{r} - \varepsilon_r(\omega_0)\right], \tag{4.63b}$$

where $\mu_z(\omega_0)$ and $\varepsilon_r(\omega_0)$ are given by Eq. 4.14. Calculations give that the causality condition on $\widetilde{\varepsilon}_r$ is fulfilled if

$$\gamma_r \geq \frac{r(\omega^2 + \alpha\omega_0^2)}{\omega^2 + \omega_0^2} - \frac{R_1 \alpha \omega_0^2}{\omega^2 + \omega_0^2}. \tag{4.64}$$

Consequently, as it was the case in section 4.7.1, the choice $\gamma_r \geq R_2$ should be done given that it ensures that the cloak is causal in a large frequency band. However, Eq. 4.32 can be written as $\gamma_r \leq R_2$. Therefore γ_r must be such that

$$\gamma_r = R_2. \tag{4.65}$$

Let Π^2 be the plane normal to the x-axis at point x_0. Let t_{td} be the deviation between the required time for the EM wave to reach Π^2 with and without the presence of the whole structure. Let us consider the line, contained in Π^2, that points along the y-direction. Depending on the position of the point under consideration, t_{td} is expected to take different values. In the following, we propose to compute t_{td} (normalized by T_0) in terms of the distance y from the x-axis. In order to calculate t_{td}, we look at the EM power associated with the signal. We first calculate the

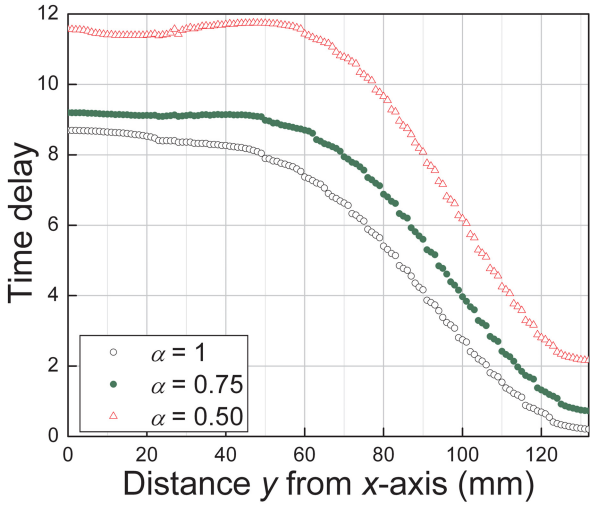

Figure 4.21: (Color online) Time-delay (normalized by T_0) in terms of the distance y form the x-axis for non-linear coordinate transformations

total power, P_0, of the incident wave. Then, we admit that the required time for the transmitted wave to reach Π^2 is attained when the power $P_0/2$ has flowed through Π^2. The result is depicted in Fig. 4.21 for α = 1, 0.75, and 0.5. As expected, t_{td} decreases when deviating from the x-axis. Furthermore, the time delay is plainly sensitive to the type of transformation, the linear one rendering the delay smaller.

For completion's sake, we have tried other frequencies for the incoming wave. The obtained curves turn out to be different from the ones presented in Fig. 4.21. The reason is that the phenomenon mainly comes from diffraction, thus the time delay depends on the size of the cloak or, equivalently, on the frequency of the incident wave.

4.8 Anticloak

An issue of great concern to physicists is whether the cloaking effect can be achieved under any condition. In this sense, it has been shown that the ideal 2D cloak is very sensitive to the slightest perturbation [72]. Still for the cylindrical case, it has been established that extending the inner boundary of the cloaking shell toward the concealed region appears to allow further penetration of the field [73]. Nonetheless, since the power cannot go into the cloak, the effectiveness of the cloaking was not questioned in [73]. It should be emphasized that [72, 73]

clearly stressed the fundamental role of the extreme inner layer, for which the azimuth permittivity or permeability (depending on the electromagnetic polarization under consideration) are infinite while the other electromagnetic parameters are zero. Furthermore, it has been more recently proven that a certain kind of anisotropic material located beyond the inner boundary of the cloak can cancel out the cloaking effect [75, 93]. The permittivity, ε, and permeability, μ, of such an anticloak are derived using a coordinate transformation whose slope is negative compared to the original one; the electromagnetic space associated with the cloak is then reconstructed by the anticloak, rendering visible the object inside the anticloak [75]. It is interesting to note that there are two sets of solutions to Maxwell's equations in this case. One dictates that the field cannot penetrate into the cloak irrespective of what is inside [72,73], while the other shows that the field can penetrate into the cloaked region by virtue of the anticloak [75]. However, it is arduous to verify this extreme case for which both the cloak and anticloak exist and interact with each other. The analytic calculations in [72, 73] did not consider the possibility of including such an anisotropic anticloak, while [75] used a nonzero perturbation parameter that approaches the ideal case without rigorously reaching it. Therefore, the ideal situation requires further analysis, as mentioned in [75], but dealing with extreme parameters is challenging from both the analytical and computational point of view. Mathematically, when the perturbation parameter goes to zero, the transformation becomes a singular mapping and the Jacobian matrix does not exist at the interface between the cloak and the anticloak. For this reason, cloaking modeling usually assume upper and lower limits of the constitutive parameters while the required, ε or μ span the entire range from zero to infinity.

In the present section, the singular behavior of the anticloak is studied using TLM. We will show that when the perturbation parameter is nonzero, the anticloak can cancel the cloaking effect outside. However, when it is zero, the presence of an extreme layer between the cloak and anticloak ensures that the cloaking effect is still achieved, irrespective of the core composition. Third, an analytical model is developed to explain this behavior.

We have shown in section 4.2 that, to be effective, the dielectric and magnetic constants of the anisotropic cloak must take the specific values given in Eq. 4.6. In this section, we will extend the development given in this section to make Eq. 4.6 more general. Let the inner and outer radius be represented by R_1 and R_2,

respectively. The simple following transformation,

$$r = (r' - R_2)\frac{R_2 - R_1}{R_2 - c} + R_2, \quad \varphi = \varphi', \quad z = z', \tag{4.66}$$

that can compress the space from $0 < r' < R_2$ to the annular region $a < r < R_2$, yields

$$\varepsilon_r = \mu_r = \frac{r-a}{r}, \tag{4.67a}$$

$$\varepsilon_\varphi = \mu_\varphi = \frac{r}{r-a}, \tag{4.67b}$$

$$\varepsilon_z = \mu_z = (\frac{R_2 - c}{R_2 - R_1})^2 \frac{r-a}{r}, \tag{4.67c}$$

where c is the perturbation parameter, and $a = R_2(R_1 - c)/(R_2 - c)$. The parameter c marks the degree of imperfection of the cloak. In this manner, a zero value of c would make ε or μ ideal, i.e., Eq. 4.67 becomes Eq. 4.6.

Let R_0 be a third boundary inside the cloak in such a way that $0 < R_0 < R_1$. In agreement with [75], the transformation,

$$r = (r' - d)\frac{R_0 - R_1}{d - c} + R_0, \quad \varphi = \varphi', \quad z = z', \tag{4.68}$$

leads to the anticloak parameters:

$$\varepsilon_r = \mu_r = \frac{r-b}{r}, \tag{4.69a}$$

$$\varepsilon_\varphi = \mu_\varphi = \frac{r}{r-b}, \tag{4.69b}$$

$$\varepsilon_z = \mu_z = (\frac{d - c}{R_0 - R_1})^2 \frac{r-b}{r}, \tag{4.69c}$$

where d is a constant, and $b = (R_1 d - R_0 c)/(d - c)$. Chen *et al.* have claimed that the parameters of Eq. 4.69 are capable of destroying the effect of an invisibility cloak when c is nonzero [75], but as it has been pointed out above, the achievement of ideal cloaking actually requires infinite values of μ_φ at $r = R_1$. The difficulty in assuming such an infinite value is often eluded by truncating the inner layer, which leads to large but finite values of μ_φ. Often, substituting the actual infinite values by approximate finite ones is done without significant consequences. For instance, very accurate modeling of the cloaking effect can be reached if μ_φ is chosen to be high enough [70, 72]. However, certain studies may require this quantity

to be actually infinite. It is the case of the anticloaking phenomenon for which no complete study can be carried out without being able to exactly consider an infinite μ_φ. In this sense, TLM is well-suited for the anticloak modeling given that infinite values of μ_φ are of no consequence to the convergence of the method, as it has been shown in section 4.6.1. Thus, compared to Chen *et al*'s paper, our work differs from theirs in one important respect: we will consider the case in which c is strictly equal to zero, i.e., $(\varepsilon_\varphi, \mu_\varphi) = +\infty$ in the cloak and $(\varepsilon_\varphi, \mu_\varphi) = -\infty$ in the anticloak, at $r = R_1$.

Let us consider a cylindrical cloaking structure surrounded by free space and illuminated by a monochromatic TE electromagnetic plane wave whose frequency is 2 GHz. The cloaking shell has an inner radius $R_1 = 0.1$ m, while the outer radius is $R_2 = 0.2$ m. From 0 to $R_0 = 0.05$ m, the space is occupied by a PEC cylinder. Then, from R_0 to R_2, different cases are envisaged and the results are depicted in Fig. 4.22.

- **(a)** From R_0 to R_1, there is free space, and from R_1 to R_2 we use the cloaking parameters of Eq. 4.67 with $c = 0.001$ m, and $d = 0.02$ m. The computed electric field mapping is presented in Fig. 4.22(a). Although we are in a nonideal situation, mainly due to the lack of extreme values at $r = R_1$, the cloaking effect can be achieved.

- **(b)** From R_0 to R_1, the anticloak parameters of Eq. 4.69 are used, while Eq. 4.67 is used for the cloaking shell from R_1 to R_2. In both case, c and d are still equal to 0.001 and 0.02, respectively. The result, shown in Fig. 4.22(b), shows that the anticloak destroys the cloaking effect observed in Fig. 4.22(a).

- **(c)** The modeling differs from the previous one in one fundamental point: $c = 0$, i.e., the parameters of Eqs. 4.67 and 4.69 take now extreme values at $r = R_1$. The electric field is depicted in Fig. 4.22(c). The main conclusion is that the cloaking effect is no longer perturbed by the presence of the anticloak inside. Furthermore, since losses in metamaterials are unavoidable, we have incorporated a low level of electric losses to the cloak in order to make the modeling more physically realistic. It turns out that no significant deviation in the result is observed: the anticloak is still concealed by the cloak. Consequently, the lossless media that was first considered can be treated as the limit of the lossy case as the dissipation approaches zero. This

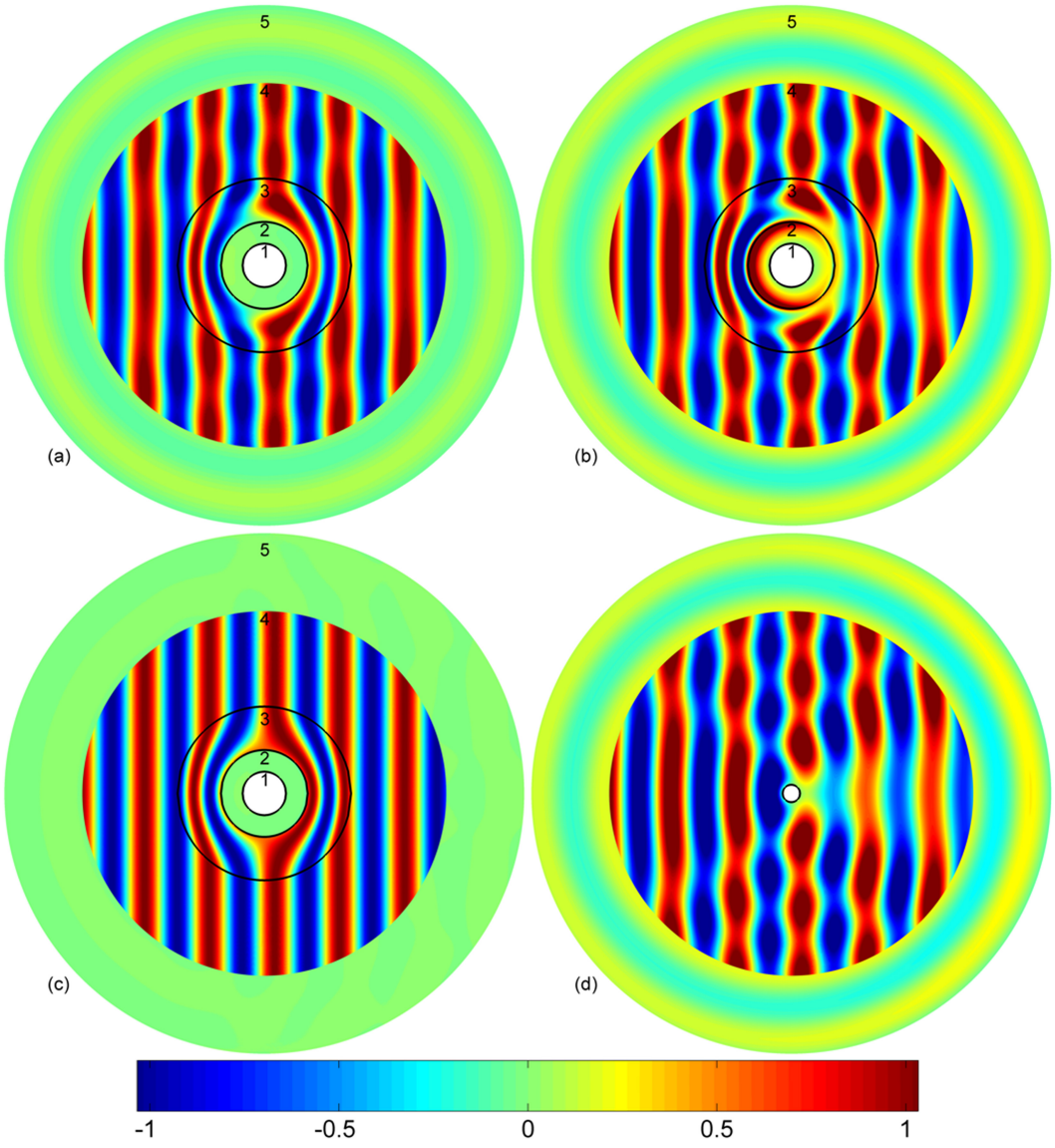

Figure 4.22: Color online. Electric field mapping for four configurations. **(a)** non-ideal ($c = 0.001$) cloaking structure with free space in the extended layer; **(b)** non-ideal ($c = 0.001$) cloaking structure with anticloak in the extended layer; **(c)** ideal ($c = 0$) cloaking structure with anticloak in the extended layer; **(d)** PEC cylinder with radius d. Five regions are apparent: **(1)** PEC cylinder; **(2)** Extended layer; **(3)** Cloaking shell; **(4)** Free space; **(5)** Scattered field region.

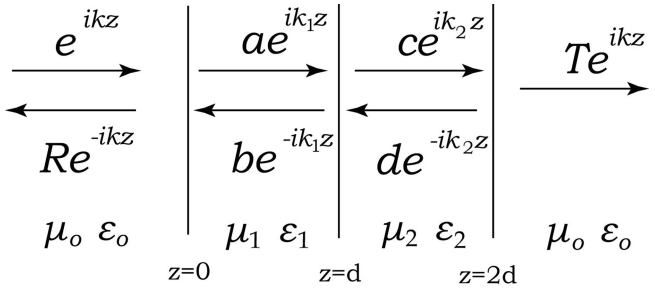

Figure 4.23: Simple model illustrating why a normally incident wave cannot penetrate a slightly dispersive ideal cloak/anticloak double layered slab.

indicates that the uniqueness theorem [80], stating that a field in a lossy region is unique, can be extended to the lossless media for which the theorem breaks down in general.

- **(d)** For completion sake, a simple PEC cylinder, with radius equal to d is modeled. The corresponding electric field mapping is shown in Fig. 4.22(d). As it has been pointed out in [75], the scattering is qualitatively similar to case (b).

One important difference between time domain and frequency domain methods is that a time domain method always gives a unique solution, while a frequency domain method may have multiple solutions for a lossless case given that the uniqueness theorem does not hold in general for a purely lossless case [80]. In order to justify uniqueness in a non-dissipative media, infinitesimal losses are traditionally assumed. This treatment is realistic because losses are always unavoidable. In order to explain the physics behind the non-penetration of electromagnetic waves through the interface between an ideal cloak and an ideal anticloak, we adopt a model similar to that of [73]. As depicted in Fig. 4.23, a plane wave is normally incident onto a double-layer medium composed of two regions: region 1 and region 2. The permittivity of the material in region 1 is ε_1, while its permeability is μ_1 . The material in region 2, of permittivity ε_2 and permeability μ_2, is obtained by the coordinate transformation $x = -x'$, which leads to $\varepsilon_2 = -\varepsilon_1$ and $\mu_2 = -\mu_1$. From the transformation-theory point of view, region 2 is able to perfectly reconstruct the electromagnetic space in region 1, so that region 1 is canceled by region 2, as if nothing were there. This property can be verified by straightforward calculations [75]. However, the materials at both sides of the cloak/anticloak interface have extreme values that may alter the effect of the can-

celation. In agreement with the value of permittivity and permeability at the inner boundary of the cloak, we let $\varepsilon_1 \to +0$ and $\mu_1 \to +\infty$ while their product remains constant, such that $\varepsilon_1\mu_1 = \varepsilon_0\mu_0$. Consequently, $\varepsilon_2 \to -0$ and $\mu_2 \to -\infty$ while $\varepsilon_2\mu_2 = \varepsilon_0\mu_0$. In order to represent the losses, a constant imaginary part is incorporated to the constitutive parameters: the permittivity and permeability in region 1 are now $\varepsilon_1 + i\delta$ and $\mu_1 + i\delta$, respectively; those in Region 2 are $-\varepsilon_1 + i\delta$ and $-\mu_1 + i\delta$, respectively. Assuming that $\varepsilon_1 \to +0$ and $\mu_1 \to +\infty$, the transmission coefficient is calculated behind the double-layer slab in Fig. 4.23. It is found that the transmission coefficient in this case is zero, indicating that the typical losses which are intrinsic to any material ensure that the electromagnetic wave cannot penetrate through the cloak/anticloak interface.

If the cloak is non-dissipative and if $c = 0$, the analysis presented in [72, 75] cannot be carried out due to the singularity of the Hankel function at this point. Accordingly, the condition of conservation of the E-field and H-field's tangential components at $r = R_1$ is degenerated, which leads to the conclusion that more than one solution is analytically possible. However, the lossless medium can be consider as the limit of the lossy medium as $\delta \to 0$. This statement is strengthened by the numerical results obtained above showing that a slight dissipation in the cloak material is of no consequence to the E-field mapping depicted in Fig. 4.22(c). Thus, the uniqueness theorem holds and ensures that only one analytical solution is compatible with the physical limitation of loss. Though mathematically possible, the other ones do not represent the physical solution. In this sense, our numerical simulations clearly indicate that no field can penetrate the lossless cloak/anticloak boundary if μ_φ is infinite.

4.9 Summary

1. The advent of metamaterials has offered a new degree of freedom in the design of challenging devices. In this sense, a cloak is a metamaterial that has the capability of excluding the electromagnetic radiation from a certain volume of space. A coordinate transformation yields the value of the constitutive parameters of the cloak, which turns out to be an anisotropic medium having the ability to distort and steer the field around the concealed object.

2. Numerical simulations have an important role to play through their ability to predict and confirm phenomena. TLM cannot easily model media whose

ε and μ are tensors with off-diagonal elements, which is the case in Cartesian coordinates. Therefore, an approximation based on substituting the anisotropic cloaking shell by a medium made up of alternating multilayered isotropic medium must be employed in Cartesian coordinates.

3. A more accurate approach consist of using curved nodes that assume the shape of the cloak and that allow ε and μ to be diagonal tensors.

4. In the modeling of metamaterials, it was shown in section 2.6 that the TLM mesh is Drude-dispersive and that no artificial dispersion has to be added. This is in agreement with the nature of TLM that should be regarded as a modeling procedure rather than a direct numerical solution of the field equations. But it was also shown in the same section that the Drude-like behavior of a cylindrical mesh must be nuanced because of the r-dependance of coefficients that appear in the expression of $\widetilde{\varepsilon}(\omega)$ and $\widetilde{\mu}(\omega)$. Thus, enforcing the cylindrical TLM mesh to fulfill the causality condition turns out to generate a set of restrictions for the TLM parameters, which is detrimental to the versatility of the modeling. This slightly limit the advantages of using cylindrical nodes.

5. It is pertinent to take into account the dispersiveness of a cloak only if the incoming plane wave is non-monochromatic. It has been shown that the frequency center of a quasimonochromatic wave is blueshifted in the forward direction after passing through a dispersive cloaking structure. Furthermore, it has been proven that the frequency shift distribution depends on the observation angle.

6. Because of the radial dependence of the constitutive parameters of the cloak, the velocity of the electromagnetic wave inside the device is smaller at the vicinity of its inner boundary. Consequently, while the phase of the electromagnetic signal is conserved, its envelope exhibits a time delay in the process of reaching a plane located at a constant distance from the structure. Furthermore, it has been shown that the time delay depends on the coordinate transformation that has been used to get ε and μ of the cloak.

7. We have verified that an anticloak is effective for an almost perfect cloak. However, we have proven that TLM can efficiently model dielectric or magnetic constants tending to infinity, which allows the simulation of the ideal

situation. The numerical results clearly show that the anticloak cannot defeat the cloaking phenomenon in the presence of an extreme layer, even if slightly electric losses are incorporated into the material. With a simple analytical model, we have mathematically demonstrated the result for a lossy medium; the lossless case following from the uniqueness theorem.

Chapter 5

General conclusions

The TLM numerical simulations undertaken in the frame of this dissertation has allowed to enlighten several problems involving the interaction between electromagnetic plane waves and complex media. The various developments presented in this work may be separated into two main categories: contributions to TLM and application to physical systems.

- In chapter 2, TLM is not only presented with abundant details, several developments and improvements to the method are also reported in order to make possible the study of challenging media that the original procedure would not allow.

- In chapters 3 and 4, the numerical tools that we have developed are employed to the determination of the effective dielectric constant of composite materials and to the study of cloaking structures, respectively.

A new vision of the usual 2D TLM nodes is first proposed. According to it, they are no longer represented by a single circuit; as a replacement, coupling circuits are used, each one describing a particular component of the electromagnetic field. So far, this statement was established only for the Symmetrical Condensed Node (SCN), i.e., the 3D counterpart. Such a treatment provides great versatility to the node such as the possibility to account for electric and magnetic losses, for instance. The new node, as well as SCN, are extended to model metamaterials, the required modifications not representing an added complexity to the method. The inherent dispersion thus introduced in the TLM mesh is derived.

TLM is used to determine the effective permittivity of composite materials. Several conclusions are drawn, the most significant ones are: i) no prediction

theory is able to offer a specific value of effective permittivity, ii) small inclusions embedded in a composite matrix offer a greatest predicability than bigger inclusions and iii) periodic square inclusions are described by Maxwell-Garnett's theory regardless of the volume fraction.

TLM has been shown capable of providing highly accurate modeling of cloaking structures. Seizing this powerful tool, phenomena such as frequency-shift or time-delays are investigated. Furthermore, we have demonstrated that TLM can be used for the modeling of exotic materials that exhibit infinite value of permittivity/permeability. The angular component of the constitutive parameters of an ideal cylindrical cloak must be infinite at the inner boundary of the shell, thus TLM has been employed to demonstrate that no anticloak can stray an ideal cloak from its faculty to make an object invisible.

Chapter 6

Resumen de la tesis

6.1 Introducción y esquema

Desde el trabajo de James Clerk Maxwell in 1873, la teoría de ondas electromagnéticas ha permitido importantes avances científicos. Sin embargo, la existencia geometrías internas o condiciones de contorno complejos puede convertir la resolución de un problema electromagnético en una tarea difícil, si no imposible. Esta dificultad puede superarse mediante el uso de métodos numéricos. El hilo conductor de esta tesis es la simulación de medios complejos con el método *Transmisión Line Modeling* (TLM) [1].

La mayor parte de los métodos numéricos parten de la derivación de una ecuación integral. Esta ecuación se resuelve numéricamente usando diferentes métodos, tal como el *Finite Element Method* [2] o el *Method of Moments* [3]. De alguna manera, estos últimos enfoques se pueden considerar semi-analíticos. De hecho, una parte importante de estas técnicas es la obtención de una ecuación analítica previa a la resolución numérica en sí misma. Estos métodos numéricos proporcionan buenos resultados, aunque tienen la desventaja de que cualquier cambio en el problema inicial exige la reformulación de la parte teórica. Por ejemplo, las ecuaciones integrales que describen un problema a bajas o a altas frecuencias no son las mismas.

Las técnicas numéricas basadas en la resolución de ecuaciones diferenciales que trabajan en el dominio del tiempo, tal como el método *Finite Differences in the Time Domain* (FDTD) [4, 5] or TLM, representan un enfoque altenativo. En su version básica, estas técnicas consideran simultáneamente las ecuaciones de Maxwell y las condiciones de contorno para simular un fenómeno dado. Resolver

el problema de esta forma puede parecer de algún modo poco elegante puesto que el problema es enteramente resuelto por el ordenador, siendo mínimo el esfuerzo teórico por parte del científico. La principal desventaja de los métodos diferenciales es que la carga computacional suele ser bastante alta comparada con los métodos semi-analíticos. Sin embargo, las ventajas de los métodos que trabajan en el dominio temporal son múltiples:

- Son fácilmente adaptables a nuevas situaciones, siendo mínimas las modificaciones en el código fuente.
- Con una única simulación se puede cubrir un gran intervalo de frecuencias a través de una simple transformada de Fourier.
- Dado que el campo electromagnético se calcula en toda la malla, es posible visualizar el proceso dinámico del fenómeno. Dicho proceso dinámico puede ser útil para entender el fenómeno, o simplemente para ayudar a confirmar que la simulación funciona correctamente.

Estas características hacen que estos métodos constituyan una herramienta atractiva para la simulación de problemas variados.

En esta tesis doctoral se discute el método TLM. Aportaremos varios desarrollos al método que permitan tratar problemas que involucren medios complejos. TLM es, al igual que FDTD, un método de bajas frecuencias para la simulación de la propagación de ondas. Aunque se suele utilizar para problemas de electromagnetismo, también ha sido empleado en el campo de la acústica [6], de la difusión de partículas [7], o de la propagación de ondas electromagnéticas en la atmósfera de cuerpos celestes [8]. Debido a la clara similitud entre TLM y FDTD, ambos métodos han sido frecuentemente comparados [9–12]; estos análisis comparativos han demostrado que sus prestaciones son en realidad totalmente comparables. Sin embargo, existen algunas ventajas de TLM con respecto a FDTD que cabe destacar:

- TLM define todas las componentes del campo en el mismo punto, en concreto en el centro de las células elementales (los nudos), formadas por líneas de transmisión cruzadas, y en el mismo instante. FDTD no puede contar con tal versatilidad ya que las componentes se calculan en puntos separados. Además, los campos eléctricos y magnéticos no se calculan en el mismo instante; por lo tanto el proceso FDTD se efectúa en dos pasos.

- Lo que realmente diferencia a los dos métodos es el enfoque radicalmente distinto que hacen del sistema físico a simular. Mientras que FDTD es una forma aproximada de resolver ecuaciones en derivadas parciales, TLM es una simulación del propio sistema a través líneas de transmisión. De esta manera, la aproximación se encuentra en el modelado y no en su solución.

La principal desventaja de TLM es que no es un método tan popular como FDTD. Por lo tanto, no hay muchos desarrollos previos disponibles para ayudar a un físico que quisiera realizar simulaciones numéricas con dicho método. Por tanto, emplear TLM necesita un alto entendimiento del método ya que dicho físico tendrá seguramente que desarrollar sus propias herramientas.

Los resultados que se presentan en esta tesis están basados en artículos publicados por el autor y sus colaboradores en revistas y conferencias científicas [13–26]. Los primeros medios que simulamos son medios compuestos, siendo nuestro objetivo la determinación de la permitividad efectiva de una mezcla de dieléctricos. En segundo lugar, investigamos la interacción entre dispositivos de invisibilidad (*cloaks*) y ondas electromagnéticas en el capitulo 4. Previamente, el capitulo 2 se dedica a la presentación detallada del método TLM. Además, se presenta un estudio sobre la manera de modelar metamateriales con TLM.

6.2 El método TLM

Usando redes eléctricas para resolver problemas que involucran la propagación de campos electromagnéticos es una técnica muy establecida desde los años 40 cuando Kron [27] y Whinnery [28] presentaron sus trabajos precursores. Inspirados por estas contribuciones, Johns y Beurle crearon TLM en 1971 [1]. TLM es un método numérico que trabaja en el dominio del tiempo y que se puede considerar como el equivalente eléctrico del principio de Huygens para la propagación de la luz. Este principio afirma que cada punto en una frente de onda primaria se puede considerar como una nueva fuente de una onda esférica segundaria y que una frente de onda segundaria se puede construir como el envuelto de estas frentes de onda segundarias. De la misma manera, la discretización del espacio conduce a la malla TLM en la cual cada pulso de tensión que se propaga es una nueva fuente de radiación. El centro de los nudos esta formado por el cruce de varias líneas de transmisión – con impedancia característica Z_0 o, equivalentemente, con admitancia $Y_0 = 1/Z_0$ – y la malla esta hecha con una gran cantidad de nudos. Por lo tanto, la malla constituye una red de líneas de transmisión en la cual los pulsos se

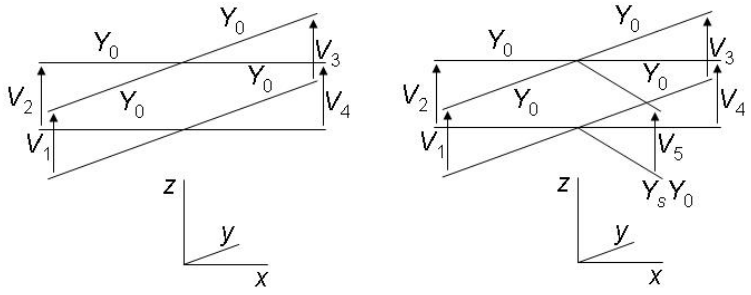

Figure 6.1: Nudo paralelo bidimensional: (a) sin stub, (b) con stub.

propagan según la teoría de estas líneas. Por la analogía existente entre esta teoría y las ecuaciones de Maxwell, los pulsos que se esparcen en la red representan una onda electromagnética propagándose en un cierto medio.

El nudo Cartesiano que presentaron Johns y Beurle en su papel original esta representado en Fig. 6.1(a). Se trata de un circuito paralelo, es por ello que este nudo esta conocido como nudo paralelo. A bajas frecuencias, Johns mostró que este nudo se puede representar por una red de bobinas, con inductancia L, y de condensadores, con capacidad C. Resulta que las ecuaciones describiendo esta red son análogas a las de Maxwell para una onda electromagnética que se propaga con el campo eléctrico normal al plano de propagación (modo TE). Los pulsos incidentes penetran dentro del nudo de Fig. 6.1(a) desde las cuatro puertas; la información esta contenida en el vector de voltaje,

$$\overline{V}^i = \begin{pmatrix} V_1 \\ V_2 \\ V_3 \\ V_4 \end{pmatrix}^i . \tag{6.1}$$

Cuando alcanzan el centro de los nudos, los pulsos incidentes están dispersados en

las cuatro direcciones posibles, lo que da lugar a un conjunto de pulsos reflejados:

$$\overline{V}^r = \begin{pmatrix} V_1 \\ V_2 \\ V_3 \\ V_4 \end{pmatrix}^r . \tag{6.2}$$

La redistribución de los pulsos incidentes se hace vía una matriz de dispersión, S, de tal modo que,

$$\overline{V}^r = \mathbf{S}\overline{V}^i. \tag{6.3}$$

La determinación de S es un paso importante del método, y dado la simple topología del nudo paralelo, la obtención de S es directa en este caso. Cálculos triviales conducen a

$$\mathbf{S} = \frac{1}{2}\begin{pmatrix} -1 & 1 & 1 & 1 \\ 1 & -1 & 1 & 1 \\ 1 & 1 & -1 & 1 \\ 1 & 1 & 1 & -1 \end{pmatrix}. \tag{6.4}$$

No obstante, obtener la matriz de dispersión para un nudo más complicado puede ser muy difícil; afortunadamente, existe una técnica que simplifica de manera considerable la tarea.

Los parámetros (L y C) pueden ajustarse para controlar el valor local de la permitividad y permeabilidad. Pero de esta manera, el nudo de Fig. 2.1(a) es solo capaz de similar medios homogéneos ya que la capacidad y inductancia de las líneas de transmisión se quedan constantes a través toda la malla. Sin embargo, extra capacidad se puede añadir al nudo equipando el nudo con una líneas de transmisión, llamado un stub en el método TLM, de tal manera que la permitividad sea variable. Es importante notar que el stub esta conectado al centro del nudo y no a otras líneas de los nudos adyacentes ya que los stubs controlan la velocidad de la propagación y en ningún caso la propagación en si mismo. El nudo paralelo con stub esta representado en Fig. 6.1(b), donde se puede observar que una quinta línea ha sido añadido. Sin embargo, este procedimiento no permite variación de la permeabilidad lo que constituye una seria limitación. Otro punto fundamental es que este nudo se suele representar por un circuito eléctrico único con el fin de calcular el campo electromagnético en función de los pulsos de tensión [31]. Todo lo que acabamos de decir se podría adaptar a la descripción de ondas electromagnéticas propagándose con el campo magnético perpendicular al plano de propagación (TM mode). En este caso referimos al nudo serie que es

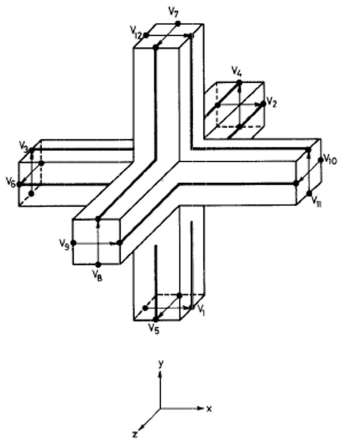

Figure 6.2: El Nudo Simétrico Condensado sin stub.

equivalente a un circuito eléctrico serie.

Una contribución importante por TLM fue el desarrollo del Nudo Simétrico Condensado (SCN), igualmente propuesto por Johns [29], para resolver problemas tridimensionales (3D). Hasta la aparición del SCN, nudos pocos elegantes, con topología compleja, solían ser empleado para problemas 3D. Puesto que SCN elimina las desventajas de los otros nudos, estos últimos son totalmente obsoletos e ya no usados. El SCN sin stubs, como aparece en el artículo de Johns, se puede ver en Fig. 6.2. Johns afirmó que el SCN no se puede representar por un solo circuito eléctrico, como era el caso para el nudo 2D pero al precio de que solo una componente de las constantes ópticas puede variar. Efectivamente, las líneas de transmisión deben acoplarse entre ellas, en acuerdo con el hecho de que las componentes del campo electromagnético se acoplan entre ellas en las ecuaciones de Maxwell. La afirmación de Johns era por supuesto verdadera: no existe un circuito único que puede representar el SCN. Sin embargo, Taylor y sus colaboradores [30, 32] mostró que el SCN se puede representar por un conjunto de circuitos paralelos y de circuitos series, cada línea de transmisión del nudo aparece en un circuito paralelo y un circuito serie. Esta descripción fue reservada al SCN durante mucho tiempo.

Sin embargo, hemos mostrado [14] que incluso los nudos 2D deben ser representados por un conjunto de circuitos paralelos/series. En realidad, la representación del nudo paralelo por un único circuito limita su validez a medios por

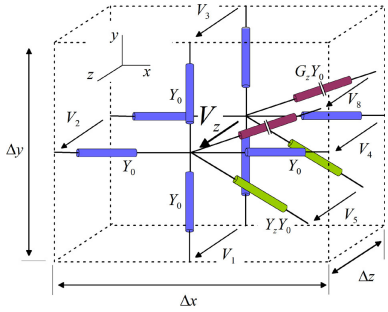

(a) Sub-circuito paralelo para la componente z de la ley de Ampère que define E_z.

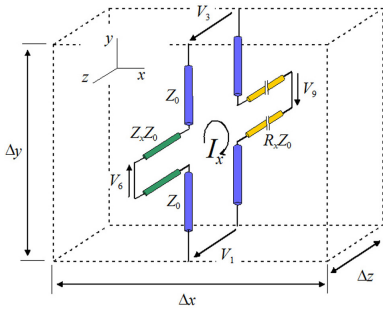

(b) Sub-circuito serie para la componente x de la ley de Faraday que define H_x.

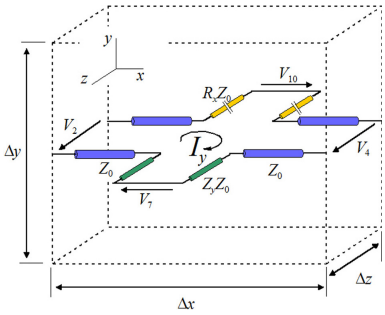

(c) Sub-circuito serie para la componente y de la ley de Faraday que define H_y.

Figure 6.3: Subdivisión del nudo global para modos TE en tres sub-circuitos.

los cuales solo términos capacitivos, como la permitividad por ejemplo, son variables. Por lo contrario, describir el nudo paralelo como un conjunto de circuitos le da más versatilidad al nudo; permite en particular la simulación de magnitud inductiva, como la permeabilidad. Además, perdidas eléctricas y magnéticas pueden considerarse. In Fig. 6.3, el nudo global para modos TE esta representado. Puesto la complejidad de tal nudo, la expresión de la matriz de dispersión no es tan sencilla como en Eq. 6.4. Cálculos extensivos (véase sección 2.3.1) conducen

a

$$\mathbf{S} = \begin{bmatrix} a_x & c & b_x & c & g & -i_x & 0 \\ c & a_y & c & b_y & g & 0 & i_y \\ b_x & c & a_x & c & g & i_x & 0 \\ c & b_y & c & a_y & g & 0 & -i_y \\ c & c & c & c & f & 0 & 0 \\ -e_x & 0 & e_x & 0 & 0 & h_x & 0 \\ 0 & e_y & 0 & -e_y & 0 & 0 & h_y \end{bmatrix}. \tag{6.5}$$

Los elementos de la matriz están dados en la expresión siguiente:

$$\begin{aligned} a_k &= \tfrac{2}{4+Y_z+G_z} - \tfrac{2}{2+Z_k+R_k}, & f &= \tfrac{Y_z-G_z-4}{Y_z+G_z+4}, \\ b_k &= \tfrac{2}{4+Y_z+G_z} - \tfrac{Z_k+R_k}{2+Z_k+R_k}, & g &= \tfrac{2Y_z}{4+Y_z+G_z}, \\ c &= \tfrac{2}{4+Y_z+G_z}, & h_k &= \tfrac{2-Z_k+R_k}{2+Z_k+R_k}, \\ e_k &= \tfrac{2Z_k}{2+Z_k+R_k}, & i_k &= \tfrac{2}{2+Z_k+R_k}, \end{aligned} \tag{6.6}$$

con $k = \{x, y\}$, y donde Y, Z, G, and R representan respectivamente la admitancia de los stubs para la permtividad, la impedancia de los stubs para la permeabilidad, la admitancia de los stubs para la conductividad eléctrica, y la impedancia de los stubs para la conductividad magnética. Concretamente, esos parámetros se expresan como:

$$Z_x = \frac{2\mu_x\mu_0}{Z_0\Delta t}\frac{\Delta y\Delta z}{\Delta x} - 2, \tag{6.7a}$$

$$Z_y = \frac{2\mu_y\mu_0}{Z_0\Delta t}\frac{\Delta x\Delta z}{\Delta y} - 2, \tag{6.7b}$$

$$Y_z = \frac{2\varepsilon_z\varepsilon_0}{Y_0\Delta t}\frac{\Delta x\Delta y}{\Delta z} - 4. \tag{6.7c}$$

donde Δt es el paso temporal del método, mientras que Δx, Δy, y Δz representan las dimensiones del nudo en todas las direcciones.

So y sus compañeros mostraron que invertir la naturaleza capacitiva y inductiva de los stubs permite la simulación de metamaterial, es decir medios con $\varepsilon \leq 1$ and $\mu \leq 1$, a través de modificaciones importantes de la versión usual [43]. Sin embargo, demostramos que modificaciones tan drásticas no son necesarias en re-

alidad [15, 16], invertir las bobinas y los condensadores afecta solamente a Eqs. 6.7 que hay que multiplicar por el factor $-\frac{1}{4}\Delta t^2\omega^2$ (ω siendo la frecuencia angular) y que se convierten entonces en:

$$Z_x = -\frac{1}{4}\Delta t^2\omega^2 \left[\frac{2\mu_x\mu_0}{Z_0\Delta t}\frac{\Delta y\Delta z}{\Delta x} - 2\right], \tag{6.8a}$$

$$Z_y = -\frac{1}{4}\Delta t^2\omega^2 \left[\frac{2\mu_y\mu_0}{Z_0\Delta t}\frac{\Delta x\Delta z}{\Delta y} - 2\right], \tag{6.8b}$$

$$Y_z = -\frac{1}{4}\Delta t^2\omega^2 \left[\frac{2\varepsilon_z\varepsilon_0}{Y_0\Delta t}\frac{\Delta x\Delta y}{\Delta z} - 4\right]. \tag{6.8c}$$

Un análisis profundo de este procedimiento muestra que la dispersión introducida en la malla con este tratamiento sigue un modelo de tipo Drude (véase sección 2.6).

6.3 Materiales compuestos

Los materiales compuestos comenzaron a estudiarse por primera vez hace mas de 150 años. En concreto, las primeras trazas datan de 1837, cuando Faraday propuso un modelo de dieléctrico que consistía en una serie de glóbulos metálicos separados por un material aislante. Desde entonces, el interés en estos materiales ha ido creciendo. Físicos conocidos como Mossotti, Clausius, o Maxwell, abordaron el problema a nivel teórico [45]. Hoy en día, el problema no es solo de interés fundamental sino también práctico, dado que los materiales compuestos se emplean de manera masiva en la industria. El éxito de los materiales compuestos radica en la posibilidad que éstos ofrecen para obtener propiedades diferentes en función de las distintas fases que constituyen la mezcla. Dadas las analogías matemáticas, todo lo que se puede concluir para una mezcla es válido tanto para la constante dieléctrica, como para la permeabilidad magnética, conductividad eléctrica, conductividad calorífica y difusión [46]. En este estudio, sin embargo, estamos interesados únicamente en la constante dieléctrica o permitividad de medio. Debido a la complejidad del problema, especialmente en mezclas aleatorias, los materiales compuestos no han podido ser estudiados mediante métodos numéricos hasta recientemente, cuando ordenadores de alto poder computacional han estado al alcance de la mano. En este capítulo, TLM se utiliza para el modelado materiales compuestos.

Las teorías de Maxwell-Garnett (MG) [48] y Bruggeman [49] son, sin duda, los dos modelos más conocidos para la predicción de la permitividad efectiva en términos de la permitividad ε_i, y fracción de volumen, p_i, de cada fase de la mezcla. Según MG, la permitividad efectiva de una mezcla compuesta por dos fases viene dada por

$$\frac{\varepsilon_{eff}-\varepsilon_2}{\varepsilon_{eff}+(d-1)\varepsilon_2}=p_1\frac{\varepsilon_1-\varepsilon_2}{\varepsilon_1+(d-1)\varepsilon_2}, \tag{6.9}$$

mientras que Bruggeman establece que

$$p_1\frac{\varepsilon_1-\varepsilon_{eff}}{\varepsilon_1+(d-1)\varepsilon_{eff}}=p_2\frac{\varepsilon_2-\varepsilon_{eff}}{\varepsilon_2+(d-1)\varepsilon_{eff}} \tag{6.10}$$

se cumple para la misma mezcla, siendo d la dimensionalidad del problema.

Otro tipo de enfoque consiste en determinar el rango de valores posibles para la permitividad efectiva, en lugar de intentar obtener un valor preciso. Por ejemplo, los límites de Wiener vienen dados por [50]:

$$\varepsilon_{eff,max}=p_1\varepsilon_1+p_2\varepsilon_2, \tag{6.11a}$$

$$\varepsilon_{eff,min}=(\frac{p_1}{\varepsilon_1}+\frac{p_2}{\varepsilon_2})^{-1}. \tag{6.11b}$$

y los de Hashin-Shtrikman (HS) por [53]:

$$\varepsilon_{eff,max}=\varepsilon_+ + \frac{p_-}{\frac{1}{\varepsilon_- -\varepsilon_+}+\frac{p_+}{d\varepsilon_+}}, \tag{6.12a}$$

$$\varepsilon_{eff,min}=\varepsilon_- + \frac{p_+}{\frac{1}{\varepsilon_+ -\varepsilon_-}+\frac{p_-}{d\varepsilon_-}}, \tag{6.12b}$$

donde ε_+ y ε_- son los valores máximo y mínimo de la permitividad para las fases individuales, respectivamente; mientras que los valores de p_+ y p_- representan la fracción de volumen del medio cuya permitividad está dado por ε_+ and ε_-, respectivamente.

En primer lugar, se consideron inclusiones circulares de dilectrico insertadas en un medio homogéneo. Se realizaron cientos de simulaciones con TLM para obtener el comportamiento estadístico de las muestras. Este estudio nos permitió demostrar que no existe teoría capaz de predecir el valor específico de la permitividad efectiva en un medio aleatorio. Todos los valores pertenecientes al intervalo

definido por los límites de Wiener son posibles, sin embargo, el valor exacto resulta inaccesible con métodos analíticos. Por tanto, es necesario utilizar métodos numéricos para obtener dicho valor exacto.

Si la concentración de inclusiones es constante, las permitividades efectivas obtenidas para las distintas configuraciones internas siguen una distribución gaussiana con un valor medio y una desviación standard. Los límites HS han sido considerados los más restrictivos que pueden obtenerse a partir de las permitividades y fracción de volumen de las fases puras. Sin embargo, nuestros resultados han puesto esto en duda, puesto que observamos un número no despreciable de geometrías en las cuales se sobrepasan dichos límites debido al solapamiento entre las inclusiones. Además, parece que mientras más pequeñas son las inclusiones, menor es la desviación standard de la distribución. En otras palabras, la permitividad efectiva de un material compuesto por pequeñas inclusiones distribuidas de manera aleatoria está más cerca del valor medio característico. Por tanto, si uno conoce la fracción de volumen de estas inclusiones pequeñas, será capaz de predecir con bastante precisión la permitividad efectiva de la mezcla, independientemente como se organicen inclusiones. Esta conclusión tiene un gran interés en el diseño y manufacturación de dieléctricos compuestos. Si se considera todo el intervalo de fracciones de volumen, observamos que las predicciones teóricas funcionan bien para bajas concentraciones, pero ni Bruggeman ni MG son capaces de describir con precisión el comportamiento del sistema a altas concentraciones. Sin embargo, Bruggeman parece acercarse más a los resultados numéricos, especialmente en el caso de inclusiones con permitividad menor que la del medio que las contiene.

En segundo lugar, se estudió el efecto del tamaño de las inclusiones ε_{eff}. Para ello, se consideraron materiales con distintos tipos de inclusiones periódicas. Observamos que, si la concentración de inclusiones no es demasiado alta, las mezclas pueden describirse de manera bastante precisa con la fórmula de MG, independientemente de la forma de las inclusiones. Cuando la concetración de inclusiones aumenta, ε_{eff} diverge del comportamiento MG, además, el grado de divergencia depende de la geometría de las inclusiones. Una vez que se excede el límite de solapamiento, ε_{eff} muestra un cambio drástico hacia los límites de Wiener. Esto puede explicarse mediante la similitud existente entre distribuciones plano paralelas y las geometrias con solapamiento. A diferencia de las otras geometrías, las inclusiones cuadradas tienen la peculiaridad de que siguen la fórmula de MG independientemente de la fracción de volumen.

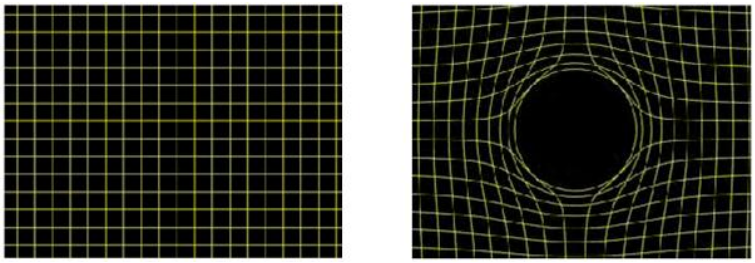

Figure 6.4: Desde el espacio original hasta el espacio distorsionado.

6.4 *Cloaks*: dispositivos de invisibilidad

El *cloak* de invisibilidad fue propuesto por Pendry y sus colaboradores [61]. Fundamentalmente, la idea es crear un agujero en cual toda radiación electromagnética esta excluida. Con este fin, la radiación electromagnética ha de estar conducida alrededor de la región que hay que hacer invisible, lo que parece ser en contradicción con el principio de Fermat estipulando que cualquier onda electromagnética que empieza a propagarse en una cierta dirección debe seguir esta línea. Sin embargo, se puede imaginar otro espacio relacionado con el original por una transformación matemática. Consideramos un entramado que define un volumen oculto, como se representa en Fig.6.4. En consecuencia, toda onda propagándose en este entramado distorsionado contorna el espacio vacío. Lo importante es determinar lo que ocurre a las ecuaciones de Maxwell en tal transformación. Resulta que las ecuaciones tienen exactamente la misma forma [62], pero las constantes dieléctricas y magnéticas son multiplicadas por un factor dado. Por lo tanto, transformar las propiedades del material es equivalente a distorsionar el espacio original. Esto significa que el espacio fuera del volumen disimulado se puede substituir por un material nuevo: el *cloak*. Merece la pena subrayar que los parámetros constitutivos del *cloak*, sean lo que sean sus complejidad, son consistentes con las leyes físicas. Usando una transformación lineal, estos parámetros constitutivos de un *cloak* 2D vienen dados por:

$$\varepsilon_r = \mu_r = \frac{r - R_1}{r}, \tag{6.13a}$$

$$\varepsilon_\varphi = \mu_\varphi = \frac{r}{r - R_1}, \tag{6.13b}$$

$$\varepsilon_z = \mu_z = [\frac{R_2}{R_2 - R_1}]^2 \frac{r - R_1}{r}. \tag{6.13c}$$

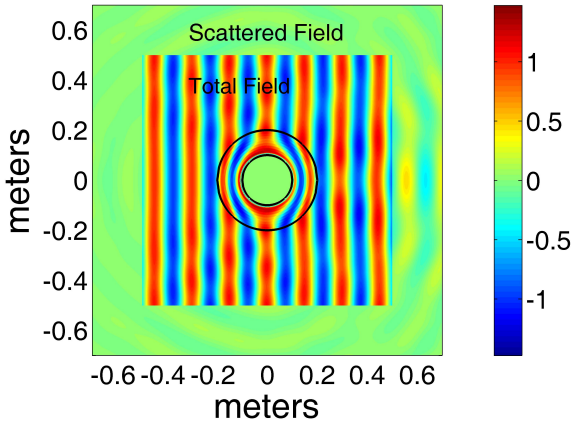

Figure 6.5: Amplitud total (parte interior del cuadro) y dispersadas (parte exterior del cuadrado) del campo eléctrico por un cilindro conductor perfecto rodeado de un *cloak*.

Para el *cloak* 3D, las formulas

$$\varepsilon_r = \mu_r = \frac{R_2}{R_2 - R_1}\left(\frac{r - R_1}{r}\right)^2, \tag{6.14a}$$

$$\varepsilon_\theta = \mu_\theta = \frac{R_2}{R_2 - R_1}, \tag{6.14b}$$

$$\varepsilon_\varphi = \mu_\varphi = \frac{R_2}{R_2 - R_1}, \tag{6.14c}$$

se obtienen. En esta formulas, R_1 y R_2 son respectivamente las interfaces interna y externa del *cloak*. Para el *cloak* 2D, podemos ver que ε_φ y μ_φ tienden a infinito.

Simulaciones numéricas tienen un papel importante puesto sus capacidades para predecir y confirmar fenómenos. Emplear los nudos TLM cartesianos es problemático porque los tensores de permitividad y permeabilidad (Eqs. 6.13 y 6.14), que son diagonal en coordenadas cilindricas o esfericas, se vuelven no diagonal en coordenadas cartesianas. TLM no puede procesar tensores no diagonal de manera trivial, y tuvimos que usar una técnica, propuesta por Huang [78], que consiste en substituir el medio anisótropo por una estructura alternante de capas concéntricas de materiales isótropos y homogéneo. Con esta aproximación, el mapa de intensidad del campo eléctrico por un *cloak* 2D se puede observar en Fig. 6.5. Claramente, se logra el efecto *cloaking* aunque se puede notar un dispersión

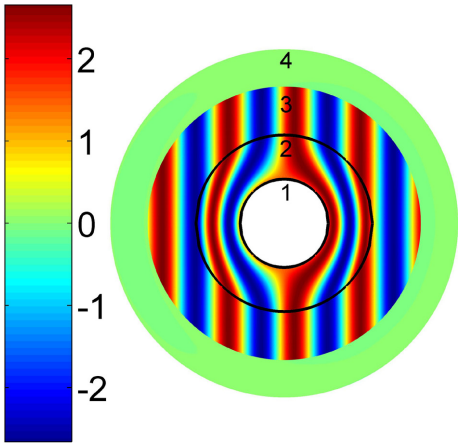

Figure 6.6: Mapa del campo magnético ($\times 10^{-3}$). Cuatro regiones se observan: (1) Cilindro conductor, (2) *Cloak*, (3) Vacío, (4) Región de campo dispersado.

no nula hacia adelante.

Si nudos directamente cilíndricos se emplean en lugar de los habituales nudos cartesianos, el resultado mejora mucho, como se puede observar en Fig. 6.6, en la cual se puede ver que la dispersión es casi nula en todas las direcciones. En este ultimo ejemplo, la polarización de la onda incidente era TM.

En lo que concierne las propiedades de la estructura de cloaking, los resultados que hemos encontrado son:

1. La frecuencia de una onda casi-monocromática sufre un desplazamiento hacia el azul en la dirección hacia adelante después de haber cruzado un *cloak* dispersivo 2D. Además el desplazamiento de frecuencia depende del ángulo de observación.

2. Puesta la dependencia de los parámetros constitutivos del *cloak*, la velocidad de la onda dentro del dispositivo es menor cerca de su interfaz interna. Por lo tanto, mientras que la fase de la señal se conserva, su envolvente muestra un retardo temporal al alcanzar un plano ubicado a una distancia constante de la estructura.

3. Hemos verificado que un material, un *anti-cloak*, puede destruir el efecto de un *cloak* casi perfecto. Por otra parte, con TLM, se puede asumir permitivad y permeabilidad que tienden a infinito, lo que nos permite sim-

ular la situación ideal. Los resultados numéricos muestran que el *anti-cloak* ya no es efectivo en presencia de una capa con ε_φ,$\mu_\varphi \rightarrow \infty$, incluso si leves perdidas estan incorporado al material. Dicho resultado se ha demostrado matemáticamente para un medio con perdidas utilizando un modelo analítico simple. Sin embargo, el teorema de unicidad [80] ha permitido generalizar este descubrimiento al caso de un medio no conductor.

6.5 Conclusiones generales

Las simulaciones numéricas realizadas en el marco de esta Tesis Doctoral han permitido entender diversos problemas relacionados con la interacción entre ondas electromagneticas planas y medios complejos. El trabajo presentado en este manuscrito se divide en dos categorías: contribuciones al método numérico TLM en sí mismo y aplicaciones de dicho método a sistemas físicos.

- En el capítulo 2, no solo se presenta el método numérico TLM en detalle, también se muestran las mejoras que se han hecho en el método para adaptarlo a las características de ciertos medios complejos, que no podían ser estudiados con el método original.

- En los capítulos 3 y 4, se emplean estas nuevas herramientas numéricas para determinar la constante dielectrica efectiva de materiales compuestos y estudiar estructuras de cloaking respectivamente.

En primer lugar, se propone una nueva visión de los nudos TLM bidimensionales. En este nuevo enfoque, los nudos no se representan por un circuito simple, sino por un sistema de circuitos acoplados, cada uno de los cuales describe una componente particular del campo electromagnetico. Hasta ahora, este concepto había sido aplicado solo al caso tridimensional, es decir, al Symmetrical Condensed Node (SCN). Este tratamiento confiere gran versatilidad al nudo, por ejemplo, la posibilidad de tener en cuenta las perdidas eléctricas o magnéticas. El nuevo nudo bidimensional, junto con el nodo SCN, han sido desarrollados para permitir el modelado de metamateriales. Las modificaciones necesarias, sin embargo, no añaden ninguna complejidad extra al método. Además de este desarrollo, hemos calculado la expresión de la dispersión inherente a la malla.

El método TLM se empleó para determinar la constante dieléctrica de materiales compuestos. De las las distintas conclusiones extraídas de este estudio, la

más significativas son: i) no existe ninguna teoría capaz de predecir el valor específico de la permitividad efectiva, ii) es más fácil predecir dicho valor en gotas pequenas que en gotas grandes y iii) la teoría de Maxwell-Garnett permite describir distribuciones periódicas de inclusiones cuadradas para cualquier fracción de volumen.

Se ha demostrado que el TLM es capaz de modelar de manera precisa las estructuras de *cloaking*. Aprovechando esta potente herramienta, hemos sido capaces de investigar fenómenos tales como desplazamientos en frecuencia o retardos temporales de la onda incidente al atravesar el *cloaking*. Además, hemos demostrado que el TLM puede utilizarse para modelar materiales exóticos con valores infinitos de permitividad/permeabilidad. La componente angular de los parámetros constitutivos de un *cloak* ideal cilíndrico tienen que ser infinitos en la superficie interna de la corteza que constituye el *cloak*. Según esto, hemos demostrado que no existe un *anticloak* capaz hacer que un *cloak* perfecto pierda su propiedad de hacer invisble a un objeto.

Bibliography

[1] P. B. Johns and R. L. Beurle. Numerical solution of 2-dimensional scattering problems using a transmission-line matrix. *Proc. Inst. Elec. Eng.*, 118(9):1203–1208, 1971.

[2] P. G. Ciarlet. *The Finite Element Method for Elliptic Problems*. North-Holland Publishing Company, Amsterdam, 1978.

[3] W. C. Gibson. *The Method of Moments in Electromagnetics*. Chapman and Hall/CRC, 2008.

[4] K. S. Yee. Numerical solution of initial boundary value problems involving maxwell's equations. *IEEE Trans. Antennas and Propagat.*, 14(3):302–307, 1966.

[5] A. Taflove and S. C. Hagness. *Computational Electrodynamics: The Finite-Difference Time-Domain Method*. Artech House, Norwood MA, third edition, 2005.

[6] W. O'Connor and F. Cavanagh. Transmission line matrix acoustic modelling on a pc. *Applied Acoust.*, 50:247–255, 1997.

[7] D. de Cogan. *Transmission Line Matrix (TLM) techniques for diffusion applications*. Gordon and Breach, Oxford, 1998.

[8] J. A. Morente, J. A. Portí, C. Blanchard, B. P. Besser, H. I. M. Lichtenegger, A. Salinas, E. A. Navarro, and G. J. Molina-Cuberos. Transmission line meshes for computational simulation of electromagnetic modes in the earth's atmosphere. *COMPEL*, 26:650–660, 2007.

[9] P. B. Johns. On the relationship between tlm and finite-difference methods for maxwell's equations. *IEEE Trans. Microwave Theory Tech.*, 35(1):2075–2084, 1987.

[10] C. Eswarappa and W. J. R. Hoefer. Bridging the gap between tlm and fdtd. *IEEE Microwave and Guided Wave Letters*, 43(8):4–6, 1995.

[11] D. H. Choi. A comparison of the dispersion characteristics associated with the tlm and fd-td methods. *Int. J. Num. Modelling: Electronic Networks, Device and Fields*, 2:203–214, 1989.

[12] P. B. Johns and G. Butler. The consistency and accuracy of the tlm method for diffusion and its relationship to existing methods. *Int. J. Num. Methods Eng.*, 19:1549–1554, 1983.

[13] C. Blanchard, J. A. Portí, J. A. Morente, A. Salinas, and E. Navarro. Determination of the effective permittivity of dielectric mixtures with the transmission line matrix method. *J. Appl. Phys.*, 102(6):064101, 2007.

[14] J. A. Portí, J. A. Morente, A. Salinas, M. Rodriguez-Sola, and C. Blanchard. On the circuit description of tlm nodes. *Int. J. Electron.*, 93:479–491, 2006.

[15] C. Blanchard, J. A. Portí, J. A. Morente, A. Salinas, and B-I Wu. Numerical determination of frequency behavior in cloaking structures based on l-c distributed networks with tlm method. *Opt. Express*, 16:9344–9350, 2008.

[16] C. Blanchard, J. A. Portí, B-I Wu, J. A. Morente, A. Salinas, and J. A. Kong. Time domain simulation of electromagnetic cloaking structures with tlm method. *Opt. Express*, 16:6461–6470, 2008.

[17] C. Blanchard, B-I Wu, J. A. Portí, H. Chen, B. Zhang, J. A. Morente, and A. Salinas. Response of cylindrical cloaks to a nonmonochromatic plane wave. Submitted to J. Opt. Soc. Am. B-Opt. Phys., 2009.

[18] C. Blanchard, B. Zhang, B-I Wu, J. A. Portí, H. Chen, J. A. Morente, and A. Salinas. Importance of the singular constitutive parameters of cylindrical cloaks: illustration on the anticloak concept. Submitted to J. Opt. Soc. Am. B-Opt. Phys., 2009.

[19] C. Blanchard, J. A. Portí, J. A. Morente, and A. Salinas. A plane-wave illumination algorithm for non-perpendicular electromagnetic incidence on an infinite dielectric medium with the tlm method. In *European Conference on Antennas and Propagation (EuCAP2006)*, Nice (France), Nov. 6-10 2006.

[20] C. Blanchard, J. A. Portí, A. Salinas, J. A. Morente, and M. Rodríguez-Sola. Time-varying electromagnetic-media modeling with tlm method. In *21st National Conference of the International Union of Radio Science*, Oviedo (Spain), Sept. 12-15 2006.

[21] A. Salinas, J. A. Morente, J. A. Portí, C. Blanchard, and M. Rodríguez-Sola. Formulatión of the dispersion matrix in the tlm method using mathematica. In *21st National Conference of the International Union of Radio Science*, Oviedo (Spain), Sept. 12-15 2006.

[22] J. A. Morente, B. P. Besser, J. A. Portí, H. I. M. Lichtenegger, A. Salinas, E. A. Navarro, G. J. Molina-Cuberos, M. Rodríguez-Sola, and C. Blanchard. Redes de líneas de transmisión para la simulación computacional de cavidades electromagnéticas: estudio de los modos ter y tmr en la atmósfera de la tierra. In *21st National Conference of the International Union of Radio Science*, Oviedo (Spain), Sept. 12-15 2006.

[23] C. Blanchard, J. A. Portí, B-I Wu, J. A. Morente, A. Salinas, and J. A. Kong. Time domain modeling of electromagnetic invisible shells. In *Progress in Electromagnetics Research Symposium*, Cambridge (USA), July 2-6 2008.

[24] J. A. Portí, C. Blanchard, J. A. Morente, A. Salinas, E. A. Navarro, and M. Rodríguez-Sola. Determinación de la permitividad de mezclas dieléctricas con el método tlm. In *23rd National Conference of the International Union of Radio Science*, Madrid (Spain), Sept. 22-24 2008.

[25] J. A. Morente, E. A. Navarro, C. Blanchard, A. Salinas, M. Rodríguez-Sola, J. A. Portí, and J. Fornieles. Un análisis de los espectros elf del campo eléctrico en la atmósfera de titán enviados por la misión cassini-huygens. In *23rd National Conference of the International Union of Radio Science*, Madrid (Spain), Sept. 22-24 2008.

[26] A. Salinas, J. A. Morente, J. A. Portí, C. Blanchard, M. Rodríguez-Sola, J. Fornieles, and I. Sanz. Innovación docente en prácticas de laboratorio tradicionales en electromagnetismo. In *23rd National Conference of the International Union of Radio Science*, Madrid (Spain), Sept. 22-24 2008.

[27] G. Kron. Equivalent circuit of the field equations of maxwell. *Proc. IRE*, 32:289–299, 1944.

[28] J. R. Whinnery and S. Ramo. A new approach to the solution of high frequency field problems. *Proc. IRE*, 32:284–288, 1944.

[29] P. B. Johns. A symmetrical condensed node for the tlm method. *IEEE Trans. Microwave Theory Tech.*, 35(4):370–377, 1987.

[30] J. A. Portí, J. A. Morente, and M. C. Carrión. Simple derivation of scattering matrix for tlm nodes. *Electron. Lett.*, 34:1763–1764, 1998.

[31] C. Christopoulos. *The Transmission-Line Modeling Method: TLM*. Oxford University Press, Oxford, 1995.

[32] P. Naylor and R. Ait-Sadi. Simple method for determining 3-d tlm nodal scattering in nonscalar problems. *Electron. Lett.*, 28:2353–2354, 1992.

[33] S. Akhtarzad and P. B. Johns. Generalized elements for t.l.m. method of numerical analysis. *Proc. Inst. Elec. Eng.*, 122:1349–1352, 1975.

[34] J. A. Morente, G. Gimenez, J. A. Portí, and M. Khalladi. Dispersion analysis for a tlm mesh of symmetrical condensed nodes with stubs. *IEEE Trans. Microwave Theory Tech.*, 43:452–456, 1995.

[35] S. Akhtarzad and P. B. Johns. Solution of maxwell's equations in three space dimensions and time by the t.l.m. method of analysis. *Proc. Inst. Elec. Eng.*, 122:1344–1348, 1975.

[36] J. B. Pendry, A. J. Holden, D. J. Robbins, and W. J. Stewart. Low frequency plasmons in thin-wire structures. *J. Phys. Condens.Matter*, 10:4785–4809, 1998.

[37] J. B. Pendry, A. J. Holden, D. J. Robbins, and W. J. Stewart. Magnetism from conductors and enhanced nonlinear phenomena. *IEEE Trans. Microwave Theory Tech.*, 47:2075–2084, 1999.

[38] D. R. Smith, W. J. Padilla, D. C. Vier, and S. Nemat-Nasser, S. C.and Schultz. Composite medium with simultaneously negative permeability and permittivity. *Phys. Rev. Lett.*, 84:4184–4187, 2000.

[39] G. V. Eleftheriades, A. K. Iyer, and P. C. Kremer. Planar negative refractive index media using l-c loaded transmission lines. *IEEE Trans. Microwave Theory Tech.*, 50:2702–2712, 2002.

[40] S. Ramo, J. R. Whinnery, and T. Van Duzer. *Fields and Waves in Communication Electronics*. John Wiley and Sons, third edition, 1994.

[41] G. V. Elefhteriades and K. G. Balmain. *Negative-Refraction Metamaterials*. John Wiley and Sons, 2005.

[42] C. Caloz and T. Itoh. *Electromagnetic Metamaterials*. John Wiley and Sons, 2006.

[43] P. P. M. So, H. Du, and W. J. R. Hoefer. Modeling of metamaterials with negative refractive index using 2-d shunt and 3-d scn tlm networks. *IEEE Trans. Microwave Theory Tech.*, 53:1496–1505, 2005.

[44] R. W. Ziolkowski and E. Heyman. Wave propagation in media having negative permittivity and permeability. *Phys. Rev. E.*, 64:056625, 2001.

[45] R. Landauer. in proceedings conference on electrical transport and optical properties of inhomogeneous media. In J.C. Garland and D.B. Tanner, editors, *America Institute of Physics*, page 2, New York (USA), 1978.

[46] D. Stroud. The effective medium approximations:some recent developments. *Superlattices Microstruct.*, 23(3/4):567–573, 1998.

[47] D. J. Bergman. The dielectric constant of a composite material - a problem in classical physics. *Physics Reports (Section C of Physics Letters)*, 43(9):377–407, 1978.

[48] J. C. M. Garnett. Colors in metal glasses and metal films. *Trans. Roy. Soc.*, 53:385–420, 1904.

[49] D. A. G. Bruggeman. Berechnung verschiedener physikalicher konstanten von heterogenen substanzen. i. dielektrizitatkonstanten und leitfahigkeiten der mischkorper aus isotropen substanzen. *Ann. Phys. (Leipzig)*, 24:636–664, 1935.

[50] O. Wiener. Zur theorie der refraktionskonstanten. *Berichteüber Verhanlungen Königlich-Sächsischen Gesellschaft Wisseschaften Leipzig*, pages 256–277, 1910.

[51] W. F. Brown Jr. Solid mixture permittivities. *J. Chem. Phys.*, 23(8):1514–1517, 1955.

[52] G. P. DeLoor. *Dielectric properties of heterogeneous mixtures*. PhD thesis, University of Leiden, Leiden, 1956.

[53] Z. Hashin and Shtrikman. A variational approach to the theory of the effective magnetic permeability of mutiphase materials. *J. Applied Physics*, 33(10):3125–3131, 1962.

[54] O. Pekonen, K. Kärkkäinen, A. H. Sihvola, and K. I. Nikoskinen. Numerical testing of dielectric mixing rules by fdtd method. *J. Electromagn. Waves Appl.*, 13:67–87, 1999.

[55] K. Kärkkäinen, A. H. Sihvola, and K. I. Nikoskinen. Effective permittivity of mixtures: numerical validation by the fdtd method. *IEEE Trans. Geosc. Remote Sensing*, 38(3):1303–1308, 2000.

[56] K. Kärkkäinen, A. H. Sihvola, and K. I. Nikoskinen. Analysis of a three-dimensional dielectric mixture with finite difference method. *IEEE Trans. Geosc. Remote Sensing*, 39(5):1313–1318, 2001.

[57] S. K. Park and K. W. Miller. Random number generators: good ones are hard to find. *Commun. ACM*, 31(10):1192, 1988.

[58] A. H. Sihvola. Self-consistency aspects of dielectric mixing theories. *IEEE Trans. Geosc. Remote Sensing*, 27(4):403–415, 1989.

[59] K. W. Whites and F. Wu. Effects of particle shape on the effective permittivity of composite materials with measurements for lattices or cubes. *IEEE Trans. Magnetics*, 50(7):1723–1729, 2002.

[60] O. Ouchetto, C. Qiu, S. Zouhdi, L. Li, and A. Razek. Homogenization of 3-d periodic bianisotropic metamaterials. *IEEE Trans. Microwave Theory Tech.*, 54(11):3893–3898, 2006.

[61] J. B. Pendry, D. Schurig, and D. R. Smith. Controlling electromagnetic fields. *Science*, 312(5781):1780–1782, 2006.

[62] A. J. Ward and J. B. Pendry. Refraction and geometry in maxwell's equations. *J. Mod. Opt.*, 43(4):773–793, 1996.

[63] Y. Luo, H. Chen, J. Zhang, L. Ran, and J. A. Kong. Design and analytical full-wave validation of the invisibility cloaks, concentrators, and field rotators created with a general class of transformation. *Phys. Rev. B*, 77:125127, 2008.

[64] W. Cai, U. K. Chettiar, A. V. Kildishev, and V. M. Shalaev. Nonmagnetic cloak with minimized scattering. *Appl. Phys. Lett.*, 91:111105, 2007.

[65] S. Xi, H. Chen, B-I. Wu, B. Zhang, J. Huangfu, D. Wang, and J. A. Kong. Effects of different transformations on the performance of cylindrical cloaks. *J. Electrom. Waves and Appl.*, 22:1489–1497, 2008.

[66] A. Nicolet, F. Zolla, Y Ould Agha, and S. Guenneau. Geometrical transformations and equivalent materials in computational electromagnetism. *Compel*, 27:806–819, 2008.

[67] H. Wang, H. Chen, L. Ran, J. Huangfu, J. A. Kong, and B-I Wu. Reconfigurable cloak for multiple operating frequencies. *App. Phys. Lett.*, 93:043515, 2008.

[68] D. Schurig, J. J. Mock, B. J. Justice, S. A. Cummer, J. B. Pendry, A. F. Starr, and D. R. Smith. Metamaterial electromagnetic cloak at microwave frequencies. *Science*, 314(5801):977–980, 2006.

[69] J. B. Pendry, A. J. Holden, D. J. Robbins, and Stewart W. J. Magnetism from conductors and enhanced nonlinear phenomena. *IEEE Trans. Microwave Theory Tech.*, 47:2075–2084, 1999.

[70] S. A. Cummer, B. I. Popa, D. Schurig, D. R. Smith, and J. Pendry. Full-wave simulations of electromagnetic cloaking structures. *Phys. Rev. E*, 74(3):036621, 2006.

[71] H. Chen, B-I Wu, B. Zhang, and J. A. Kong. Electromagnetic wave interactions with a metamaterial cloak. *Phys. Rev. Lett.*, 99:063903, 2007.

[72] Z. Ruan, M. Yan, C. W. Neff, and M. Qiu. Ideal cylindrical cloak: perfect but sensitive to tiny perturbations. *Phys. Rev. Lett.*, 99:113903, 2007.

[73] B. Zhang, H. Chen, B-I. Wu, Y. Luo, L. Ran, and J. A. Kong. Response of a cylindrical invisibility cloak to electromagnetic waves. *Phys. Rev. B*, 76:121101(R), 2007.

[74] H. Chen and C. T. Chan. Time delays and energy transport velocities in three dimensional ideal cloaking devices. *J. Appl. Phys.*, 104:033113, 2008.

[75] H. Chen, X. Luo, H. Ma, and C. T. Chan. The anti-cloak. *Opt. Express*, 16:14603, 2008.

[76] L. de Menezes and W. J. R. Hoefer. Modeling of general constitutive relationships using scn tlm. *IEEE Trans. Microwave Theory Tech.*, 44:854–861, 1996.

[77] J. P. Paul, C. Christopoulos, and D. W. P. Thomas. Generalized material models in tlm-part 2: Materials with anisotropic properties. *IEEE Trans. Antennas Propag.*, 47:1535–1542, 1999.

[78] Y. Huang, Y. Feng, and T. Jiang. Electromagnetic cloaking by layered structure of homogeneous isotropic materials. *Opt. Express*, 15(18):11133–11141, 2007.

[79] R. Luebbers, D. Ryan, and J. Beggs. A two-dimensional time-domain near-zone to far-zone transformation. *IEEE Trans. Antennas Propag.*, 40:848–851, 1992.

[80] C. A. Balanis. *Advanced Engineering Electromagnetics*. John Wiley and Sons, 1989.

[81] M. Yan, Z. Ruan, and M. Qiu. Cylindrical invisibility cloak with simplified material parameters is inherently visible. *Phys. Rev. Lett.*, 99:233901, 2007.

[82] Y. Zhao, C. Argyropoulos, and Y. Hao. Full-wave finite-difference time-domain simulation of electromagnetic cloaking structures. *Opt. Express*, 16:6717–6730, 2008.

[83] Z. Liang, P. Yao, X. Sun, and J. Xiang. The physical picture and the essential elements of the dynamical process for dispersive cloaking structures. *App. Phys. Lett.*, 92:131118, 2008.

[84] W. Cai, U. K. Chettiar, A. V. Kildishev, and V. M. Shalaev. Optical cloaking with metamaterials. *Nat.Photonics*, 1:224–227, 2007.

[85] B. Zhang, H. Chen, B-I. Wu, and J. A. Kong. Extraordinary surface voltage effect in the invisibility cloak with an active device inside. *Phys. Rev. Lett.*, 100:063904, 2008.

[86] F. Zolla, S. Guenneau, A. Nicolet, and J. B. Pendry. Electromagnetic analysis of cylindrical invisibility cloaks and the mirage effect. *Opt. Lett.*, 32:1069–1071, 2007.

[87] P. Yao, Z. Liang, and X. Jiang. Limitation of the electromagnetic cloak with dispersive material. *App. Phys. Lett.*, 92:031111, 2008.

[88] B. Zhang, B-I Wu, H. Chen, and J. A. Kong. Rainbow and blueshift effect of a dispersive spherical invisibility cloak impinged on by a nonmonochromatic plane wave. *Phys. Rev. Lett.*, 101:063902, 2008.

[89] J. B. Pendry, A. J. Holden, W. J. Stewart, and I. Youngs. Extremely low frequency plasmons in metallic mesostructures. *Phys. Rev. Lett.*, 76:4773–4776, 1996.

[90] L. D. Landau, E. M. Lifshitz, and L. P. Pitaevskii. *Electrodynamics of continuous media*. Pergamon Press Ltd., second edition, 1984.

[91] A. D. Yaghjian and S. Maci. Alternative derivation of electromagnetic cloaks and concentrators. *New. J. Phys.*, 10:115022, 2008.

[92] E. N. Economou, Th. Koschny, and C. M. Soukoulis. Strong diamagnetic response in split-ring-resonator metamaterials: Numerical study and two-loop model. *Phys. Rev. B*, 77:092401, 2008.

[93] G. Castaldi, I. Gallina, V. Galdi, A. Alùç, and N. Engheta. Cloak/anti-cloak interactions. *Opt. Express*, 17(5):3101–3114, 2009.